Control of chemical dynamics of polyatomic molecules by IR and UV laser pulses

A Thesis
submitted for the degree of

Doctor of Philosophy

by

Nitai Giri
Reg. No. 17CHPH04
giri.nitai@gmail.com

School of Chemistry
University of Hyderabad
Hyderabad - 500 046, INDIA
August 2023

Dedicated
to
my family

Declaration of Authorship

I hereby declare that the matter embodied in the thesis entitled **"Control of chemical dynamics of polyatomic molecules by IR and UV laser pulses"** is the result of investigations carried out by me in the School of Chemistry, University of Hyderabad, India under the supervision of Prof. Susanta Mahapatra.

In keeping with the general practice of reporting scientific investigations, acknowledgements have been made wherever the work described is based on the finding of other investigators.

16/08/23
Date

Nitai Giri
Signature of the candidate

Certificate

School of Chemistry
University of Hyderabad
Hyderabad-500 046
India

This is to certify that the work contained in this thesis, titled "**Control of chemical dynamics in polyatomic molecules by IR and UV laser pulses**" by **Nitai Giri (Reg. No. 17CHPH04)**, has been carried out under my supervision and is not submitted elsewhere for a degree.

This thesis is free from plagiarism and has not been submitted previously in part or in full to this or any other University or Institution for award of any degree or diploma.

Parts of this thesis have been published in the following publications:

1. **N. Giri** and S. Mahapatra*, J. Chem. Phys. **156**, 094305 (2022), **Chap. 5**.

and presented in following conferences :

1. 18^{th} Annual In-House Symposium (CHEMFEST 2020) (poster presentation)
2. 20^{th} Annual In-House Symposium (CHEMFEST 2022) (oral presentation)
3. 20^{th} Annual In-House Symposium (CHEMFEST 2022) (poster presentation)

Further, the student has passed the following courses towards fulfilment of coursework requirement for Ph.D.

Course code	Name	Credits	Pass/Fail
1. CY801	Research Proposal	3	Pass
2. CY805	Instrumental Methods-A	4	Pass
3. CY354	Computer Programming and Numerical Methods	3	Pass
4. CY577	Computational Chemistry	2	Pass

16/08/23

Date

S Mahapatra

Supervisor: Prof. Susanta Mahapatra

Susanta Mahapatra
Professor
School of Chemistry
University of Hyderabad
Hyderabad-500 046, India.

Dean
School of Chemistry
University of Hyderabad

Dean
SCHOOL OF CHEMISTRY
University of Hyderabad
Hyderabad-500 046.

Acknowledgements

I would like to express my sincere gratitude to my PhD supervisor Prof. Susanta Mahapatra for his constant guidance and encouragement throughout my research work. I am very much thankful to him for the valuable discussions, especially in the group meetings.

I would like to thank Prof. Zhengang Lan, Qingdao Institute of Bioenergy and Bioprocess Technology for the discussions related to the photodissociation involving coupled electronic states. I thank Prof. Harjinder Singh, IIIT Hyderabad for the fruitful discussion.

I would like to thank the present and former Deans, School of Chemistry, UoH for their support and help during my research work. I thank to my DC members Dr. Debashis Barik and Dr. K. V. Jovan Jose for their support and help.

I express heartful thanks to my labmates Alamgir, Ajay Rawat, Yarram Ajay, Daradi, Mamilwar Rani, Jhansi Rani, Dr. Arun, Dr. Jayakrushna, Dr. Sugata, Dr. Arpita, Dr. Rudra, Dr. Karunamoy, Dr. Satyadendra Gupta, Dr. B. Manjusha and Dr. Mohammed Shavez for a friendly environment and many fruitful discussions.

I would like thank the University Grant Commission (UGC), New Delhi, India for the financial support.

I would like to thank my friends, Sumanta, Suman, Shubham, Anupam and Nilanjan for their support and friendship.

Finally and most importantly, I would like to thank to my family Moumita, my little one (Srihith), my parent and my elder brother for their love, care and endless support in all times of my life.

Nitai Giri

List of Abbreviations

BS	Brumer-Shapiro
BO	Born-Oppenheimer
CDA	Constant Dipole Approximation
CI	Conical Intersection
CG	Conjugate Gradient
DFT	Discrete Fourier Transform
DVR	Discrete Variable Representation
FC	Franck-Condon
FFT	Fast Fourier Transform
FGH	Fourier Grid Hamiltonian
GA	Genetic Algorithm
GP	Geometric Phase
HT	Hydrogen Transfer
IVR	Intramolecular Vibrational Redistribution/Relaxation
KE	Kinetic Energy
OCT	Optimal Control Theory
PES	Potential Energy Surface
PE	Potential Energy
RHS	Right Hand Side
SO	Split Operator
STIRAP	Stimulated Raman Adiabatic Passage
TDM	Transition Dipole Moment
TDSE	Time-Dependent Schrödinger Equation
TISE	Time-Independent Schrödinger Equation
TDWP	Time-Dependent Wavepacket Propagation
TMF	Transition Moment Function
TRK	Tannor, Rice and Kosloff
VC	Vibronic Coupling
WP	Wave packet

Contents

List of Figures

List of Tables

Chapter 1

Introduction

Chemical reactions at the atomic level involve in the rupture and construction of bonds between specific atoms of a molecule. This rupture and construction of bonds take place in the femtosecond (10^{-15} sec) timescale. Chemical reactions often result multiple products. In such situations, controlling a specific product over another is a long-held scientific dream. In traditional control schemes, experimental chemists vary the macroscopic parameters e.g., pressure, temperature, concentration of reactants, pH, or lowering a reaction barrier by using a catalyst. These types of schemes refer to the macroscopic control. Intermolecular collisional behaviour is modified in those methodologies. When one gives excess energy to a chemical reaction, generally, the energy is not localized in a specific bond rather it is distributed statistically over various degrees of freedom. Therefore, a chemical reaction results both unwanted products and the desired products. However, neither of the traditional methods offers a satisfying solution to a chemical reaction. Therefore, one seeks for novel strategies to perform selective, clean and energy-efficient chemistry. In this context, laser light with optimal control theory is considered to be an efficient tool to control a specific product of a chemical reaction.

1.1 Laser light as a controlling reagent

The laser light was invented in 1960. Chemists have dreamed to take advantage of the special properties of the laser light e.g., enormous intensity, monochromaticity, phase coherence, etc., to carry out clean, energetically efficient and selective photochemistry [1, 2]. The laser light is viewed as an ideal chemical reagent in that all of its parameters can be actively and completely controlled. The laser radiation deposits energy on the molecule in a non-statistical fashion. In the early days, various approaches had been developed based on the properties like high monochromaticity and tunability of narrowly structured lasers to perform the bond selective chemistry [3–7]. In general, the laser field-induced bond selective chemistry is not feasible because of the rapid intramolecular vibrational redistribution (IVR) [8–13] excluding a few studies [14–17] where the deposited energy flows along a specific bond by avoiding the IVR in the molecules. At a high level of excitation, the energy is redistributed among the strongly coupled vibrational modes. The molecular phenomena, IVR takes place in a short timescale among various coupled degrees of freedom of isolated and excited molecules. In these experiments, the laser pulses were tuned according to the characteristic of a specific bond without accounting for the complex dynamical behaviour of the rest of the systems.

In the context of controlling an outcome of laser-induced chemical reactions, an alternative idea is developed based on the quantum interference of various reaction paths on potential energy surfaces (PESs) connecting a reactant to a product. The laser field interacts with a system and prepares various intermediate states for different reaction paths. The frequency profile of a laser pulse is imprinted with the energy associated with these intermediate states. This can be understood in the representation [see Fig. (1.1)] of the coherent wave packet (WP). A diatomic molecule is excited with the help of an ultrashort

laser pulse to an excited electronic state. If the time duration of a laser pulse is briefer than the vibrational period (typically femtosecond to picosecond) then the bandwidth of the pulse incorporates multiple vibrational eigenfunctions. Those eigenfunctions are superposed coherently by altering amplitudes and phases to generate a localized WP. The laser pulse prepared localized WPs or the intermediate states are connected to the reactant and product through multiple pathways. These states (or dynamical paths associated with them) interfere constructively or destructively to enhance or suppress the desired product amplitude. In this way, one can control the outcome of a reaction by manipulating reaction pathways. The manipulation of the quantum interference between multiple pathways is performed actively by varying parameters of a laser pulse. Therefore, properties of PESs and their eigenstates are employed in this approach.

Advances in the laser technology [18–24] as well as various developments and improvements in spectroscopic techniques [25–28] helped us to get valuable information about electronic, vibrational and rotational motions [29–34] in many molecules, ranging from simple diatomic molecules to polyatomic complex molecules. In the recent past, theoretical concepts of controlling quantum dynamics using shaped laser pulses have been experimentally implemented with encouraging results [35–40].

1.2 Theoretical methods

Quantum control methods have been developed to control an outcome of a chemical reaction differ from the traditional macroscopic control methods discussed in the previous section. In the former methods, the WP evolution of a molecule is controlled in a laser light-induced process. The central idea of these methodologies is based on the quantum interference in laser light-induced

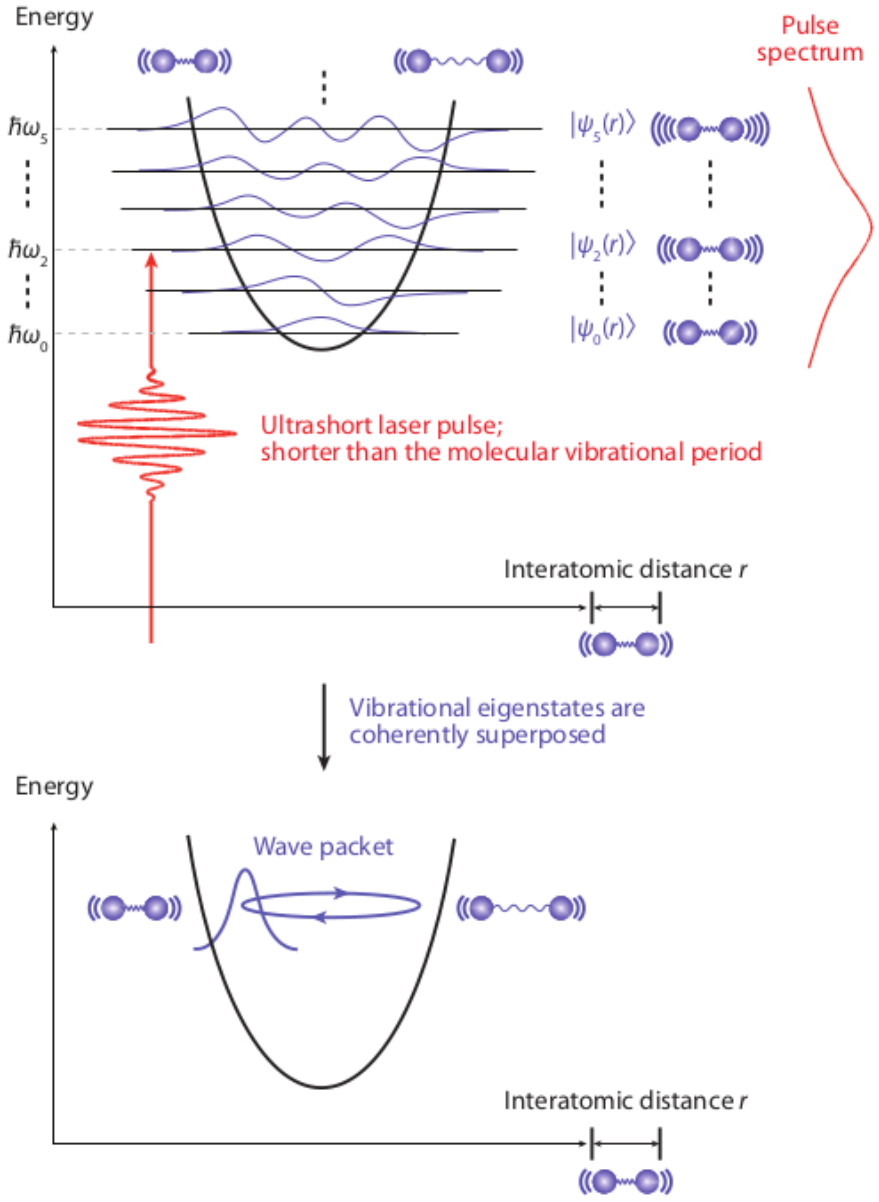

Figure 1.1: The above figure represents the construction of a coherent vibrational WP of an excited electronic state with an ultrashort laser pulse for a diatomic molecule [K. Ohmori, Ann. Rev. Phys. Chem. 60, 487 (2009)].

events. In those quantum control methods, the coherence property of laser is exploited to manipulate the molecular dynamics. The goal is to generate a specific product efficiently while reducing unwanted side products. The idea of controlling an outcome of quantum mechanical systems towards a specific direction by the application of a suitable laser field is in general referred to as "coherent control" or "quantum control". Various theoretical schemes are developed over the years in the context of quantum control.

1.3 Single-parameter control strategies

1.3.1 Pump-dump control

In the 1980s, the pump-dump control strategy was developed [41, 42] by Tannor, Rice and Kosloff to control the chemical reactivity using the coherent properties of the laser light. This approach is based on the time gap between pump and dump laser pulses of femtosecond timescale. It is referred to as the TRK model. The pump pulse excites the WP from the ground electronic state to an excited state where the WP evolves freely and finally, the WP is de-excited by the dump pulse [see Fig. (1.2)]. The coherent properties of the laser pulses are exploited in the proposed methodology. The excitation and evolution processes are treated separately. The WP moves various product regions on the PES. Different time delays between these pulses result different time durations of the WP evolution on the excited state leading to different products. The selectivity of reaction products is controlled by varying the "time delay (ΔT)" between the pump and dump pulses. A large fraction of the product population can be accomplished in a reaction where the WP on the excited state evolves in a localized (coherent) fashion and greatly it is dumped back to a product channel. Here, the excited state helps to control the chemistry on the ground electronic state. The pump-dump control scheme is demonstrated successfully to control photofragmentation reactions in small molecules [43–48]. This scheme is used

as a spectroscopic tool in various studies [49–53] to guide real-time dynamics. However, the TRK scheme has a limitation because of the consideration of the transform-limited laser pulses having frequency-independent phases.

1.3.2 Phase control

Another novel scheme was suggested by Brumer and Shapiro (BS) [54–57] based on the quantum interference of two independent laser pulse-driven excitations connecting to the same initial and final states [58–60]. The initial state absorbs n photons of the first colour of frequency, ω_n and m photons of the second colour of frequency, ω_m such that $n\omega_n = m\omega_m$ [see Fig. (1.2)]. The coherent laser pulses interact with the initial state and create a superposition of eigenstates connecting to different reaction products. The resultant product probability is optimized by varying the "relative phase ($\Delta\Phi$)" between two coherent radiations. The BS control scheme has been applied experimentally in various scenarios, for example, the selective population transfer in small molecules, atoms [61–64], and photochemical reactions [65–68]. However, the BS method is limited practically as the difficulties that arise from the simultaneous excitations for both the reaction paths with the locking of phases and amplitudes of the laser radiation in optically dense media [69].

1.3.3 STRIP control

Besides these two novel approaches, there is another approach proposed by Bergmann and co-workers, known as the stimulated Raman adiabatic passage (STRIP) control [70–73]. In this scheme, two laser pulses couple with three states rather than one couple with two quantum states. Two pulses are used in a counter-intuitive way to transfer the population to a target state. The pump pulse connects an initial state with an intermediate state [see Fig. (1.2)]. On the other hand, the stokes pulse links the intermediate state with the desired target

state. By tuning the time delay between these pulses, the intermediate state population is kept at zero to avoid radiative decay. This strategy exploits the properties of the quantum interference between two transitions induced by the pulses. In general, the pump pulse overlaps partially with the Stokes pulse in a complete population transfer process. The STRIP control has been successfully demonstrated for small molecular systems [73–75]. For large polyatomic systems, the STRIP control is quite difficult to achieve as these systems have a high density of states [73, 76].

The discussed control strategies are based on the idea of controlling a single laser pulse parameter and they can be successful for small molecular systems. Nevertheless, for polyatomic molecules because of the complex nature of PESs, these schemes may not be efficient. Therefore, it is an apparent need for a laser pulse general shaping scheme that is robust and flexible and that can result precisely tailored laser fields to manipulate the nuclear dynamics. Here, we discuss one such approach, namely optimal control theory.

1.4 Multiple laser parameters control: optimal control theory (OCT) and its experimental realization

1.4.1 Optimal control theory

In the subject of the coherent control of a reaction product using a laser pulse, Tannor and Rice suggested a variational approach in which the optimum waveform of laser pulses (shaped) is obtained using calculus of variation [77]. This variational approach is further extended by Rabitz et al. [78–81] and others [82, 83] to design an optimally shaped laser pulse in the mathematical framework of optimal control theory. They proposed that it would be possible to guide a quantum mechanical system toward a specific objective by tailoring a laser pulse.

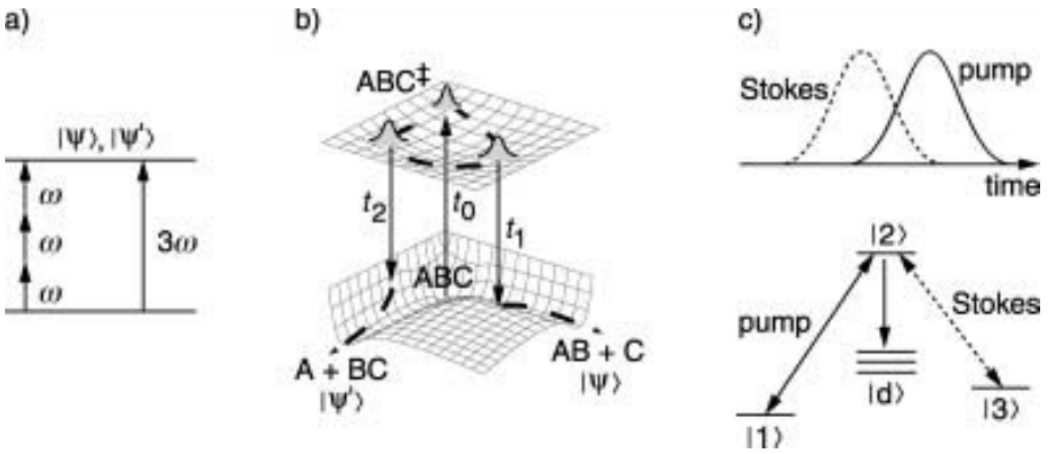

Figure 1.2: The above figure represents: (a) BS phase control scheme, (b) TRK pump-dump scheme, (c) STRIP control scheme by Bergmann *et el.*. These are the single-parameter quantum control schemes [T. Brixner and G. Gerber, Chem. Phys. Chem. 4, 418 (2003)].

This approach includes multiple laser pulse parameters to control over dynamics of a molecular system. In this approach, a cost functional is constructed by considering a control problem. An optimally shaped laser pulse is designed by maximizing the cost functional. The shaped laser pulse maximizes the formation of a desired product. This control scheme is applied to steer the outcome of various molecular processes e.g., state selective population transfer [84–90], molecular orientation [91, 92], isomerization reactions [93–97], electron current in aromatic rings [98, 99], separation of isotopes [100], design of quantum logic gates [101–106], etc.

1.4.2 Experimental implementations

Optimal laser pulses constructed theoretically by OCT are faced a number of difficulties while testing in a laboratory. A major problem arises because of the use of an approximate Hamiltonian for a polyatomic system in OCT calculations. Polyatomic systems have the complicated nature of molecular Hamiltonians in

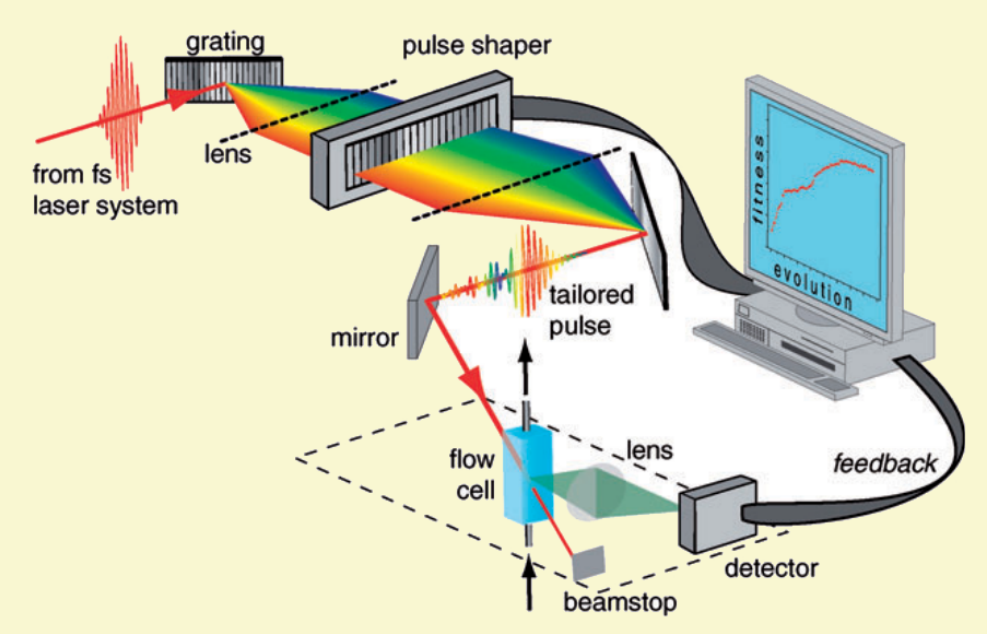

Figure 1.3: The above figure represents the adaptive feedback control (AFC) technique [G. Gerber et al., Phys. Chem. Chem. Phys., 9, 2470 (2007)].

which many degrees of freedom are tightly coupled. Therefore, the approximate Hamiltonian could not lead to the best optimal laser pulse for the experimental implementation. Another type of problem can arise from laboratory uncertainties due to optical laser pulse generation errors (uncertainties in phase and amplitude, and a certain amount of noise). The theoretically calculated laser field using an approximate molecular Hamiltonian may not be robust enough to tolerate errors from the real Hamiltonian for the system as well as from the laboratory uncertainties. To circumvent these difficulties, Rabitz and co-workers [107] have proposed a closed-loop learning technique using the adaptive feedback control strategy. The experimental setup consists of a laser light source, a measurement device and an analog computer that solves the Schrödinger equation in real-time and a sample of molecules of interest [see Fig. (1.3)]. The computer runs a genetic algorithm as a learning algorithm to direct the production of a laser pulse sequence based on "fitness" information received by the laboratory measurement

device. The measurement device is coupled to a learning algorithm (e.g., genetic algorithm) which is capable of recognizing patterns for a laser pulse sequence for a new experiment in the input-output mechanism. Over several generations, the algorithm learns an optimal laser pulse sequence. Overall this scheme is referred to as the adaptive feedback control (AFC).

Such procedures are much needed in the context of designing optimal laser pulses, especially for polyatomic molecules. Significant advancements in the subject of quantum control by designing optimal laser pulses are achieved by introducing adaptive feedback control methods in the laboratory. The advantage of AFC methods for designing an optimal pulse is that it does not need any prior knowledge about PESs, molecular Hamiltonian and reaction mechanisms. The AFC method was first demonstrated experimentally by Bardeen *et al.* [108] by controlling the fluorescence of a large organic dye in the solution. Gerber *et al.* [109] studied photodissociation reactions of $CpFe(CO)_2Cl$ by using this method. Various groups demonstrated the AFC technique as an efficient experimental method to control various physical, chemical and biological processes [110–127].

1.4.3 Importance of theoretical design of laser pulses

Laser pulses are designed theoretically employing optimal control theory have an important role in the experimental realization of the manipulation of quantum dynamics. These theoretical studies help us to understand the molecular dynamics as well as to realize the control mechanism. On the other hand, for the experimental implementation of the quantum control, one needs an expensive experimental setup including a computer-controlled laser pulse shaper and a device for the measurement of an outcome of a given system. Therefore, before performing the control experiment in a laboratory, theoretical control simulations can be performed to check the feasibility of the quantum control. Theoretically,

designed laser pulses can be used as an excellent initial guess for experiments.

1.5 Outline of the thesis

Optimal laser pulses are theoretically designed for various vibrational transitions, tautomerization and photodissociation in the polyatomic systems. The optimal laser pulses are tailored in the mathematical framework of optimal control theory. The nuclear dynamics of these processes are studied within the adiabatic and diabatic representations. The interaction between the laser light with a system is considered within the semiclassical dipole approximation. The nuclear motion of these systems follows the time-dependent Schrödinger equation (TDSE). The split-operator (SO) and fast Fourier transformation (FFT) methods are employed to solve the nuclear dynamics of the laser field-driven molecular processes. The theoretical methods are discussed in **Chap.** 2.

Various vibrational transitions of the ground electronic state of the 4(3H)-pyrimidinone/4-hydroxypyrimidine system are controlled in the presence of optimal laser pulses. The PES for the ground electronic state along the OH bond distance has been calculated employing the Coupled Cluster Singles and Doubles (CCSD) method using an aug-cc-pVDZ basis set and the dipole moment is calculated from the complete-active-space self-consistent-field (CASSCF) method employing the Molpro package. The ground electronic state has a potential barrier of 180 kJ/mol and the latter separates the tautomers. The optimal laser pulses are designed employing the conjugate gradient method. The initial state population is transferred efficiently to the target vibrational state in the presence of the optimal pulse. These optimal pulses are constructed in different time durations i.e., 30000, 60000 and 90000 a.u. for different values of penalty factor, α_0 i.e., 0.1 and 0.01. It is observed that the field amplitudes of the optimal laser pulses decrease with higher time durations with the agreement

of the pulse area theorem [128, 129]. In frequency spectra, besides the sharp peak which is responsible for the considered transition, there are secondary peaks that appear because of the involvement of intermediate vibrational states. At the end of the time durations, almost 100% population reaches the target vibrational state. This work is included in **Chap.** 3.

The excited state-mediated tautomerization is controlled through the pump-dump mechanism [41, 42] of the tautomerization of 4(3H)-pyrimidinone. The intramolecular hydrogen transfer reaction occurs in the tautomerization. The model composes two electronic states i.e., the ground electronic state and $\pi\pi^*$ state. The PESs for the ground electronic state and $\pi\pi^*$ state are calculated using the equation-of-motion coupled cluster singles and doubles (EOM-CCSD) method using an aug-cc-pVDZ basis set employing the Molpro package. The optimal calculations are performed considering the *ab initio* calculated transition dipole moment (TDM) and constant TDM (Condon approximation) conditions. A pair of ultrashort laser pulses are designed using the genetic algorithm. The pump laser pulse excites the initial state to the $\pi\pi^*$ state from the ground electronic state. The excited WP freely evolves on the $\pi\pi^*$ state. When the WP reaches the product region on the $\pi\pi^*$ state, at that time the dump pulse is activated. The dump pulse de-excites the WP back to the ground electronic state. This work is presented in detail in **Chap.** 4.

The photodissociation of the OH bond of phenol is controlled in the presence of the UV laser pulse. The optimal laser pulse is designed in optimal control theory employing the genetic algorithm. The photodissociation dynamics is performed on the three lowest electronic states i.e., the ground electronic state, the $\pi\pi^*$ state and the $\pi\sigma^*$ state including two nuclear degrees of freedom i.e., the OH stretching coordinate and CCOH dihedral angle. Vibrational wave

functions (defined by, $|n_r, n_\theta\rangle$, where n_r and n_θ denote the number of nodes along the reaction coordinate and coupling coordinate, respectively) of the ground electronic state are determined using the pseudo-spectral method. An initial state is prepared from a vibrational wave function (mentioned earlier) on the ground electronic state. The total outgoing dissociative flux is maximized in the optimization process, calculated in the S_0 and S_1 adiabatic asymptotic channels. The photodissociation process occurs through different mechanisms for different initial states. The optimal UV pulse excites the system predominantly to the $\pi\sigma^*$ state over the $\pi\pi^*$ state for the $|0,0\rangle$ and $|0,1\rangle$ initial states. On the other hand, for the $|1,0\rangle$ and $|1,1\rangle$ initial states, the system is excited to both the $\pi\pi^*$ and $\pi\sigma^*$ states. The diabatic coupling element between the $\pi\pi^*$ and $\pi\sigma^*$ states play an important role to determine the symmetry of the wave function on the $\pi\sigma^*$ state. However, In the presence of the optimal UV laser pulse, the WP does not get sufficient energy to reach the S_2 asymptote and the dissociation entirely ($\sim$100%) takes place in S_0 and S_1 asymptotic channels. This study is discussed in detail in **Chap.** 5.

The photodissociation of the OH bond of phenol (discussed in **Chap.** 5) has been extended with the optimal IR laser pulse. The vibrational eigenfunctions viz., $|0,0\rangle$, $|0,1\rangle$ and $|0,2\rangle$ are considered initial states for the optimal calculations. These eigenfunctions have lower energy as compared to the potential barrier present along the OH stretching coordinate on the $\pi\pi^*$ state. These vibrational eigenfunctions hardly dissociate in the field-free condition [130] because of the potential barrier. The optimal laser pulse for the photodissociation is designed in the genetic algorithm. The multiphoton pump-dump events are repeatedly operational in the field-induced condition. Consequently, the WP population becomes vibrationally hot on the ground electronic state as well as on the $\pi\pi^*$ state. As the WP becomes vibrationally excited it crosses the potential barrier

and the $\pi\sigma^*$ mediated photodissociation is observed. This work is included in **Chap.** 6.

Finally, a summary of this thesis and its future direction is presented in **Chap.** 7.

Chapter 2

Theory

In this thesis, IR or UV laser pulses are constructed to manipulate the quantum dynamics of molecules. These laser pulses are tailored in the mathematical framework of optimal control theory. Two optimization methods viz., the conjugate gradient method and genetic algorithm are employed to optimize a desired outcome. The laser-molecule interaction is considered within the semiclassical dipole approximation and systems follow the time-dependent Schrödinger equation (TDSE). The quantum dynamical equation of motion is solved numerically using the split-operator method (SO) and fast Fourier transformation (FFT) method. The derivation of the working equations, optimization schemes and numerical methods are discussed in this chapter.

2.1 Light-matter interaction

We consider a system of classical charged particles interacting with the electromagnetic radiation of laser light. The dynamics of the E(r,t) and B(r,t) of

the electromagnetic field are described by Maxwell's equations [131],

$$\nabla \cdot \mathbf{E}(\mathbf{r},t) = \frac{1}{\epsilon_0}\rho(\mathbf{r},t), \tag{2.1}$$

$$\nabla \cdot \mathbf{B}(\mathbf{r},t) = 0, \tag{2.2}$$

$$\nabla \times \mathbf{E}(\mathbf{r},t) = -\frac{1}{c}\frac{\partial}{\partial t}\mathbf{B}(\mathbf{r},t), \tag{2.3}$$

$$\nabla \times \mathbf{B}(\mathbf{r},t) = \frac{1}{c}\frac{\partial}{\partial t}\mathbf{E}(\mathbf{r},t) + \frac{1}{\epsilon_0 c}\mathbf{j}(\mathbf{r},t), \tag{2.4}$$

where c is the speed of light and ϵ_0 denotes the permittivity of vacuum. The motion of the charged particles in the electromagnetic field is determined by the Lorentz's equation,

$$m_i\frac{d\mathbf{v}_i}{dt} = \mathbf{F}(\mathbf{r}_i,t) = q_i\left[\mathbf{E}(\mathbf{r}_i,t) + \frac{\mathbf{v}_i}{c} \times \mathbf{B}(\mathbf{r}_i,t)\right], \tag{2.5}$$

where r_i, m_i, v_i and q_i are the position, the mass, the velocity and the charge of the i^{th} particle. $\rho(r,t)$ and $j(r,t)$ denote the charged-particle density and the current of the charged particles, respectively. These are defined as

$$\rho(\mathbf{r},t) = \sum_i q_i\delta[\mathbf{r} - \mathbf{r}_i(t)], \tag{2.6}$$

$$\mathbf{j}(\mathbf{r},t) = \sum_i q_i\mathbf{v}_i\delta[\mathbf{r} - \mathbf{r}_i(t)]. \tag{2.7}$$

It is important to re-express the fields using the vector potential, $A(r,t)$ and scalar potential, $\phi(r,t)$ by the succeeding equations,

$$\mathbf{B} = \nabla \times \mathbf{A}, \tag{2.8}$$

$$\mathbf{E} = -\frac{1}{c}\frac{\partial \mathbf{A}}{\partial t} - \nabla\Phi. \tag{2.9}$$

It can be noted that various forms of the vector and scalar potentials can be defined and they are so-called gauges that result the same electromagnetic fields. Other potentials, $\phi'(r,t)$ and $A'(r,t)$ can be constructed (from Eqs. (2.8) and (2.9)) using $\phi(r,t)$ and $A(r,t)$,

$$\mathbf{A}' = \mathbf{A} + \nabla\chi, \tag{2.10}$$

$$\Phi' = \Phi - \frac{1}{c}\frac{\partial\chi}{\partial t}, \tag{2.11}$$

where χ is an arbitrary scalar field that is often chosen to be the so-called Coulomb gauge. Therefore, the chosen field satisfies the equation, $\nabla^2\chi = -\nabla \cdot A$. Hence Eq. (2.10) reduced to the following equation,

$$\nabla \cdot \mathbf{A}' = 0. \tag{2.12}$$

Note that the different choices of χ' satisfy the relation, $\nabla^2\chi' = 0$ and also satisfy Eq. (2.12). This flexibility is used in this section later.

The classical Hamiltonian of the particles plus the electromagnetic fields, H is expressed as

$$\begin{aligned} H &= \sum_i \frac{1}{2} m_i (\frac{\partial \mathbf{r}_i}{\partial t})^2 + \sum_i q_i \Phi_i(\mathbf{r}_i) + \frac{\epsilon_0}{2} \int [\mathbf{E}^2(\mathbf{r}_i, t) + \mathbf{B}^2(\mathbf{r}_i, t)]^2 d^3\mathbf{r}, & (2.13) \\ &\equiv \sum_i \frac{1}{2} m_i (\frac{\partial \mathbf{r}_i}{\partial t})^2 + V_C + H_R, & (2.14) \end{aligned}$$

where

$$\Phi_i(r) = \frac{1}{4\pi\epsilon_0} \sum_{j<i} \frac{q_j}{|\mathbf{r} - \mathbf{r}_j|}, \tag{2.15}$$

and V_C and H_R are the electrostatic potential energy (PE) of the particles and the total energy of the electromagnetic field, respectively. In the above equation, the first term on the right hand side is the sum of the kinetic energy of the particles.

Here, we are going to quantize the dynamics of the particles. Basically, it is the conversion from the classical mechanics of the particles to the quantum mechanics. First, we express the canonical momentum [132] (incorporating the Lorentz's velocity-dependent forces) of the ith particle in the electromagnetic fields,

$$p_i = m_i \frac{d\mathbf{r}_i}{dt} + \frac{q_i}{c} \mathbf{A}(\mathbf{r}_i, t). \tag{2.16}$$

Including the above equation, the Hamiltonian of the particles plus the fields is re-expressed as

$$H = \sum_i \frac{1}{2m_i}[\mathbf{p}_i - \frac{q_i}{c}\mathbf{A}(\mathbf{r}_i, t)]^2 + V_C + H_R. \tag{2.17}$$

We can replace the canonical momentum with the quantum mechanical momentum operator that is given as

$$\mathbf{p}_j = -i\hbar\nabla_j. \tag{2.18}$$

The Hamiltonian re-defined using the above equation in the coordinate representation as follows

$$\begin{aligned} H &= \sum_i \frac{1}{2m_i}[(-i\hbar\nabla_i) - \frac{q_i}{c}\mathbf{A}(\mathbf{r}_i, t)]^2 + V_C + H_R, & (2.19)\\ &= H_M + H_{int}(t) + H_R, & (2.20) \end{aligned}$$

where the material Hamiltonian, H_M and the interaction Hamiltonian, $H_{int}(t)$ have the form,

$$H_M = \sum_i \frac{-\hbar^2\nabla_i^2}{2m_i} + V_C, \tag{2.21}$$

and

$$H_{int}(t) = \sum_i \frac{iq_i\hbar}{m_i c}\nabla_i \cdot \mathbf{A}(\mathbf{r}_i, t) + \frac{q_i^2}{2m_i c^2}\mathbf{A}^2(\mathbf{r}_i, t), \tag{2.22}$$

respectively. The dynamics of the particles in the electromagnetic fields are described by the TDSE,

$$i\hbar\frac{\partial\Psi(\mathbf{r}, t)}{\partial t} = \left\{ \sum_i \frac{1}{2m_i}[(-i\hbar\nabla_i) - \frac{q_i}{c}\mathbf{A}(\mathbf{r}_i, t)]^2 + V_C \right\}\Psi(\mathbf{r}, t). \tag{2.23}$$

The wavelength of visible light appears in the range of 4000-7000 Å whereas the displacement of the particles in a molecule varies from 1-10 Å. Therefore, all the displacements ($\mathbf{r}_j$) in A are replaced with the position of the center-of-mass of the molecule. For a plane wave, A(r,t) is re-defined considering the z projection

of the location of the center of molecular mass. Therefore, A(r,t) is approximated as

$$\mathbf{A}(\mathbf{r}_i, t) \approx \mathbf{A}(z_i, t). \tag{2.24}$$

This is called *dipole approximation*.

With this approximation, we choose χ as

$$\chi = -\sum_i \mathbf{r}_i \cdot \mathbf{A}(z, t). \tag{2.25}$$

Because of the *dipole approximation*, there is no r dependency of $\mathbf{A}$(z,t). It results $\nabla^2\chi = 0$.

The TDSE of the particles can be expressed using the definition of V_c [Eq. (2.15)] and χ [Eq. (2.25)] (noting that $\nabla\chi = -\mathbf{A}$) as

$$i\hbar\frac{\partial\Psi(\mathbf{r}, t)}{\partial t} = \sum_i \left[\frac{-\hbar^2}{2m_i}\nabla_i^2 + q_i\Phi_i(\mathbf{r}_i) + \frac{q_i}{c}\mathbf{r}_i \cdot \frac{\partial\mathbf{A}(z, t)}{\partial t}\right]\Psi(\mathbf{r}, t). \tag{2.26}$$

In the above equation, the last term of the square bracket is converted to $-q_i r_i \cdot E(z, t)$ [cf., 2.9] and we get the TDSE of the particles as

$$i\hbar\frac{\partial\Psi(\mathbf{r}, t)}{\partial t} = \sum_i \left[\frac{-\hbar^2}{2m_i}\nabla_i^2 + q_i\Phi_i(\mathbf{r}_i) - q_i\mathbf{r}_i \cdot \mathbf{E}(z, t)\right]\Psi(\mathbf{r}, t). \tag{2.27}$$

In the above equation, the last term is the matter-radiation interaction Hamiltonian, H_{MR} and the first two terms denote the material Hamiltonian in the field-free condition, H_{MR}. Therefore, the TDSE of the particles reads as

$$i\hbar\frac{\partial\Psi(t)}{\partial t} = [H_M + H_{MR}(t)]\Psi(t). \tag{2.28}$$

The matter-radiation interaction term of Eq. (2.27) i.e., H_{MR} is rewritten as

$$H_{MR} = -\boldsymbol{\mu} \cdot \mathbf{E}(z,t). \tag{2.29}$$

In the above equation, $\boldsymbol{\mu}$ is the dipole moment and it is given as

$$\boldsymbol{\mu} = \sum_i q_i \mathbf{r}_i. \tag{2.30}$$

It is relevant to go beyond the dipole approximation when the electric field as a function of $\mathbf{r}_i$ can not be avoided [133]. In such situations, one can consider the interactions between the higher multipoles with the field. However, here, the dipole approximation appears to be sufficient and the interaction is treated with Eqs. (2.28) and (2.29).

2.2 Theory of the nuclear motion in an electronic surface(s)

In this thesis, we present the nuclear motion in a single electronic state as well as in multiple coupled electronic states. Here, we start the discussion with a central and basic concept i.e., the Born-Oppenheimer approximation [134].

2.2.1 Born-Oppenheimer approximation

The total molecular Hamiltonian is expressed as

$$\hat{H} = \sum_i -\frac{\hbar^2 \nabla_{e,i}^2}{2m} + \sum_{j>i} \frac{e^2}{|r_{e,i} - r_{e,j}|} + \sum_i -\frac{\hbar^2 \nabla_{N,i}^2}{2M_i} + \sum_{j>i} \frac{Z_i Z_j e^2}{|R_{N,i} - R_{N,j}|} + \sum_{ij} \frac{Z_j e^2}{|r_{e,i} - R_{N,j}|}, \tag{2.31}$$

$$\equiv \hat{T}_e + \hat{V}_e + \hat{T}_N + \hat{V}_N + \hat{V}_{eN}, \tag{2.32}$$

where R_N and r denote nuclear and electronic coordinates, respectively. Similarly, ∇_N and ∇_e refer to nuclear and electronic momenta, respectively. Z_i represents the nuclear charge on the i^{th} nucleus. m and M_i are the mass of an electron and the i^{th} nucleus, respectively. Equation (2.31) is expressed in the shorthand notation for the five terms in Eq. (2.32) and these terms are electron KE, electron-electron PE, nuclear KE, nuclear-nuclear PE and electron-nuclear PE. The time-independent Schrödinger equation (TISE) of a molecule is given as

$$\hat{H}\Psi(r, R) = E\Psi(r, R), \tag{2.33}$$

where $\Psi(r, R)$ is the eigenfunction of the total molecular Hamiltonian, $\hat{H}$. Nuclei move slowly as compared to electrons because they are about a thousand times heavier than electrons. Therefore, it is reasonable to treat electronic and nuclear motion separately. Therefore, the total electronic-nuclear adiabatic wave function can be expressed as

$$\Psi(r, R) = \psi(r; R)\phi(R), \tag{2.34}$$

where $\psi(r;R)$ and $\phi(R)$ are the electronic wave function and nuclear wave function, respectively. The TISE for electrons at a fixed nuclear structure, R is given as

$$\hat{H}_e\psi(r;R) = E_e(R)\psi(r;R), \tag{2.35}$$

where $\hat{H}_e = \hat{T}_e + \hat{V}_e + \hat{V}_{eN}$ and $E_e(R)$ is the eigenvalue of the electronic Hamiltonian, $\hat{H}_e$. Substituting the electronic-nuclear wave function [Eq. (2.34)] into Eq. (2.33), we obtain

$$\begin{aligned}\hat{H}\{\psi(r;R)\phi(R)\} &= \{E_e(R) + V_N\}\{\psi(r;R)\phi(R)\} + \sum_i -\frac{\hbar^2}{2M_i}\{\psi(r;R)\nabla^2\phi(R) \\ &+ 2\nabla\psi(r;R)\cdot\nabla\phi(R) + \nabla^2\psi(r;R)\phi(R)\} \\ &= E\psi(r;R)\phi(R).\end{aligned} \tag{2.36}$$

In the above equation, ∇ refers ∇_N and henceforth we will follow this notation. The first-order differentiation of the electronic wave function with respect to nuclear coordinates [Eq. (2.36)] is referred to as the first-order derivative coupling and it is a vector quantity. This coupling term contributes significantly to the nonadiabatic correction. The second-order derivative coupling term in Eq. (2.36) is a scalar quantity. These two derivative coupling terms are proportional to the ratio of the mass of electrons to the mass of nuclei to a power of (1/4) [134]. Therefore, these terms are smaller as compared to other terms in Eq. (2.36). Hence, these coupling terms can be avoided and it results the approximate TISE for the nuclei,

$$\hat{H}\phi(R) = \{\hat{T}_N + E_e(R) + V_N\} = E\phi(R). \tag{2.37}$$

The above equation is called as the BO approximation. In the above equation, $E_e(R) + V_N$ is the effective potential (in which V_N is a constant at a fixed nuclear geometry) for the nuclei. The above equation indicates that the TISE for the electrons should be solved for different values of R to construct the effective potential. The nuclei move under these effective potentials which are known as adiabatic potentials. In the region of a conical intersection, $\nabla\psi(r;R)$

term becomes large. The derivative coupling terms diverge (can be ascertained through the Hellmann-Feynman theorem) at the degenerate point of adiabatic potentials. In this situation, the BO approximation fails and solving nuclear dynamics becomes cumbersome. In order to overcome such difficulties, the diabatic electronic basis is very much useful as the derivative coupling terms become as small as possible in the diabatic representation. Therefore, diabatic electronic basis functions are the convenient choice for coupled electronic states. Before discussing the diabatic representation, it is important to introduce the adiabatic electronic representation.

2.2.2 Adiabatic electronic representation

In the adiabatic representation, the total molecular wave function reads,

$$\Psi(r,R) = \sum_{n=0}^{\infty} \psi_n(r;R)\phi_n(R). \tag{2.38}$$

The electronic wave functions satisfy the conditions of normalization and orthogonalization and these conditions are given as

$$\langle \psi_m | \psi_n \rangle = \delta_{mn}. \tag{2.39}$$

Substituting Eq. (2.38) into Eq. (2.33) and taking projection with $\psi_m(r;R)$ from the left results the following equations,

$$\begin{aligned} \sum_n \hat{H}_{mn}(R)\phi_n(R) &= \sum_n \Big[\{\hat{T}_N + E_e(R) + V(R)\}\delta_{mn} \\ +2\tau^{(1)}_{mn}(R)\cdot\nabla + \tau^{(2)}_{mn}(R)\Big]\phi_n(R) &= E\phi_m(R), \end{aligned} \tag{2.40}$$

where,

$$\tau^{(1)}_{mn}(R) = \langle \psi_m | \nabla | \psi_n \rangle, \tag{2.41}$$

$$\tau^{(2)}_{mn}(R) = \langle \psi_m | \nabla^2 | \psi_n \rangle, \tag{2.42}$$

$$H_{mn}(R) = \langle \psi_m | \hat{H}(r,R) | \psi_n \rangle. \tag{2.43}$$

It is noted that $\tau^{(1)}_{mn}$ is a vector whereas $\tau^{(2)}_{mn}$ is a scalar quantity. The matrix $\tau^{(1)}_{mn}$ [Eq. (2.41)] is an anti-hermitian, i.e.,

$$\tau^{(1)}_{mn}(R) = -\tau^{(1)*}_{nm}(R). \tag{2.44}$$

The diagonal elements vanish for the real-valued electronic wave function,

$$\tau^{(1)}_{nn}(R) = 0. \tag{2.45}$$

We get the adiabatic TISE for the nuclei by retaining the diagonal terms of Eq. (2.40),

$$\{\hat{T}_N + E_{e,n}(R) + V_N(R) + \tau^{(2)}_{nn}(R)\}\phi_n(R) = E\phi_n(R). \tag{2.46}$$

The derivative coupling terms are discussed above in Eqs. (2.36), (2.46) and (2.40) can be quite large around a conical intersection (CI). In such situations, it is convenient to use the diabatic basis to solve the nuclear dynamics. We discuss briefly the adiabatic-to-diabatic transformation below.

2.2.3 Adiabatic to diabatic transformation

To avoid the singularity of the matrix, τ, one needs to perform the adiabatic-to-diabatic transformation where the adiabatic wave functions, $\psi^a(r;R)$ are replaced by the diabatic wave functions, $\psi^d(r;R)$ which are smooth and slowly varying functions [135] of nuclear coordinates and correspond to the potential energy surfaces (PESs) that may cross at the CIs of the adiabatic PESs. These smooth and slowly varying wave functions are referred to as the diabatic basis [135–139]. The diabatic Hamiltonian ($\mathbf{H}^d$) obtained by a suitable unitary transformation of the adiabatic Hamiltonian ($\mathbf{H}^a$) is given as

$$\mathbf{H}^d = \mathbf{S}\mathbf{H}^a\mathbf{S}^\dagger = T_n\mathbf{1} + \mathbf{U}, \tag{2.47}$$

where $\mathbf{U}$ is the diabatic PE matrix and a and d denote adiabatic and diabatic, respectively. The elements of the diabatic PE matrix, $\mathbf{U}$ are smooth functions of

nuclear coordinates. The diagonal elements represent PESs of electronic states in the diabatic representation. The off-diagonal elements describe the coupling between different states.

The **S** matrix is a unitary matrix, denoted the diabatic-to-adiabatic transformation matrix. For 2×2 Hamiltonian, it is given as

$$\mathbf{S} = \begin{pmatrix} cos\alpha & sin\alpha \\ -sin\alpha & cos\alpha \end{pmatrix}, \tag{2.48}$$

where α is the adiabatic-to-diabatic transformation (ADT) angle. The adiabatic nuclear basis can be transformed to the diabatic nuclear basis using the $\mathbf{S}(R)$ matrix,

$$\phi^a(R) = \mathbf{S}(R)\phi^d(R). \tag{2.49}$$

The adiabatic PE matrix, **V** is calculated by diagonalizing the diabatic PE matrix as follows

$$\mathbf{V} = \mathbf{S}\mathbf{U}\mathbf{S}^\dagger. \tag{2.50}$$

Dipole moments (DMs) and transition dipole moments (TDMs) are important for the dynamics of systems interacting with laser light. The diabatic DMs and TDMs are calculated using the equation as follows

$$\boldsymbol{\mu}^a = \mathbf{S}\boldsymbol{\mu}^d\mathbf{S}^\dagger. \tag{2.51}$$

In this work, the diabatic dipole moments are used in the control calculations.

2.2.4 Conical intersection and geometric phase

The PE matrix for a diatomic molecule, **U** in the diabatic representation is given as

$$\mathbf{U} = \begin{pmatrix} U_{11} & U_{12} \\ U_{21} & U_{22} \end{pmatrix}, \tag{2.52}$$

where U_{11} and U_{22} are the diabatic potential curves along the internuclear distance, R and U_{12} and U_{21} are the interstate diabatic coupling elements.

Diagonalization of the diabatic PE matrix results the adiabatic potentials, $V_{\pm}$ as follows

$$V_{\pm} = \frac{U_{11} + U_{22}}{2} \pm \frac{1}{2}\sqrt{(U_{11} - U_{22})^2 + 4|U_{12}|^2}. \tag{2.53}$$

The energy difference between the adiabatic potential curves is given as

$$\Delta V = V_{+} - V_{-} = \sqrt{(U_{11} - U_{22})^2 + 4|U_{12}|^2}. \tag{2.54}$$

The conditions given below give rise to the degeneracy of the adiabatic potentials given in Eq. (2.53)

$$U_{11} = U_{22}, \tag{2.55}$$

and

$$U_{12} = 0. \tag{2.56}$$

It is unlikely that the above two conditions are fulfilled for two electronic states of the same symmetry for one degree of freedom i.e., the internuclear distance, R of the diatomic molecule. Therefore, for a diatomic molecule, the PE curves corresponding to the same symmetry electronic states do not cross resulting the *avoided crossing* [140]. This phenomenon is referred to as the non-crossing rule. As there are more than one degrees of freedom for polyatomic molecules, PESs can intersect and exhibit conical intersections (CIs) [141].

For polyatomic molecules, CIs are degenerate points (or hyperlines) of adiabatic PE surfaces in the multidimensional nuclear coordinates. Electronic wave functions associated with these PE surfaces degenerate at a CI [141–145]. CI forms a double cone in the region around the degeneracy of PESs. In the region of a CI point, there are two distinguished nuclear coordinates, x_1 and x_2 and movement along these coordinates lifts the degeneracy [143]. The derivative coupling elements (discussed above) are large near, and singular at a CI. CIs results two important processes, i.e., the nonadiabatic transition and geometric phase effect [146, 147]. The nonadiabatic transition occurs from an

upper state to a lower state as well as from a lower state to an upper state. Ultrafast photochemical reactions (e.g., photodissociation) take place because of the nonadiabatic transition. Also CIs result the geometric phase effect. When two parts of a nuclear wave function evolve around a CI in a clockwise and an anti-clockwise fashion, they interfere destructively. As a result nodal patterns are introduced in the nuclear wave function. [148]. We discussed the geometric phase effect in **Chap.** 5 and **Chap.** 6.

2.2.5 Symmetry selection rule

The selection of the coupling mode and the tuning mode is very important for the characterization of the conical intersection. The irreducible representation of the electronic Hamiltonian is always totally symmetric. The intrastate coupling constant is given as

$$\kappa_{t,n} = \langle \phi_n | \frac{\partial \hat{H}_{el}}{\partial Q_t} | \phi_n \rangle |_{Q_0}. \tag{2.57}$$

In the above equation, $\frac{\partial \hat{H}_{el}}{\partial Q_t}$ is the gradient of the electronic Hamiltonian and it is totally symmetric. Therefore, it is clear that the totally symmetric vibrational mode results to a nonvanishing intrastate coupling constant. The interstate coupling between two electronic states can be described by the symmetry properties of the coupling mode and electronic states. The interstate coupling element is given as

$$\lambda_{mn} = \frac{\partial}{\partial Q_c} \langle \phi_m | \hat{H}_{el} | \phi_n \rangle |_{Q_0}. \tag{2.58}$$

The direct product of the irreducible representation of the coupling mode and the electronic states is given as

$$\Gamma_1 \times \Gamma_{Q_c} \times \Gamma_2 \supset A_1 \Rightarrow \Gamma_{Q_c} = \Gamma_1 \times \Gamma_2. \tag{2.59}$$

Therefore, non-totally symmetric modes result non-zero interstate coupling constants. When two states of the same symmetry intersect, they result

"accidental CIs". In that scenario, both the coupling and tuning modes are totally symmetric [135].

2.3 Optimal control theory

Optimal control theory (OCT) is a broad subject that provides a mathematical framework to manipulate behavior of a dynamical system in the presence of an external control. Optimal control theory [149] finds the best solution to various control problems subject to practical constraints. For a control problem, a particular objective is achieved through the judgment of a performance index functional which depends upon the state of the system and control variables. Optimal control theory (OCT) is a branch of mathematical optimization with several applications of a wide range of fields, e.g., science, engineering, etc. [150, 151].

A quantum mechanical formalism for designing an optical laser field to control the chemical reactivity is developed based on optimal control theory. A cost functional is constructed by incorporating an objective and constraints. The designed optimal field, which successfully drives systems to a desired molecular state [152, 153]. In the present work, optimal laser pulses are designed to manipulate quantum dynamics of molecular systems. Those control problems are studied in the mathematical framework of OCT. The dynamics of a quantum mechanical system is described by the TDSE. The TDSE within the semiclassical dipole approximation [87, 154] reads as,

$$i\hbar\frac{\partial}{\partial t}|\Psi(t)\rangle = [\hat{H}_0 - \hat{\boldsymbol{\mu}}.\boldsymbol{\epsilon}(t)]|\Psi(t)\rangle. \tag{2.60}$$

In the above equation, $\hat{H}_0$ is the field-free Hamiltonian and $-\hat{\boldsymbol{\mu}}.\boldsymbol{\epsilon}(t)$ is the laser-molecule interaction term.

As discussed above, an optimal laser pulse is constructed in the mathematical framework of OCT in combination with the TDSE to control the dynamical behavior of a quantum mechanical system. Laser pulse parameters are varied in the optimization process to optimize a specific outcome of a molecular process. In the optimization process, varying temporal and spectral profile connects an initial state to a product state through various pathways. For an optimal solution of the laser pulse, the constructive interference among possible pathways optimizes the product yield. The mathematical formulation of OCT is discussed below.

2.3.1 Formulation

In the mathematical framework of OCT, a cost functional is constructed using an objective function, the laser field energy and the TDSE as a dynamical constraint. The objective of a quantum mechanical system is constructed in terms of the expectation value of a certain physical observable, $\hat{O}$, at a desired target state, $\psi(T)$ or at the product channel of a chemical reaction. In the presence of a suitable laser pulse, the objective function is maximized to steer a system to the target state [81, 155–158]. An optimal laser pulse for a laser field-induced process is designed by optimizing the field-dependent cost functional. As discussed earlier, the cost functional mainly has three terms and it is expressed as

$$J[\epsilon(t)] = J_0 + J_p + J_c. \tag{2.61}$$

In the above equation, the first term, J_0 is the physical objective that measures the extent of the achievement of a desired target state. The 2nd term, J_p is a constraint term that includes the penalty on the control field to keep away from any undesirable processes. Finally, the third term is a dynamical constraint such that the system must follow the TDSE.

The objective term can be expressed in a time-independent or in a time-dependent formalism depending on the desired goal of a problem. The time-independent objective is determined in problems where a laser pulse drives the initial state, $\psi(0) = \phi_i$ into the desired target state, $\psi(T)$ at the end of the time duration. Typically, the time-independent objective is relevant in the control scenario of a state-selective population transfer process. In these cases, the expectation value of the target operator consisting of the desired final state, $\psi(T)$ is maximized in the optimization procedure (discussed below). For the time-dependent objective [159], the expectation value of the target operator is maximized. In the photodissociation control, the target operator i.e., the flux operator calculates outgoing flux through a dividing surface at each point of time (discussed below). As discussed earlier, the time-independent objective can be expressed as

$$J_0 = \langle\psi(T)|\hat{O}|\psi(T)\rangle. \tag{2.62}$$

For the state selective population transfer, the projection operator, $\hat{O}$ can be defined as $\hat{O} = |\phi_f\rangle\langle\phi_f|$, where $\hat{O} = |\phi_f\rangle$ is the predefined target state. Hence, the time-independent objective can be re-expressed as

$$J_0 = \langle\psi(T)|\phi_f\rangle\langle\phi_f|\psi(T)\rangle = |\langle\psi(T)|\phi_f\rangle|^2. \tag{2.63}$$

The above equation indicates that the overlap of the field-driven initial state with the target state determines the objective. Similarly, the objective for the time-dependent control targets has the form,

$$J_0 = \langle\psi(t)|\hat{O}|\psi(t)\rangle. \tag{2.64}$$

In the case of photodissociation problems, the dissociative flux is determined by calculating the expectation value of the flux operator. Hence, the objective of a photodissociation problem is rewritten as

$$J_0 = \int_0^T \langle\psi(t)|\hat{F}_R|\psi(t)\rangle dt, \tag{2.65}$$

where $\hat{F}_R$ is the flux operator (discussed in detail later). The flux operator reads as

$$\hat{F}_R = \frac{1}{2}\left\{\frac{\hat{p}_R}{m}\delta(R - R_\infty) + \delta(R - R_\infty)\frac{\hat{p}_R}{m}\right\}, \tag{2.66}$$

where $\hat{p}_R = -i\frac{\partial}{\partial R}$ (using atomic units) and m is the reduced mass of the molecule. The quantity R_∞ is a chosen coordinate at a large distance. The second term, J_p is a fluence (penalty) that represents a constraint on the control field for achieving a desired outcome in a field-driven process. The mathematical form of this term, introduced by Rabitz and co-workers is given as

$$J_p = -\alpha_0 \int_0^T |\boldsymbol{\epsilon}(t)|^2 dt, \tag{2.67}$$

where α_0 is a constant penalty factor and it specifies a constraint on the total laser field fluence, $\int_0^T |\boldsymbol{\epsilon}(t)|^2 dt$. It adjusts the contribution of the laser field intensity to the cost functional. Therefore, overall, the penalty term avoids undesirable processes by limiting the laser field intensity. The third term, J_c is a dynamical constraint to the cost functional. In this mathematical framework, the dynamical constraint is the TDSE that systems must follow.

Rabitz and co-workers [156, 157] formulated the cost functional expression for a quantum control problem in a more general way and is given by (using atomic units),

$$J[\epsilon(t)] = \lim_{T\to\infty} \langle\psi(T)|\hat{O}|\psi(T)\rangle - \alpha_o \int_0^T [\epsilon(t)]^2 dt - 2Re\left[\int_0^T \langle\chi(t)\left|\frac{\partial}{\partial t} + i\hat{H}\right|\psi(t)\rangle dt\right] \tag{2.68}$$

In the above equation, $\psi(t)$ is the time-evolved wave function in the presence of the time-dependent laser field, $\epsilon(t)$ and $\psi(T)$ is the wave function at time t=T. The quantity, α_0 is a penalty factor (discussed earlier) to limit the contribution of the laser field intensity to the cost functional. The Lagrange multiplier, $\chi(t)$ ensures the dynamics of a system to follow the TDSE and provides feedback to optimization algorithms.

The Hamiltonian for two electronic states within the semiclassical dipole approximation is expressed as

$$\hat{H} = \begin{pmatrix} \hat{H}_e & -\hat{\boldsymbol{\mu}}.\boldsymbol{\epsilon}^*(t) \\ -\hat{\boldsymbol{\mu}}.\boldsymbol{\epsilon}(t) & \hat{H}_g \end{pmatrix}, \tag{2.69}$$

where $\hat{\boldsymbol{\mu}}$ is the transition dipole moment. $\hat{H}_g$ and $\hat{H}_e$ are Hamiltonians of the ground electronic state and the excited state, respectively in the field-free condition. In this model system, the Lagrange multiplier and the wave function are given as

$$\psi = \begin{pmatrix} \psi_e \\ \psi_g \end{pmatrix}; \;\; \chi = \begin{pmatrix} \chi_e \\ \chi_g \end{pmatrix}. \tag{2.70}$$

Here, we consider the variation of the cost functional, J with respect to the χ, ψ and ϵ using the calculus of variation. At the optimal condition, the first-order variation is zero and it results into non-linear coupled differential equations (See Appendix for the derivation). These equations are called the pulse design equations and given as

$$\frac{\partial J}{\partial \chi(t)} = 0 \Rightarrow i\frac{\partial \psi(t)}{\partial t} = \hat{H}\psi(t), \psi(t=0) = \psi(0), \tag{2.71}$$

$$\frac{\partial J}{\partial \psi(t)} = 0 \Rightarrow i\frac{\partial \chi(t)}{\partial t} = \hat{H}\chi(t), \chi(T) = \hat{O}\psi(T), \tag{2.72}$$

$$\frac{\partial J}{\partial \boldsymbol{\epsilon}^*(t)} = 0 \Rightarrow \boldsymbol{\epsilon}(t) = \frac{i}{\alpha_0}[\langle \chi_e(t)|\hat{\boldsymbol{\mu}}|\psi_g(t)\rangle - \langle \psi_e(t)|\hat{\boldsymbol{\mu}}|\chi_g(t)\rangle]. \tag{2.73}$$

The optimal solution of a laser pulse can be achieved by solving these coupled differential equations. Equation (2.71) implies that the wave function $\psi(t)$ must follow the TDSE with the initial condition, $\psi(0) = \phi_i$. Equation (2.72) states that the Lagrange multiplier, $\chi(t)$, must obey the TDSE with the boundary condition, $\chi(T) = \hat{O}\psi(T)$. As this boundary condition is defined at the end of the pulse, one needs to integrate the TDSE backward in time to obtain $\chi(t)$. Equation (2.73) determines the optimal laser pulse, $\epsilon(t)$ using the time-dependent wave function, $\psi(t)$ and the Lagrange multiplier, $\chi(t)$. These coupled differential equations can be solved iteratively. Various numerical methods [81, 158] have been developed to

solve these equations. However, These methods are found to be inefficient. There are two efficient alternatives to these iterative methods, namely the conjugate gradient method and the genetic algorithm. The conjugate gradient method is a gradient-based algorithm, whereas the genetic algorithm is based on principles of genetics. In the conjugate gradient algorithm [79, 89, 160, 161], the derivative of the cost functional with respect to the electric field is treated as the central object. On the other hand, the cost functional is directly optimized in the genetic algorithm. Both these algorithms are discussed in detail below.

2.3.1.1 Conjugate gradient method

The laser pulse, $\epsilon(t)$ in the conjugate gradient method [89, 90, 162, 163] has the form [89]

$$\epsilon(t) = \epsilon_0(t).\mathrm{s}(t), \tag{2.74}$$

where $\epsilon_0(t)$ is a sinusoidal electric field. In the above equation, s(t) is an envelope function that ensures a smooth switch on/off of the time-dependent electric field. s(t) is often assumed as a Gaussian function [162],

$$\mathrm{s}(t) = exp\frac{-(t-T/2)^2}{(T/4)^2}. \tag{2.75}$$

In the above equation, T is the total timescale. The gradient of the cost functional with reference to the initial laser pulse, $\epsilon_0(t)$ after k^{th} number of iterations is expressed as

$$g^k(t) = \frac{\partial J^k}{\partial \epsilon_0^k(t)}, \tag{2.76}$$

$$= -2s(t)\left[\alpha_0\epsilon^k(t) - Im\langle\chi(t)|\frac{\partial\hat{H}}{\partial\epsilon^k(t)}|\psi(t)\rangle\right]. \tag{2.77}$$

$\psi(t)$ and $\chi(t)$ follow the TDSE and are solved using the SO method. The time evolution is carried out in discrete time steps (t_i). In the conjugate gradient algorithm, the parameter space of laser fields, $\epsilon(t_i)$ is searched along

the Polak–Ribiere–Polyak search direction [164] to maximize the cost functional. The search direction, d after k^{th} number of iterations is expressed as

$$d^k(t_i) = g^k(t_i) + \lambda^k . d^{k-1}(t_i). \tag{2.78}$$

In the above equation, λ is the conjugate gradient parameter, given by

$$\lambda^k = \frac{\sum_i g^k(t_i)^T (g^k(t_i) - g^{k-1}(t_i))}{\sum_i g^{k-1}(t_i)^T g^{k-1}(t_i)}, \tag{2.79}$$

where, k=2,3,..., and T denotes the transpose. To restrict the algorithm from sampling $\epsilon(t_i)$ values outside of a predefined amplitude range $[\epsilon_{min}, \epsilon_{max}]$ during the line search, the direction is projected [165] appropriately.

During the optimization process, the frequency spectrum of a laser pulse is restricted within a predefined range [166] as to get a simple profile of it. The frequency function is filtered with a 20^{th}-order Butterworth band pass filter [167]. The filter is given as

$$h(\omega) = \left[\left(1 + \left(\frac{\omega_{min}}{\omega} \right)^{40} \right) \left(1 + \left(\frac{\omega}{\omega_{max}} \right)^{40} \right) \right]^{-\frac{1}{2}}. \tag{2.80}$$

The frequency spectrum of the projected search direction is calculated from the Fourier transformation method and it is multiplied with h(ω), and then transform into the time domain with the expression given below,

$$d^k_{p,filter}(t) = \int h(\omega) F_\omega [d^k_p(t)] e^{-i\omega t} d\omega. \tag{2.81}$$

In the above equation, $F_\omega[d^k_p(t)]$ is the Fourier component of the line search direction. In the optimization process, the updated electric field, $\epsilon^{k+1}(t_i)$ is expressed as,

$$\epsilon^{k+1}(t_i) = \epsilon^k(t_i) + \lambda s(t_i) d^k_{p,filter}(t), \tag{2.82}$$

where λ is the conjugate gradient parameter and $d^k_{p,filter}(t)$ is the line search direction.

2.3.1.2 Genetic algorithm

The laser pulse in the genetic algorithm [168–170] reads

$$\epsilon_{ga}(t) = \epsilon_0 \sin(\omega t) \cdot \mathrm{s}(t). \tag{2.83}$$

where ω is the carrier frequency of the laser radiation and ϵ_0 is the amplitude of the laser field. $\mathrm{s}(t)$ is an envelope function that modulates the laser field and ensures that the field goes to zero smoothly at the initial and final time. Generally, it is defined by four positive time parameters, t_0, t_1, t_2 and t_3 where $t_0 < t_1 < t_2 < t_3$ and is given as

$$\mathrm{s}(t) = \begin{cases} \sin^2\left[\frac{\pi}{2}\left(\frac{t-t_0}{t_1-t_0}\right)\right] & \text{for} \quad t_0 \leq t \leq t_1, \\ 1 & \text{for} \quad t_1 \leq t \leq t_2, \\ \sin^2\left[\frac{\pi}{2}\left(\frac{t_3-t}{t_3-t_2}\right)\right] & \text{for} \quad t_2 \leq t \leq t_3 = T. \end{cases} \tag{2.84}$$

Normally, t_0 is defined as 0 and t_3 as T. The time duration t_0 to t_1 is the rise time and t_2 to t_3 is the switch-off period of the pulse. The duration t_1 to t_2 is a plateau region where the envelope function reaches the maximum value, 1. The amplitude (ϵ_0), frequency (ω) and two time parameters t_1 and t_2 are varied to maximize the cost functional ($J[\epsilon(t)]$). The genetic algorithm is a global search optimization tool consisting of principles of genetics viz., survival of the fittest, selection, reproduction through crossover combined with mutation or randomization, etc. [see Fig. (2.1)]. Each parameter value is stored in a binary number containing ten bits (0 or 1). The chromosome consists of four parameters string containing a total of 40 bits with different combinations of these parameters. The genetic algorithm finds the optimal solution from the said possibilities. The calculation starts with an initial guess population (population or total number of individuals in a generation, N=10). The individuals (chromosome, a set of parameters, define an electric field) in this population are randomly selected from the parameter space. Using a set of parameters *i.e.*, chromosome, we evaluated the cost functional

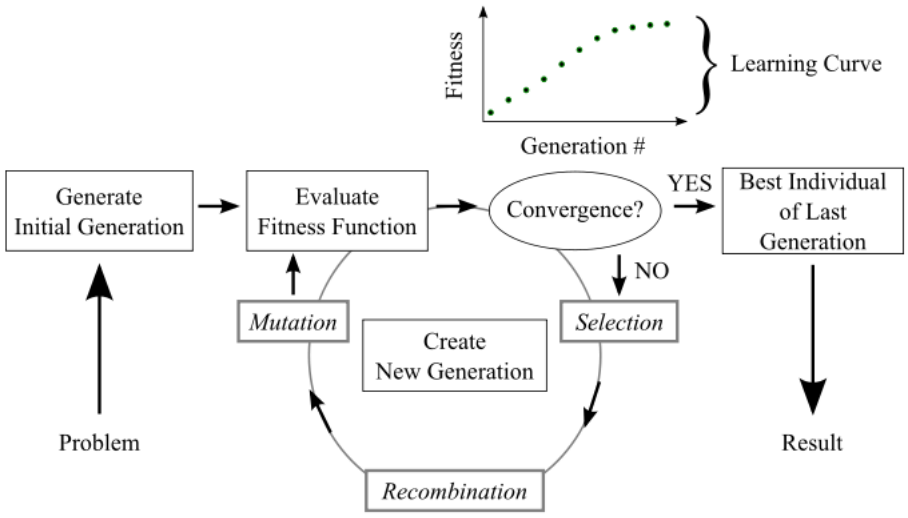

Figure 2.1: The above figure represents the genetic algorithm: Individuals of a generation are subjected to estimate a fitness function that determines the degree of fitness of an individual. The optimization proceeds iteratively through various operations e.g., selection, recombination, mutation, etc. .

expression, which measures its fitness. In the present study, the cost functional value near 1.0 makes the chromosome fitter for survival. The population evolves through various genetic operations like tournament selection, elitism, mutation and crossover as suggested in Ref. [169]. These operations are performed in every generation until the convergence of the cost functional is achieved. In the present work, the genetic algorithm has been found to work well to reach the convergence criteria of cost functional.

2.4 Time propagation

The time evolution of a quantum mechanical system is described by the TDSE,

$$i\hbar\frac{\partial}{\partial t}|\Psi(x,t)\rangle = \hat{H}|\Psi(x,t)\rangle, \tag{2.85}$$

where $\Psi(x,t)$ is the wave function and $\hat{H}$ is the Hamiltonian operator of the system. The solution of the above equation provides dynamical properties of the

system. For an explicitly time-independent Hamiltonian, $\hat{H}$, the solution of the above equation is given as

$$\Psi(x,t) = e^{-\frac{i\hat{H}t}{\hbar}}\Psi(x,0), \tag{2.86}$$

where $\Psi(x,0)$ is the wave function at time, $t = 0$. It is clear from the above equation that the Hamiltonian operator, $\hat{H}$ operates on the initial wave function, $\Psi(x,0)$ to get the solution. For an explicitly time-dependent Hamiltonian, the solution is approximated by assuming the Hamiltonian as a constant for a small-time interval, dt reads,

$$\Psi(x,t+dt) \approx e^{-\frac{i\hat{H}dt}{\hbar}}\Psi(x,t), \tag{2.87}$$

where dt is the width of the time increment and it determines the accuracy of the solution. Therefore, a more accurate solution is obtained from the smaller time increment. The total time, T is divided into N steps with the time increment, dt, where $T = Ndt$. The wave function at the final time, T i.e., $\Psi(x,T)$ is expressed as the product of the time propagators follows as

$$\Psi(x,T) = \hat{O}(Ndt)\hat{O}((N-1)dt)...\cdots\hat{O}(dt)\Psi(x,0), \tag{2.88}$$

where $\hat{O}(dt)$ is a short-time propagator,

$$\hat{O}(dt) = e^{-\frac{i\hat{H}}{\hbar}dt} = e^{-i\frac{\hat{T}+\hat{V}}{\hbar}dt}. \tag{2.89}$$

The Hamiltonian operator, $\hat{H}$ contains the kinetic energy operator, $\hat{T}$ and the PE operator, $\hat{V}$ (shown in the above equation). The PE operator is best treated in coordinate representation as it is local in the coordinate space (i.e., can be diagonalized). Therefore, the operation of the PE operator on Ψ is calculated by simple multiplication in the coordinate representation. On the contrary, the kinetic energy operator is best treated in the momentum representation as it is local in the momentum space (i.e., can be diagonalized). Therefore, one needs to move back and forth between these two representations. Fourier transformation

method do this task naturally. In the grid representation, Fourier transformation provides a reliable and robust method called the Fourier-grid method [171, 172].

2.4.1 Coordinate and momentum space and the role of the Fourier transformation method

The Fourier-grid method is used to transform from the coordinate representation to the momentum representation and vice versa on a grid of evenly spaced points. The transformation between these two representations is performed using the Fourier transformation method. Actions of the kinetic energy operator and PE operator on the wave function are performed in their local representations. The PE matrix is diagonalized in the coordinate representation and operates on the wave function. The formulation of the one dimensional Fourier grid method [173] is discussed below.

The Hamiltonian, $\hat{H}$ for a particle of mass m moving in one dimension under the influence of a potential, $V(\hat{x})$ is reads as

$$\hat{H} = \hat{T} + \hat{V} = \frac{\hat{p}^2}{2m} + V(\hat{x}), \tag{2.90}$$

where $\hat{p}$ is the momentum operator given as

$$\hat{p} = -i\hbar\frac{\partial}{\partial x}. \tag{2.91}$$

The basic vectors or ket's (Dirac notation) of the coordinate representation, $|x\rangle$ are the eigenfunctions of the position operator, $\hat{x}$, given as

$$\hat{x}|x\rangle = x|x\rangle, \tag{2.92}$$

where x is the eigenvalue of it. The basic vectors, $|x\rangle$ satisfy the orthogonality and completeness relationships as follows

$$\langle x'|x\rangle = \delta(x' - x), \tag{2.93}$$

and

$$\hat{I}_x = \int_{-\infty}^{\infty} |x\rangle\langle x| dx. \tag{2.94}$$

The PE is diagonal in the coordinate representation as follows,

$$\langle x'|V(\hat{x})|x\rangle = V(x)\delta(x' - x). \tag{2.95}$$

The basic vectors or ket's (Dirac notation) of the momentum representation, $|k\rangle$ are the eigenfunctions of the momentum operator, $\hat{p}$,

$$\hat{p}|k\rangle = k\hbar|k\rangle, \tag{2.96}$$

where $k\hbar$ is the eigenvalue of it. The basic vectors, $|k\rangle$ satisfy the orthogonality and completeness relationships as follows

$$\langle k'|k\rangle = \delta(k' - k), \tag{2.97}$$

and

$$\hat{I}_k = \int_{-\infty}^{\infty} |k\rangle\langle k| dk. \tag{2.98}$$

The kinetic energy is diagonal in the momentum representation as follows,

$$\begin{aligned} \langle k'|\hat{T}|k\rangle &= T_k\delta(k' - k), \\ &\equiv \frac{\hbar^2 k^2}{2m}\delta(k' - k). \end{aligned} \tag{2.99}$$

Back-and-forth transformation between the mentioned representations is required to perform operations of the potential and kinetic energy operator on the wave function. This transformation between the coordinate and momentum representations is carried out using the Fourier transforms,

$$\langle k|x\rangle = \frac{1}{(2\pi)^{1/2}} exp(-ikx), \tag{2.100}$$

and

$$\langle x|k\rangle = \frac{1}{(2\pi)^{1/2}} exp(ikx). \tag{2.101}$$

The multidimensional Fourier grid method is developed by Dutta and others [174]. In this work, we have implemented one dimensional as well as two-dimensional Fourier methods to study the nuclear dynamics.

Discretization and grid

For any numerical calculation, we need to replace the continuous variable, x with the grid values. We have discretized into N numbers of evenly spaced grids, $\{x_i\}$,

$$x_i = i\Delta x \qquad i = 1, 2, \cdots, N, \tag{2.102}$$

where the length of the grid is given as $L = N\Delta x$. The grids of the coordinate space, $\{x_i\}$ satisfy the orthogonality condition,

$$\Delta x \langle x_i | x_j \rangle = \delta_{ij}, \tag{2.103}$$

as well as the completeness property,

$$\hat{I}_x = \sum_{i=1}^{N} |x_i\rangle\langle x_i| \Delta x. \tag{2.104}$$

The length of the grid of the coordinate space (L) defines the longest wavelength (λ_{max}) or the smallest frequency. The grid spacing in the reciprocal momentum space defined using the longest wavelength is expressed as

$$\Delta k = \frac{2\pi}{\lambda_{max}} = \frac{2\pi}{L} = \frac{2\pi}{N\Delta x}. \tag{2.105}$$

The grid points in the momentum space are distributed on both sides around zero. The grid in the momentum space, k_l is given as

$$\begin{aligned} k_l &= k_{min} + l\Delta k, \\ &= -\frac{N\pi}{L} + l\frac{2\pi}{L}, \\ &= -\frac{\pi}{\Delta x} + l\frac{2\pi}{N\Delta x}. \end{aligned} \tag{2.106}$$

The implementation of the FFT algorithm [172, 175, 176] increases a significant amount of computational efficiency. The FFT algorithm appears to be an O(NlnN) process to calculate the discrete Fourier transform that has $O(N^2)$ operations. Also, the FFT algorithm does not create and store matrices rather

it rearranges the elements of the vector representing the wave function. Thus, the FFT algorithm saves computational cost significantly for large input vectors. In the next section, we discuss the SO method with the FFT algorithm for the estimation of the operation of the short-time propagator on the wave function.

2.4.2 Split-operator method

The split-operator (SO) method [171, 175, 176] is used for the numerical implementation of the time propagator, $e^{-\frac{i\hat{H}t}{\hbar}}$. In this method, the exponent form of the propagator is retained and it directly operates on the wave function. The PE and kinetic energy operator do not commute i.e., $[\hat{V}, \hat{T}] \neq 0$. Hence, we can not express the short-time propagator as $e^{-\frac{i\hat{T}dt}{\hbar}} e^{-\frac{i\hat{V}dt}{\hbar}}$. The short-time propagator approximated by the symmetrical splitting with reference to the PE operator,

$$e^{-\frac{i\hat{H}dt}{\hbar}} \approx e^{-\frac{i\hat{T}dt}{2\hbar}} e^{-\frac{i\hat{V}dt}{\hbar}} e^{-\frac{i\hat{T}dt}{2\hbar}} + O(dt^3), \tag{2.107}$$

or with reference to the kinetic energy operator,

$$e^{-\frac{i\hat{H}dt}{\hbar}} \approx e^{-\frac{i\hat{V}dt}{2\hbar}} e^{-\frac{i\hat{T}dt}{\hbar}} e^{-\frac{i\hat{V}dt}{2\hbar}} + O(dt^3), \tag{2.108}$$

where $O(dt^3)$, an error function is proportional to the commutator, $[\hat{V}, \hat{T}]$. The time evolution of the wave function is given as

$$\Psi(x, t + dt) \approx e^{-\frac{i\hat{T}dt}{2\hbar}} e^{-\frac{i\hat{V}dt}{\hbar}} e^{-\frac{i\hat{T}dt}{2\hbar}} \Psi(x, t). \tag{2.109}$$

The wave function, $\Psi(x, t)$ is propagated in the following way:

1. In the first step, the wave function in the coordinate representation (x) is transformed to the momentum representation (k) using the FFT. The transformed wave function i.e., $\Psi(k, t)$ is multiplied by $e^{-i\frac{\hbar^2 k^2}{2m}\frac{dt}{2\hbar}}$ (K.E part of SO) i.e., $e^{-i\frac{\hbar^2 k^2}{2m}\frac{dt}{2\hbar}}\ \Psi(k, t)$ where,

$$\Psi(k, t) = FFT\{\Psi(x, t)\} = \frac{1}{(2\pi)^{1/2}} \int_{-\infty}^{\infty} \Psi(x, t) e^{-ikx} dx. \tag{2.110}$$

2. At this step, the wave function in the momentum representation is transformed back to the coordinate representation using the reverse FFT. The resultant wave function in the coordinate representation is then multiplied by $e^{-i\frac{V(x)dt}{\hbar}}$ (P.E part of SO) i.e., $e^{-i\frac{V(x)dt}{\hbar}}\ \Psi(k,t)$ where,

$$\Psi(x,t) = FFT^{-1}\{\Psi(k,t)\} = \frac{1}{(2\pi)^{1/2}}\int_{-\infty}^{\infty}\Psi(k,t)e^{ikx}dk. \tag{2.111}$$

3. The wave function thus obtained is again transformed to the momentum representation and multiplied by $e^{-i\frac{\hbar^2k^2}{2m}\frac{dt}{2\hbar}}$ (other half of K.E part of SO) as discussed in step 1.

In the present work, we have considered a two-dimensional model system for the control problem where R and Q are the tuning mode and coupling mode, respectively. In the two-dimensional model, the short-time propagator is given as (kinetic energy referenced)

$$\hat{U}(dt) = e^{-\frac{i\hat{V}dt}{2\hbar}}e^{-\frac{i\hat{T}_Q dt}{2\hbar}}e^{-\frac{i\hat{T}_R dt}{\hbar}}e^{-\frac{i\hat{T}_Q dt}{2\hbar}}e^{-\frac{i\hat{V}dt}{2\hbar}}, \tag{2.112}$$

where the SO component $e^{-\frac{i\hat{T}_Q dt}{2\hbar}}$ associated with coupling mode (Q) follows the same steps as discussed earlier.

2.5 Physical observables

2.5.1 Flux operator

The flux operator, F estimates the probability of the current density through a dividing surface. The dividing surface is situated at $R = R_f$ and it separates between the reactant and product. The quantum flux operator reads as

$$F = i[\hat{H}, \hat{\Theta}], \tag{2.113}$$

where $\hat{H}$ is a Hamiltonian and $\hat{\Theta}$ is the Heaviside step function, h,

$$\Theta = h(R - R_f), \tag{2.114}$$

$$= \begin{cases} 0, & R < R_f \\ 1, & R > R_f. \end{cases} \tag{2.115}$$

From the above equation, it is clear that the $\hat{\Theta}$ is a function of coordinate and it commutes to the PE operator. The flux operator [177] can be re-expressed as

$$F = [\hat{T}, \hat{\Theta}], \tag{2.116}$$

$$= -\frac{i}{2m}\left\{ \frac{\partial}{\partial R}\frac{\partial}{\partial R}H(R - R_\infty) - H(R - R_\infty)\frac{\partial}{\partial R}\frac{\partial}{\partial R} \right\}, \tag{2.117}$$

$$= -\frac{i}{2m}\left\{ \frac{\partial}{\partial R}\delta(R - R_\infty) + \delta(R - R_\infty)\frac{\partial}{\partial R} \right\}, \tag{2.118}$$

where

$$\hat{T} = -\frac{1}{2m}\frac{\partial^2}{\partial R^2}, \tag{2.119}$$

$$\frac{\partial}{\partial R}H(R - R_f) = \delta(R - R_f), \tag{2.120}$$

$$\text{and} \qquad H(R - R_f)\frac{\partial}{\partial R} = -\delta(R - R_f). \tag{2.121}$$

$\frac{\partial}{\partial R}$ is an anti-hermitian operator i.e., $\frac{\partial}{\partial R}^\dagger = -\frac{\partial}{\partial R}$. The reaction probability on the i^{th} electronic state for the reaction coordinate, R_1 through a dividing surface at $R_1 = R_f$ is given as

$$F_i^D(t) = \int \langle \psi_i(R_1, R_2, .., t)|\hat{F}|\psi_i(R_1, R_2, .., t)\rangle \Big|_{R_1=R_f} dt, \tag{2.122}$$

$$= \frac{1}{\mu}\int Im\left[\langle \psi_i(R_1, R_2, .., t)|\frac{\partial \psi_i(R_1, R_2, .., t)}{\partial R_1}\rangle\right]\Big|_{R_1=R_f} dt. \tag{2.123}$$

In the above equation, the integration is carried out over other coordinates for $R_1 = R_f$. For a photodissociation control problem, the dissociation probability in a given channel is measured at $R_f = R_d$ by the quantum flux.

2.5.2 Probability density

The probability density is estimated from the absolute square of the nuclear wave packet (WP) on an electronic state reads

$$PD_i^{dia}(R_1, R_2, .., t) = |\psi_i^{dia}(R_1, R_2, .., t)|^2, \tag{2.124}$$

$$PD_i^{adia}(R_1, R_2, .., t) = |\psi_i^{adia}(R_1, R_2, .., t)|^2. \tag{2.125}$$

The probability density on the ith diabatic and adiabatic state along a particular nuclear degree of freedom, say R_1 determined by estimating the integration of the square of the nuclear WP for other nuclear degrees of freedom is given as

$$PD_i^{dia}(R_1, t) = \int dR_2 \int dR_3 .. |\psi_i^{dia}(R_1, R_2, .., t)|^2, \tag{2.126}$$

$$PD_i^{adia}(R_1, t) = \int dR_2 \int dR_3 .. |\psi_i^{adia}(R_1, R_2, .., t)|^2. \tag{2.127}$$

2.5.3 Electronic population probability

Mechanisms of the field-driven nuclear dynamics discussed in this thesis are understood from the time-dependent electronic population probability. The time-dependent diabatic and adiabatic electronic populations are estimated by calculating the expectation values of the associated projection operators, $|\psi_i^d\rangle\langle\psi_i^d|$ and $|\psi_i^a\rangle\langle\psi_i^a|$ as

$$P_i^d(t) = \langle\Psi(t)|\psi_i^d\rangle\langle\psi_i^d|\Psi(t)\rangle, \tag{2.128}$$

$$P_i^a(t) = \langle\Psi(t)|\psi_i^a\rangle\langle\psi_i^a|\Psi(t)\rangle. \tag{2.129}$$

The above equations are re-expressed as

$$P_i^{dia}(t) = \int dR_1 \int dR_2 .. |\psi_i^{dia}(R_1, R_2, .., t)|^2, \tag{2.130}$$

$$P_i^{adia}(t) = \int dR_1 \int dR_2 .. |\psi_i^{adia}(R_1, R_2, .., t)|^2. \tag{2.131}$$

For the laser field-induced dissociation works (discussed in **Chap.** 5 and **Chap.** 6), the time-dependent diabatic and adiabatic electronic populations

are determined using the following equations,

$$P_i^{dia}(t) = \int dR_1 \int dR_2..|\psi_i^{dia}(R_1, R_2, .., t)|^2 + F_i^D(t), \tag{2.132}$$

$$P_i^{adia}(t) = \int dR_1 \int dR_2..|\psi_i^{adia}(R_1, R_2, .., t)|^2 + F_i^D(t), \tag{2.133}$$

where $F_i^D(t)$ is the time accumulated dissociation probability (discussed earlier) for a particular channel.

2.5.4 Spectral intensity

Vibrational eigenfunctions of the ground electronic state are estimated using the spectral method [178, 179]. A suitable chosen Gaussian function as an initial state is propagated on the ground electronic state. The autocorrelation function, $C(t)$ is calculated from the time evolved-wave function and is given by

$$C(t) = \langle \psi(t_0)|\psi(t)\rangle. \tag{2.134}$$

The pseudo-spectral intensity is estimated using the autocorrelation function given above as

$$I(E) = \int_0^\infty C(t)e^{iEt/\hbar}dt. \tag{2.135}$$

Eigenvalues are calculated from peak maxima of the frequency spectrum. The eigenfunctions are determined by filtering the time-evolved wave function as follows

$$\psi_n = \int_0^\infty \psi(t)e^{iE_nt/\hbar}dt. \tag{2.136}$$

The energy resolution can be improved (by a factor of 2) using the relation,

$$C(2t) = \langle \psi(t)^*|\psi(t)\rangle. \tag{2.137}$$

Chapter 3

Control of vibrational transitions in 4(3H)-pyrimidinone/4-hydroxypyrimidine system

3.1 Introduction

4(3H)-pyrimidinone is a parent molecule of various important pyrimidine nucleobases (uracil, thymine and cytosine) those are essential building blocks of genetic materials. Therefore, experimental and theoretical investigations [180, 181] of the molecule are important to understand its chemistry.

The prototropic tautomerism is an important phenomenon in biological systems, especially in the structure of nucleic acids. 4(3H)-pyrimidinone is a good model compound for the study of the prototropic tautomerism of various heterocyclic compounds. In the tautomeric equilibrium [182, 183], 4(3H)-pyrimidinone (oxo tautomer) is converted to 4-hydroxypyrimidine (hydroxy tautomer) through the intramolecular hydrogen transfer reaction. The molecule co-exists in the (∼1:1) tautomeric equilibrium [182–186] with the hydroxy tautomer in the gas phase and inert gas (Ar and Ne) matrices. The tautomeric equilibrium of 4(3H)-pyrimidinone has been studied experimentally in IR spectroscopy [182, 183], X-ray photoemission spectroscopy [186], free jet

millimeter wave spectroscopy [185], NMR spectroscopy [184], etc. IR spectra of 4(3H)-pyrimidinone and 4-hydroxypyrimidine have been studied theoretically using various *ab initio* methods [187]. Leś *et al.* [188] explained theoretically the temperature-dependent population of tautomeric forms in the gas phase as well as the environmental effect on the tautomeric equilibrium. Galvão *et al.* [189] investigated theoretically (with the help of *Ab initio* calculations) the stability of 4(3H)-pyrimidinone in the tautomeric equilibrium.

Upon exposure to the UV light (< 310 nm), 4(3H)-pyrimidinone tautomer is converted to 4-hydroxypyrimidine tautomeric form [190–194]. In this reaction, the intramolecular hydrogen transfer reaction occurs between the tautomers. In general, the excited state proton transfer (ESPT) reaction occurs through an intermolecular or intramolecular hydrogen bond. In this tautomerization, the intramolecular hydrogen transfer reaction takes place without having an intramolecular or intermolecular hydrogen bond. The photo-induced tautomeric conversion of 4(3H)-pyrimidinone was theoretically [191, 193, 195, 196] studied using various methods of quantum chemistry. *Ab initio* studies combined with IR spectroscopy to separate the tautomeric forms based on the phototautomeric effect. Theoretical studies were reported to explain the mechanism of the reaction as well as the stability of the isomers. Nowak *et al.* [196] reported that various electronic states (the ground, $\pi\pi^*$, $n\pi^*$ and $\pi\sigma^*$ states) are associated with the photo-induced oxo-hydroxy tautomerization. These electronic states are nonadiabatically coupled in the photo-induced tautomerization reaction.

Controlling an outcome of a quantum mechanical system by a laser field has been developed within the mathematical framework of optimal control theory (OCT) [81, 155–157, 197, 198]. A cost functional is constructed mathematically with the terms namely an objective term, the fluence term related to the

field intensity and time-dependent Schrödinger equation (TDSE). Various optimization methods e.g., gradient-based algorithms and the genetic algorithm are used to optimize a specific product of a reaction by constructing a suitable laser pulse. An optimal laser pulse is designed in the process of the maximization of the cost functional and minimization of the field intensity. The optimal laser pulse steers a system to follow a specific path that optimizes a desired outcome.

In this chapter, the controlled preparation of vibrational eigenstates is performed in OCT in combination with the TDSE. The model system consists of the ground electronic state along the OH stretching coordinate. The obtained potential function is an asymmetric double well. Vibrational eigenstates localized in geometries of 4(3H)-pyrimidinone and 4-hydroxypyrimidine are abbreviated to as opmd (v=n) and hpmd (v=n), respectively, where n is the number of nodes [see Fig. (3.4)]. Optimal laser pulses are designed for various vibrational transitions employing the conjugate gradient method. The optimal IR laser pulse for a particular vibrational excitation is obtained from the optimization.

In the present study, various vibrational transitions are considered and are given by

$$\text{opmd (v=0)} \longrightarrow \text{opmd (v=1)}$$
$$\text{opmd (v=0)} \longrightarrow \text{opmd (v=2)}$$
$$\text{opmd (v=3)} \longrightarrow \text{opmd (v=4)}$$
$$\text{opmd (v=0)} \longrightarrow \text{hpmd (v=0)}$$

These selective vibrational excitations are controlled for the timescales of 30000, 60000 and 90000 a.u. with two penalty factor values i.e., 0.01 and 0.1.

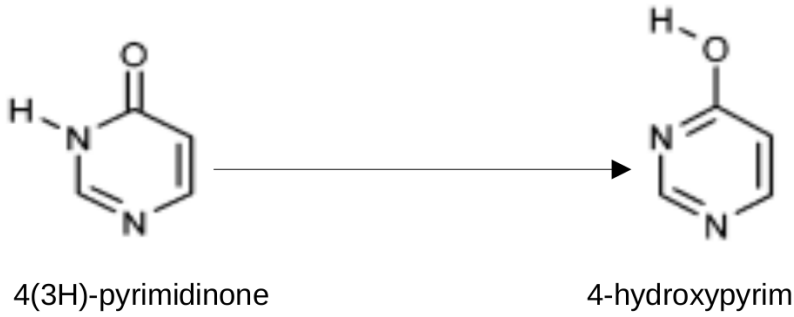

Figure 3.1: The above plot represents the tautomeric conversion from 4(3H)-pyridinone to 4-hydroxypyrimidine.

3.2 Theoretical framework

3.2.1 *Ab initio* calculations

Here, the tautomerization of (3H)-pyrimidinone to 4-hydroxypyrimidine, is studied in the presence of the optimal laser pulses. The model system considered here consists of the ground electronic state along the OH bond distance of the 4(3H)-pyrimidinone/4-hydroxypyrimidine system. The OH bond distance is treated as the reaction coordinate. Equilibrium geometries of both the tautomers are optimized in the second-order Møller–Plesset perturbation (MP2) method with an aug-cc-pVDZ basis set using the Gaussian package. The ground electronic state potential function is calculated using optimized geometries at various OH bond distances. These optimized geometries are obtained from the MP2 method employing the Gaussian package. Single point energies corresponding to these optimized geometries are calculated using the Coupled-Cluster Singles and Doubles (CCSD) method. The dipole moment (DM) is calculated employing the complete-active-space self-consistent-field (CASSCF) method (14 electrons in 11 orbitals) using the Molpro package [199]. The *ab initio* calculated data of the potential energy surface (PES) and DM are fitted with polynomial functions,

$$V(r) = \sum_{n=0}^{6} a_n r^n + b_1(1 - exp(-b_2(r - r_0)))^2, \tag{3.1}$$

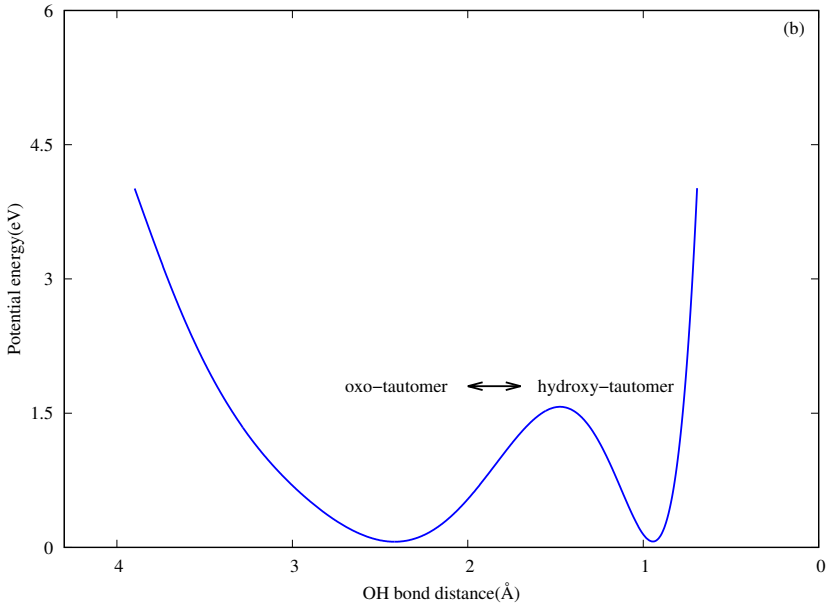

Figure 3.2: The above plot represents the one dimensional potential energy function of the ground electronic state along the OH bond distance.

Table 3.1: *Ab initio* PES data in eV are fitted against the reaction coordinate, r in Å using Eq. (3.1). Numerical values of parameters of the ground electronic potential are tabulated below.

a_0=-201.8	a_3=322.8	a_6=-0.7072
a_1=588	a_4=-87.76	b_1=48.06
a_2=-632.8	a_5=12.34	b_2=1.501

$$\mu(r) = a_0 + \sum_{n=1}^{5} a_n x^n exp(-b_n r^2), \tag{3.2}$$

using the regression method [see Figs. (3.2) and (3.3), and Tables (3.1) and (3.2)].

The potential profile is an asymmetric double well in nature. There is a potential barrier of 180 kJ/mol for the conversion of oxo tautomer to hydroxy tautomer. Therefore, the vibrational excitations are important for the tautomerization in the ground electronic state.

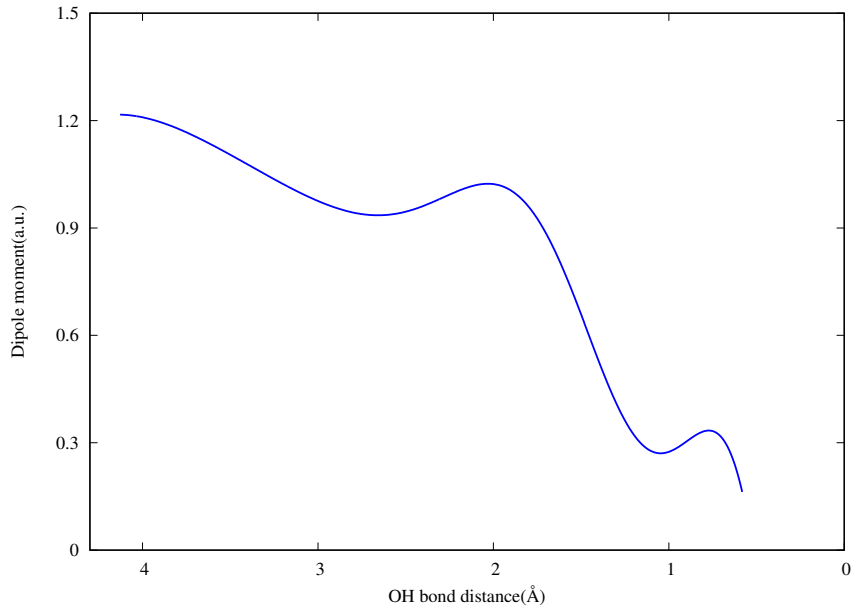

Figure 3.3: The above plot represents the one dimensional DM along the OH bond distance.

Table 3.2: *Ab initio* dipole moment data in a.u. are fitted using Eq. (3.2) where the reaction coordinate, r is considered in Å. Numerical values of parameters of dipole data are tabulated below.

a_0=-4.189	a_4=-0.5932	b_3=0.1139
a_1=11.12	a_5=1.932	b_4=0.1547
a_2=0.1296	b_1=1.455	b_5=0.9677
a_3=1.757	b_2=0.5544	

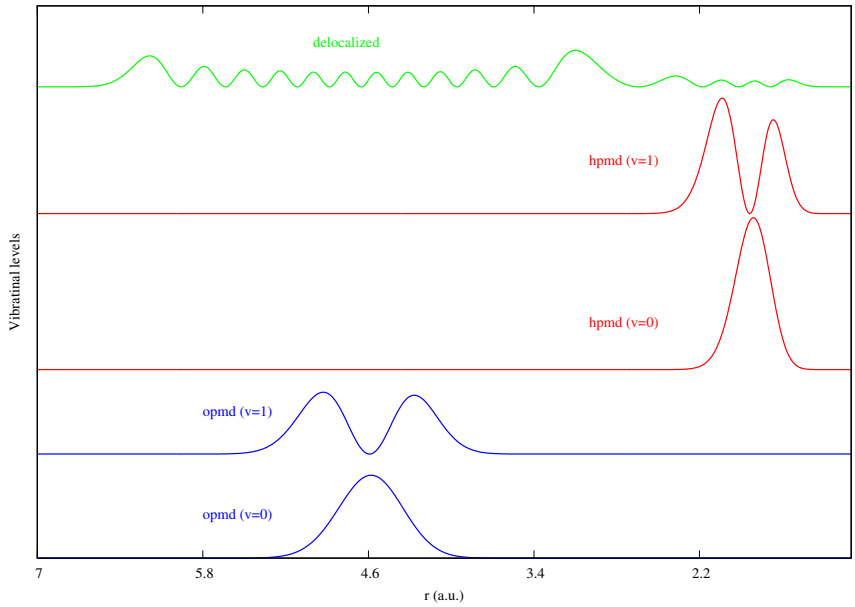

Figure 3.4: Above plots represent eigenstates of the ground electronic state calculated by the pseudo-spectral method.

3.2.2 Nuclear dynamics

The Hamiltonian of the model system in the field-free condition, $\hat{H}_0$ reads as

$$\hat{H}_0 = -\frac{1}{2\mu}\frac{\partial^2}{\partial r^2} + \hat{V}(r), \tag{3.3}$$

where $\mu = \frac{M_H M_O}{M_O + M_H}$ in which the M_H and M_O denote the masses of Hydrogen and Oxygen, respectively and $\hat{V}(r)$ is the PES. The vibrational eigenstates and eigenvalues of the ground electronic state are estimated using the pseudo-spectral method [178, 179]. The autocorrelation function is determined using the time-evolved wave function. The eigenvalues [see Table (3.3)] of the ground electronic state are obtained from the frequency spectrum. The vibrational eigenstates are estimated by evaluating the projection of the time-evolved wave function onto the associated eigenvalue [see Fig. (3.4)]. The eigenstates are localized as well as delocalized in nature [see Fig. (3.4)].

A laser field interacts with the molecule and results the modification of

the molecular Hamiltonian. The Hamiltonian of the model system , $\hat{H}$ in the semiclassical dipole approximation [87, 154] is given by,

$$\hat{H} = \hat{H}_0 + \hat{H}_{int}, \tag{3.4}$$

where $\hat{H}_0$ is the Hamiltonian in the absence of an external field and $\hat{H}_{int}$ is the laser-molecule interaction Hamiltonian reads

$$\hat{H}_{int} = -\hat{\mu} \cdot \epsilon(t), \tag{3.5}$$

where $\epsilon(t)$ is the field and $\hat{\mu}$ is the DM.

The nuclear wave function, $|\Psi(t)\rangle$ follows the TDSE,

$$i\hbar \frac{\partial}{\partial t}|\Psi(t)\rangle = \hat{H}|\Psi(t)\rangle. \tag{3.6}$$

The above equation is solved numerically by employing the split-operator method (SO) [171, 200] and fast Fourier transformation (FFT) [172] methods. The one dimensional grid along the OH bond distance contains 512 grid points ranging from 1.0 a_0 to 6.8 a_0.

3.2.3 Optimal control theory

The cost functional is constructed in the theoretical framework of OCT [81, 156, 157]. The cost functional, $J[\epsilon(t)]$ reads as

$$J[\epsilon(t)] = |\langle\psi(T)|\phi_f(T)\rangle|^2 - \alpha_o \int_0^T [\epsilon(t)]^2 dt - 2Re\left[\langle\psi(T)|\phi_f(T)\rangle \int_0^T \langle\chi(t)\left|\frac{\partial}{\partial t} + i\hat{H}\right|\psi(t)\rangle dt\right]. \tag{3.7}$$

In the above equation, the first term on the right hand side is the transition probability (P) that measures the overlap between the initial state at t=T and target state. This term is considered as the objective. The second term is the fluence term as a constraint and it is associated with the laser field. α_0 is the penalty factor that limits the laser pulse intensity. The last term corresponds

to the dynamics of the system which follows the TDSE. $\chi(t)$ is the Lagrange multiplier. The variation of the cost functional with respect to $\epsilon(t)$, $\psi(t)$ and $\chi(t)$ leads the pulse design equations,

$$\begin{aligned}
\frac{\partial J}{\partial \chi} &= 0 \Rightarrow i\frac{\partial \psi(t)}{\partial t} = \hat{H}\psi(t), \psi(0) = \phi_i, && (3.8)\\
\frac{\partial J}{\partial \psi} &= 0 \Rightarrow i\frac{\partial \chi(t)}{\partial t} = \hat{H}\chi(t), \chi(T) = \hat{O}\psi(t), && (3.9)\\
\frac{\partial J}{\partial \epsilon} &= 0 \Rightarrow \epsilon(t) = -\frac{1}{\alpha_0} Im(\langle\psi(T)|\phi_f(T)\rangle\langle\chi(t)|\mu|\psi(t)\rangle). && (3.10)
\end{aligned}$$

Equation (3.8) determines the time-dependent initial state, $\psi(t)$. Similarly, Eq. (3.9) estimates the time-dependent Lagrange multiplier, $\chi(t)$. The optimal laser pulse is determined by using $\psi(t)$ and $\chi(t)$ [Eq. (3.10)]. The above differential equations are coupled to each other. Therefore, they should be solved iteratively. Here, these equations are solved by using the conjugate gradient method.

3.3 Conjugate gradient method

In the conjugate gradient method [89, 90, 162], the laser pulse, $\epsilon(t)$ reads as

$$\epsilon(t) = E_0 \sin(\omega_{\text{init}} t).\text{s}(t), \tag{3.11}$$

where E_0 and ω_{init} are the amplitude and frequency, respectively. The pulse is composed of a sinusoidal electric field with an envelope function. The envelope function, $s(t)$ guarantees a steady power on/off of the field and it is a Gaussian function [162],

$$\text{s}(t) = exp\frac{-(t - T/2)^2}{(T/4)^2}, \tag{3.12}$$

where T is the total time duration. The gradient of the cost functional with respect to the initial laser pulse, $\epsilon_0(t)$ after k^{th} number of iterations is expressed as

$$\begin{aligned}
g^k(t) &= \frac{\partial J^k}{\partial \epsilon_0^k(t)},\\
&= -2s(t)[\alpha_0\epsilon^k(t) + Im\langle\chi(t)|\psi(t)\rangle\langle\psi(T)|\phi_f(T)\rangle]. && (3.13)
\end{aligned}$$

In the conjugate gradient algorithm, the parameter space for the laser pulse is searched using the Polak–Ribiere–Polyak search direction [164] to maximize the cost functional. The search direction, d after k^{th} number of iterations is expressed as

$$d^k(t_i) = g^k(t_i) + \lambda^k . d^{k-1}(t_i). \tag{3.14}$$

In the above equation, λ is the conjugate gradient parameter and given by

$$\lambda^k = \frac{\sum_i g^k(t_i)^T (g^k(t_i) - g^{k-1}(t_i))}{\sum_i g^{k-1}(t_i)^T g^{k-1}(t_i)}, \tag{3.15}$$

where, k=2,3,..., and T denotes the transpose. In the line search process, the search direction is projected [165] to prevent the large value of the $\epsilon(t_i)$ from the predefined range.

A laser pulse of a simple frequency profile (within the specified range of frequency) [166], is obtained by filtering the frequency function with a 20^{th}-order Butterworth band pass filter [167]. The filter is given as

$$h(\omega) = \left[\left(1 + \left(\frac{\omega_{min}}{\omega} \right)^{40} \right) \left(1 + \left(\frac{\omega}{\omega_{max}} \right)^{40} \right) \right]^{-\frac{1}{2}}. \tag{3.16}$$

The frequency function of the projected search direction is calculated from the Fourier transformation with the expression given below,

$$d^k_{p,filter}(t) = \int h(\omega) F_\omega [d^k_p(t)] e^{-i\omega t} d\omega. \tag{3.17}$$

In the optimization process, the updated electric field, $\epsilon^{k+1}(t_i)$ reads as,

$$\epsilon^{k+1}(t_i) = \epsilon^k(t_i) + \lambda s(t_i) d^k_{p,filter}(t). \tag{3.18}$$

3.4 Results and discussion

3.5 opmd (v=0)→opmd (v=1) transition

It can be seen from Figs. (3.5) and (3.6) that the optimal laser pulses transfer the population from the initial state i.e., the opmd (v=0) vibrational state to the

Table 3.3: Vibrational eigenvalues of the ground electronic state are tabulated below.

	Vibrational states	E (cm^{-1})
1	opmd (n=0)	1109
2	opmd (n=1)	2280
3	hpmd (n=0)	2581
4	opmd (n=2)	3430
5	opmd (n=3)	4560
6	opmd (n=4)	5664

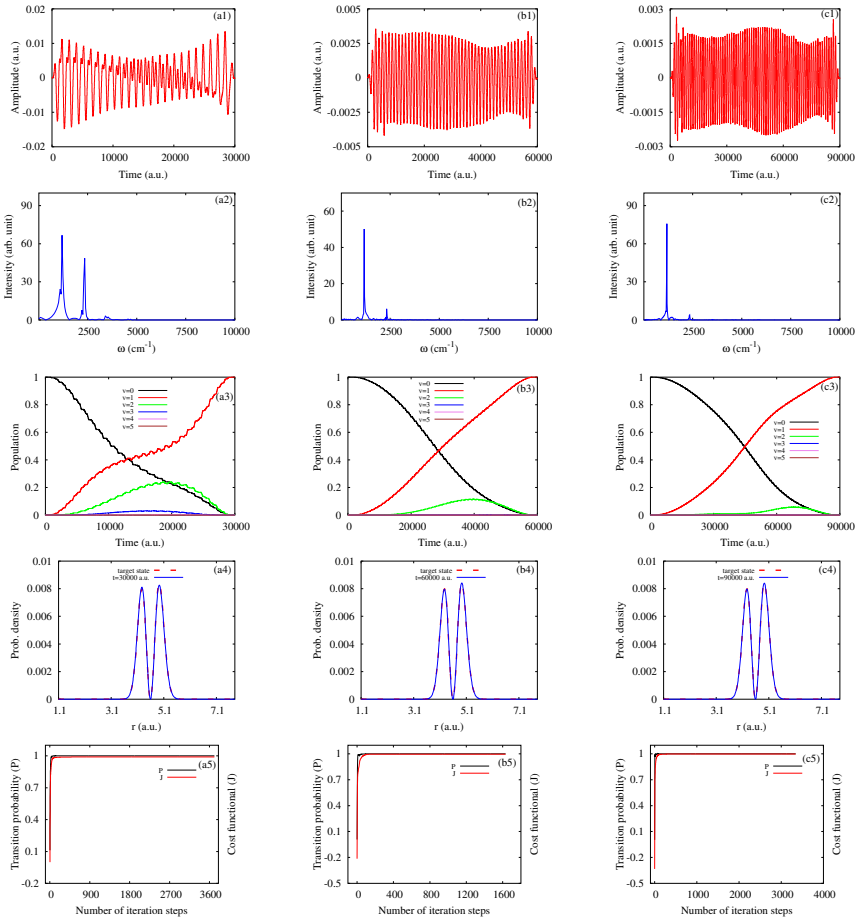

Figure 3.5: Optimal laser pulses in the time domain (a1, b1 and c1), frequency spectra (a2, b2 and c2) and populations of various vibrational states (a3, b3 and c3) are depicted above. Plots (a4, b4 and c4) present probability densities of $\psi(T)$ and the target vibrational state. Plots (a5, b5 and c5) show variations of J and P with iteration steps. These results are obtained for the v=0→v=1 transition for the timescales of 30000, 60000 and 90000 a.u. with α_0 value 0.01.

target state i.e., the opmd (v=1) vibrational state for the timescales of 30000, 60000 and 90000 a.u.. These optimal calculations are carried out for different values of α_0 i.e., 0.01 and 0.1. It can be seen from Figs. 3.5(a1), 3.5(b1), 3.5(c1), 3.6(a1), 3.6(b1) and 3.6(c1) that the optimal laser pulses have smooth temporal profiles. Amplitudes of the obtained laser fields for this transition decrease for increasing the time duration. This phenomena agrees with the pulse-area theorem [128, 129] . Apart from the carrier frequency peak, several secondary frequency peaks appear in the frequency spectra. The population of the initial state (opmd (n=0)) is transferred almost completely to the target state (opmd (v=1)) in the presence of the optimal laser pulses [see Figs. 3.5(a3), 3.5(b3), 3.5(c3), 3.6(a3), 3.6(b3) and 3.6(c3)]. Besides the opmd (v=0) and opmd (v=1) states, various intermediate states e.g., opmd (v=2), opmd (v=3), opmd (v=4) and opmd (v=5) participate in the population transfer process. It can be seen from Figs. 3.5(a3), 3.5(b3), 3.5(c3), 3.6(a3), 3.6(b3) and 3.6(c3)] that the opmd (v=2) vibrational state is engaged dominantly in the transition as compared to other intermediate states. The population of the opmd (v=0) vibrational state is excited to the opmd (v=1) state and intermediate states rapidly for the three mentioned time durations. Populations of the intermediate states (especially opmd (v=2)) is transferred to the opmd (v=1) vibrational state. The populations of the intermediate states reach the maxima [see Figs. 3.5(a3), 3.5(b3), 3.5(c3), 3.6(a3), 3.6(b3) and 3.6(c3)] in the population transfer process. The opmd (v=2) and opmd (v=3) vibrational states are involved in the transition for the pulse duration of 30000 a.u.. On the other hand, the opmd (v=2) state participates for the time durations of 60000 and 90000 a.u.. The opmd (v=2) gets a higher population for the pulse of time duration 30000 a.u. as compared to 60000 and 90000 a.u.. With increasing the pulse duration, the population transfer happens more efficiently because of the participation of a lower number of intermediate states. However, for all conditions, almost 100% population of the initial state

is transferred to the target state at the end of pulse durations. It is clear from Figs. 3.5(a4), 3.5(b4), 3.5(c4), 3.6(a4), 3.6(b4) and 3.6(c4) that the probability density of $\psi(T)$ overlaps perfectly with the probability density of the target state. The cost functional increases rapidly towards the convergence value within a few initial iterations. Finally, it is converged within 5000 iterations. The conjugate gradient method works well to optimize the laser pulse for the transition.

3.6 opmd (v=0)→opmd (v=2) transition

Here, the opmd (v=0) and opmd (v=2) vibrational states are considered as the initial and target states, respectively. The optimal laser pulses are designed for the timescales of 30000, 60000 and 90000 a.u. with α_0 values of 0.01 and 0.1. It is clear from Figs. (3.7) and (3.8) that the population of the initial state (opmd (v=0)) is excited to the target state (opmd (v=2)) as well as intermediate states i.e., opmd (v=1), opmd (v=3), opmd (v=4) and opmd (v=5) states in the presence of the optimal laser pulse. The population of the initial state is depleted rapidly during the early period of time durations. The intermediate states gain the population from the initial state and the population of them is shifted to the target state. Hence, the intermediate states reach the maxima. The intermediate vibrational states i.e., opmd (v=1), opmd (v=3) and opmd (v=4) states involve for the time duration of 30000 a.u. whereas opmd (v=1) and opmd (v=2) states take part in the transition for timescales of 60000 and 90000 a.u.. For time durations of 60000 and 90000 a.u., the opmd (v=1) state gets a higher population as compared to the time duration of 30000 a.u. for both values of α_0 i.e., 0.01 and 0.1. Because of the involvement of the intermediate vibrational states, frequency spectra show more than one peak. It is clear from Figs. 3.7(a4), 3.7(b4), 3.7(c4), 3.8(a4), 3.8(b4) and 3.8(c4) that probability densities of $\psi(T)$ have good agreement with the probability density of the target state. Therefore, almost 100% population of the initial vibrational state is excited to the target

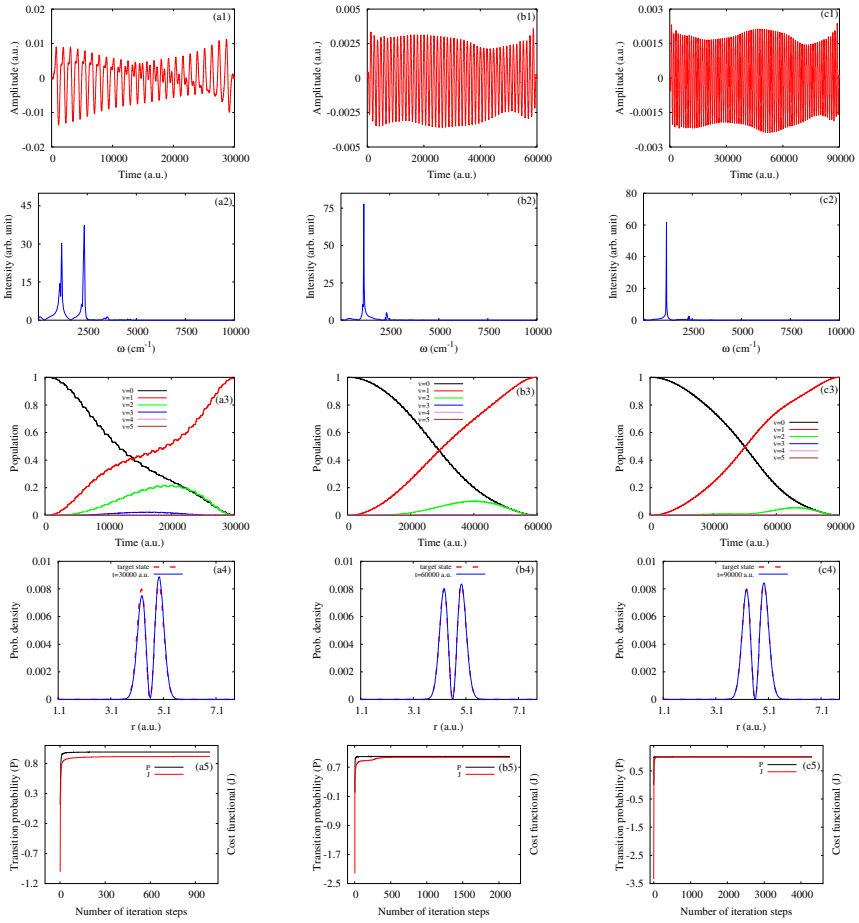

Figure 3.6: Optimal laser pulses in the time domain (a1, b1 and c1), frequency spectra (a2, b2 and c2) and populations of various vibrational states (a3, b3 and c3) are depicted above. Plots (a4, b4 and c4) present probability densities of $\psi(T)$ and the target vibrational state. Plots (a5, b5 and c5) show variations of J and P with iteration steps. These results are obtained for the v=0→v=1 transition for the timescales of 30000, 60000 and 90000 a.u. with α_0 value 0.1.

vibrational state. The cost functional shows good convergence behaviour for the vibrational transition in the conjugate gradient optimization method. In this case, the cost functional is converged within 3000 iterations [see Figs. 3.7(a5), 3.7(b5), 3.7(c5), 3.8(a5), 3.8(b5) and 3.8(c5)].

3.7 opmd (v=3)→opmd (v=4) transition

For this transition, the opmd (v=3) and opmd (v=4) vibrational states are considered as the initial and target states, respectively. It is clear from Figs. (3.9) and (3.10) that the optimal laser pulses for the timescales of 30000, 60000 and 90000 a.u. are designed for the transition. The optimizations are carried out for two different values of α_0 i.e., 0.01 and 0.1. Intermediate vibrational states i.e., opmd (v=0), opmd (v=1), opmd (v=2), opmd (v=5), opmd (v=6) and opmd (v=7) states take part in the field-driven transition for the time duration of 30000 a.u.. On the other hand, opmd (v=2) and opmd (v=1) states are involved for time durations of 60000 and 90000 a.u.. The initial state is excited to the target and intermediate states. The target vibrational state gets its population from the initial vibrational state as well as from intermediate states. It is clear from Figs. 3.9(a3), 3.9(b3), 3.9(c3), 3.10(a3), 3.10(b3) and 3.10(c3) that populations of intermediate states show maxima as their populations increase at initial pulse durations and after that, these populations are transferred to the target state. There are several peaks appear in the frequency spectra of these pulses because of multiple transitions. It is clear from Figs. 3.9(a3), 3.9(b3), 3.9(c3), 3.10(a3), 3.10(b3) and 3.10(c3) that the population of the initial state is transferred efficiently to the target state for timescales of 60000 and 90000 a.u. as compared to 30000 a.u.. The probability density of $\psi(T)$ overlaps with the probability density of the target state [see Figs. 3.9(a4), 3.9(b4), 3.9(c4), 3.10(a4), 3.10(b4) and 3.10(c4)]. It can be seen from Figs. 3.9(a3), 3.9(b3), 3.9(c3), 3.10(a3), 3.10(b3) and 3.10(c3) that at t=T almost 100% population is excited to

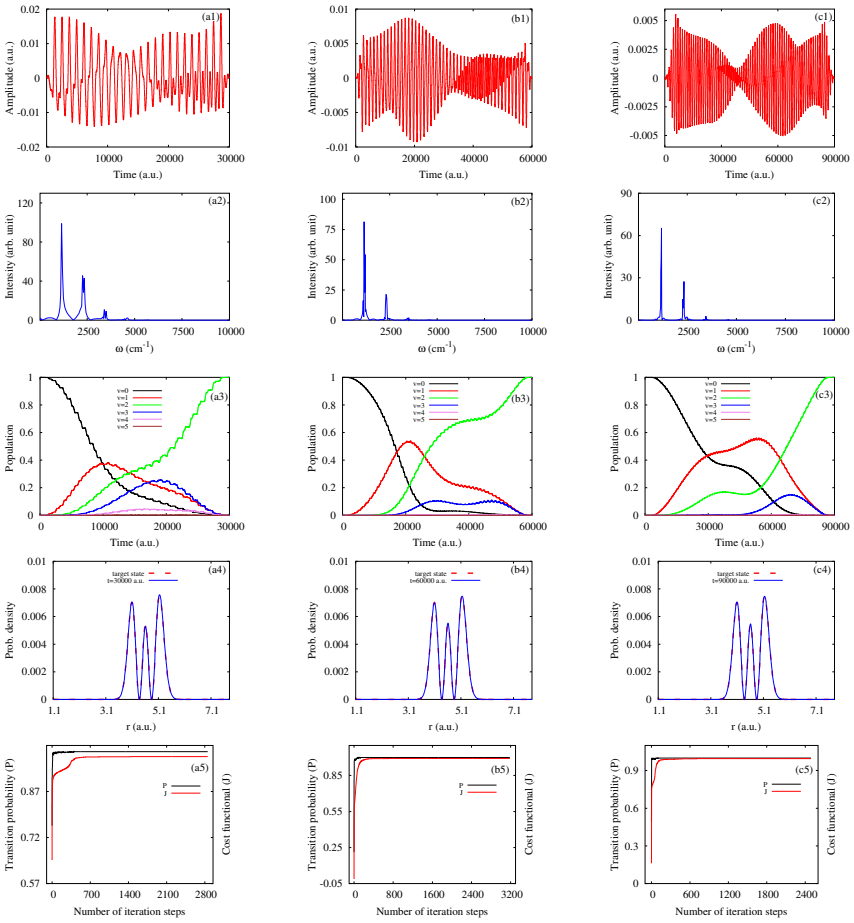

Figure 3.7: Optimal laser pulses in the time domain (a1, b1 and c1), frequency spectra (a2, b2 and c2) and populations of various vibrational states (a3, b3 and c3) are depicted above. Plots (a4, b4 and c4) present probability densities of $\psi(T)$ and the target vibrational state. Plots (a5, b5 and c5) show variations of J and P with iteration steps. These results are obtained for the v=0→v=2 transition for the timescales of 30000, 60000 and 90000 a.u. with α_0 value 0.01.

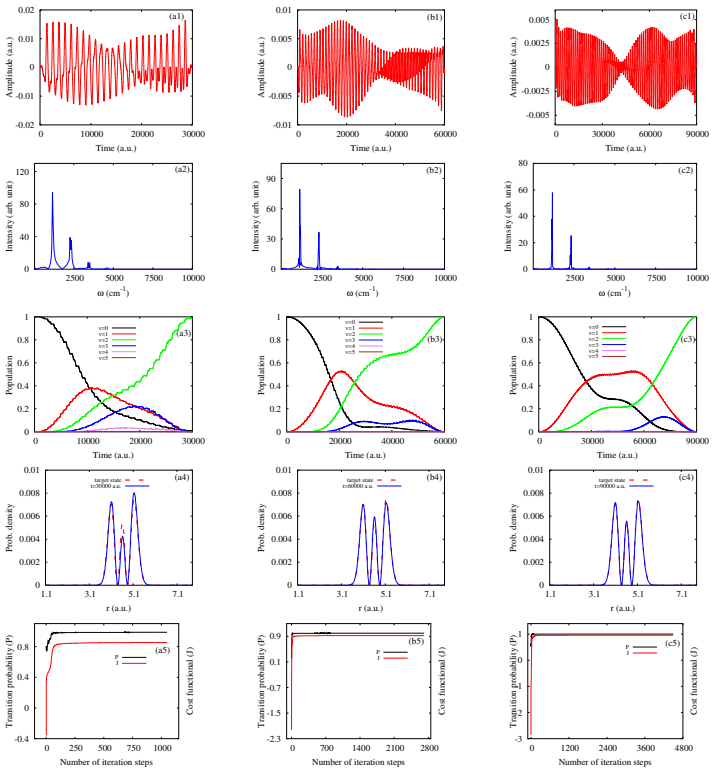

Figure 3.8: Optimal laser pulses in the time domain (a1, b1 and c1), frequency spectra (a2, b2 and c2) and populations of various vibrational states (a3, b3 and c3) are depicted above. Plots (a4, b4 and c4) present probability densities of $\psi(T)$ and the target vibrational state. Plots (a5, b5 and c5) show variations of J and P with iteration steps. These results are obtained for the v=0→v=2 transition for the timescales of 30000, 60000 and 90000 a.u. with α_0 value 0.1.

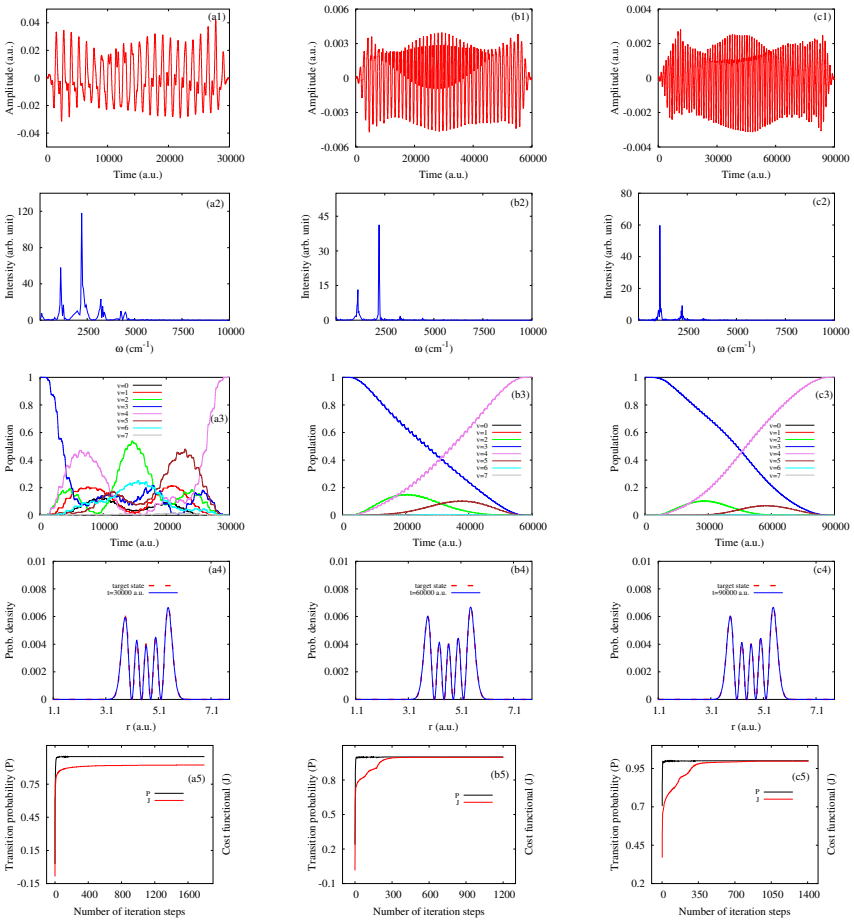

Figure 3.9: Optimal laser pulses in the time domain (a1, b1 and c1), frequency spectra (a2, b2 and c2) and populations of various vibrational states (a3, b3 and c3) are depicted above. Plots (a4, b4 and c4) present probability densities of $\psi(T)$ and the target vibrational state. Plots (a5, b5 and c5) show variations of J and P with iteration steps. These results are obtained for the v=3→v=4 transition for the timescales of 30000, 60000 and 90000 a.u. with α_0 value 0.01.

the target vibrational state. The cost functional reaches to the convergence limit within 2000 iterations [see Figs. 3.9(a5), 3.9(b5), 3.9(c5), 3.10(a5), 3.10(b5) and 3.10(c5)].

3.8 Effect of penalty factor (α_0)

We performed the optimal calculations with different values of α_0 i.e., 0.01 and 0.1. The calculations for different α_0 values are carried out for three different time domains of 30000, 60000 and 90000 a.u.. Other conditions in these optimization processes are kept fixed for a particular transition in a specific time duration. It is clearly seen from Eq. (3.7) that the penalty factor, α_0 controls the laser pulse energy to optimize the objective. It is clear from Table (3.4) that laser field amplitude decreases with the rise of α_0 from 0.01 to 0.1. Similarly, the cost functional and transition probability decrease with an increment of α_0 for a specific time domain of a particular transition. Hence, the penalty factor, α_0 has a crucial effect on the laser field-induced transition.

3.9 opmd (v=0)→hpmd (v=0) transition

In this case, the opmd (v=0) and hpmd (v=0) vibrational states are the initial and target states, respectively. The considered vibrational transition results the laser field-induced tautomerization. The frequency of the initial pulse is guessed by considering one of a delocalized vibrational state as an intermediate state for the transition. The optimal laser pulse has a complex temporal profile with multiple peaks in the frequency spectrum [see Fig. (3.11)]. It is clear from Fig. 3.11(a1) that the temporal profile of the control pulse clearly has pumping and dumping components. The pumping field components excite the initial state to various intermediate states and the dumping components de-excite their populations to the target state. It can be seen from Figs. 3.11(a2), (3.12) and (3.13) that multiple intermediate states including localized vibrational

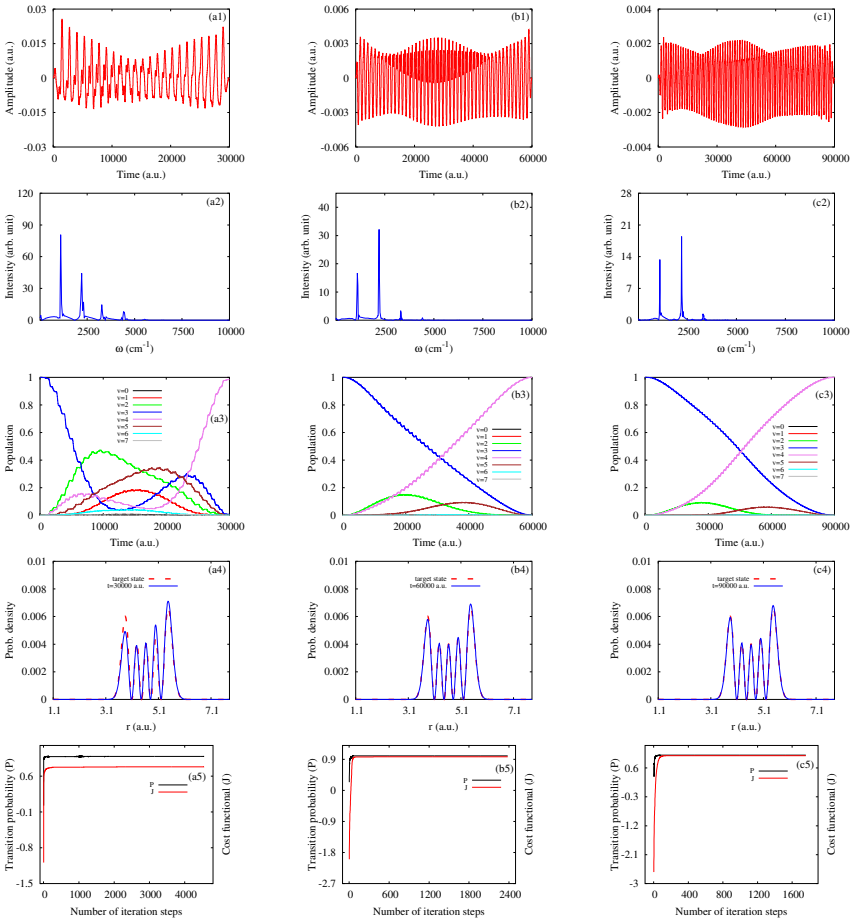

Figure 3.10: Optimal laser pulses in the time domain (a1, b1 and c1), frequency spectra (a2, b2 and c2) and populations of various vibrational states (a3, b3 and c3) are depicted above. Plots (a4, b4 and c4) present probability densities of $\psi(T)$ and the target vibrational state. Plots (a5, b5 and c5) show variations of J and P with iteration steps. These results are obtained for the v=3→v=4 transition for the timescales of 30000, 60000 and 90000 a.u. with α_0 value 0.1.

Table 3.4: Results are shown below in the table calculated for opmd (v=0)→opmd (v=1), opmd (v=0)→opmd (v=2) and opmd (v=3)→opmd (v=4) transitions for the timescales of 30000, 60000 and 90000 a.u. with various values of the penalty factor, α_0 i.e., 0.01 and 0.1. J and P denote the cost functional and transition probability, respectively. ϵ_{peak} refers to the amplitude (max). These parameters are presented in a.u..

Transition	α_0	T	P	J	ϵ_{peak}
v=0⟶v=1	0.01	30000	0.999859	0.990677	1.4817×10^{-2}
		60000	0.999993	0.997234	4.1743×10^{-3}
		90000	0.999995	0.998251	2.7296×10^{-3}
	0.1	30000	0.991604	0.916241	1.3599×10^{-2}
		60000	0.999662	0.973698	3.5858×10^{-3}
		90000	0.999872	0.983131	2.3955×10^{-3}
v=0⟶v=2	0.01	30000	0.999806	0.983936	1.8754×10^{-2}
		60000	0.999974	0.992038	9.2717×10^{-3}
		90000	0.999993	0.995359	5.5540×10^{-3}
	0.1	30000	0.986256	0.853485	1.6404×10^{-2}
		60000	0.997816	0.924510	8.6830×10^{-3}
		90000	0.999540	0.957303	5.0095×10^{-3}
v=3⟶v=4	0.01	30000	0.999564	0.922876	4.1834×10^{-2}
		60000	0.999970	0.996849	4.6880×10^{-3}
		90000	0.999976	0.998074	3.1322×10^{-3}
	0.1	30000	0.985897	0.786432	2.5583×10^{-2}
		60000	0.999507	0.971387	4.2228×10^{-3}
		90000	0.999839	0.982534	2.8602×10^{-3}

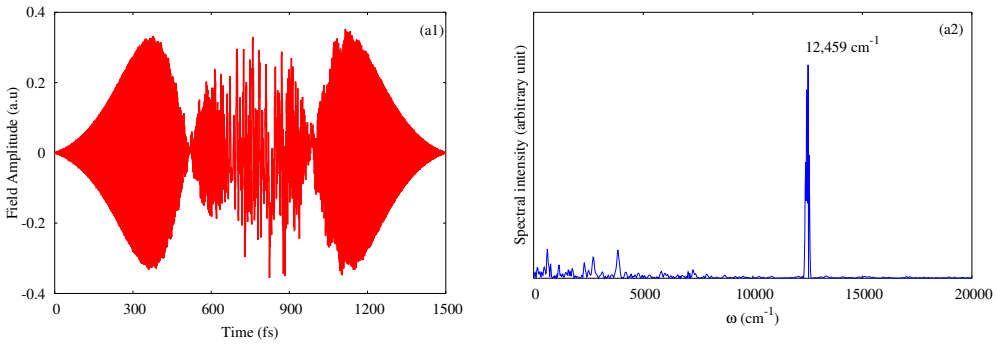

Figure 3.11: The Temporal profile (a1) and frequency spectrum of the optimal laser pulse for the opmd (v=0) to hpmd (v=0) transition.

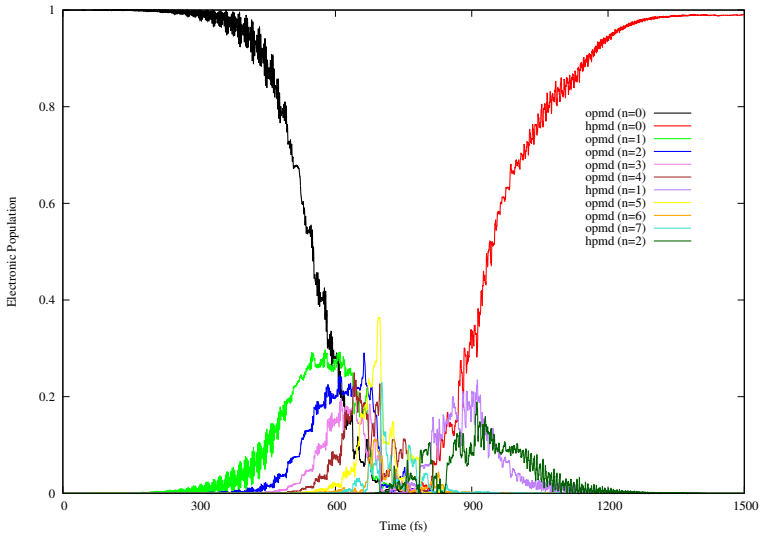

Figure 3.12: Localized state populations in the optimal condition. These vibrational states (except the initial and target states) act as intermediate states.

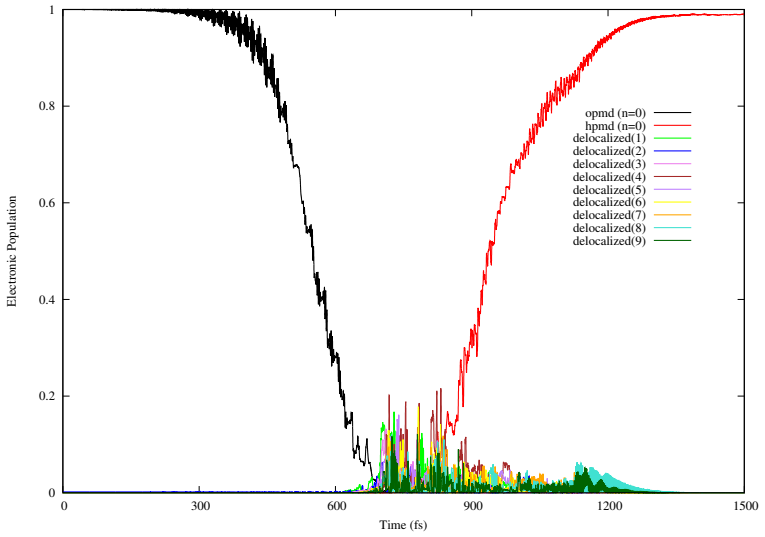

Figure 3.13: Time-dependent populations of various delocalized vibrational states, 4(3H)-pyridinone (v=0) vibrational state and 4 hydroxypyrimidine (v=0) vibrational state in the optimal condition. These delocalized vibrational states act as intermediate states.

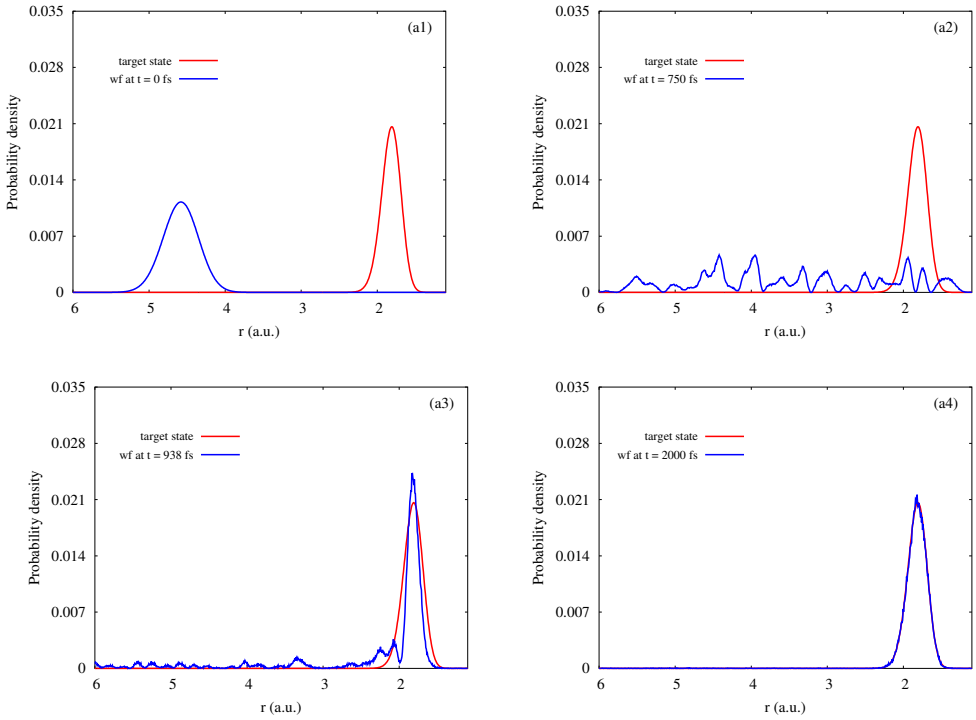

Figure 3.14: Plots (a1, a2, a3 and a4) represent the probability density of target state (red) and snapshots of the probability densities of the field-driven time-evolved wave function (blue) at 0 fs, 750 fs, 938 fs and 2000 fs.

states as well as delocalized states are involved in the transition. Among these intermediate states, a delocalized state corresponds to the frequency 12459 cm^{-1} (carrier frequency) participates predominantly in the transition. The control pulse excites rapidly the initial state population to various intermediate states. After 850 fs (approximately), the target vibrational state gets the population very rapidly from the intermediates. Finally, at the end of the time period, t=T about 95% population is excited to the target state. It can be seen in Figs. (3.15) and (3.16) that the cost functional is maximized as well as the objective i.e., the transition probability is optimized in the optimization process. The cost functional is converged efficiently within 950 iterations.

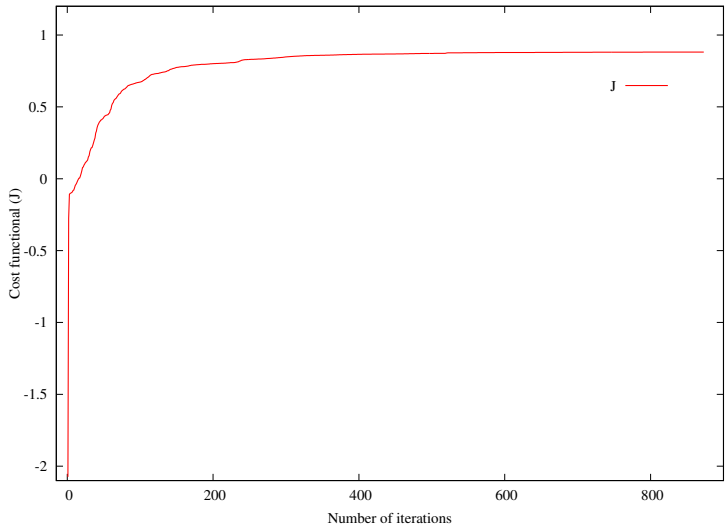

Figure 3.15: Cost functional (J) at various iterative steps.

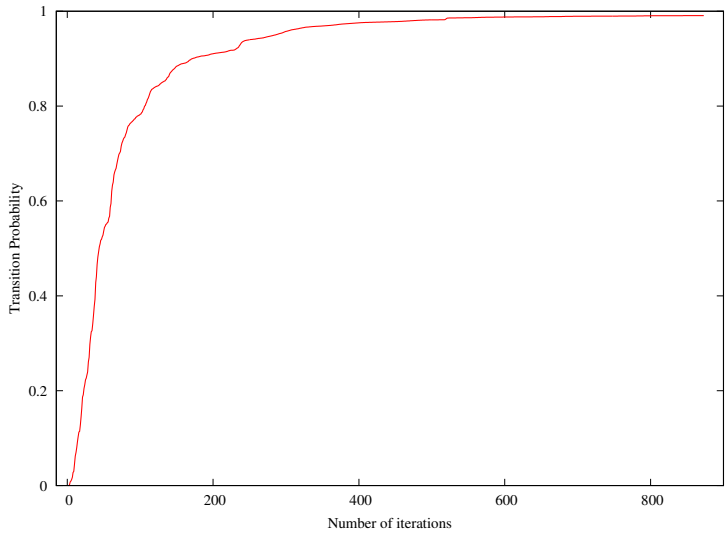

Figure 3.16: Transition probability (P) at various iterative steps.

3.10 Conclusions

In the present study, various vibrational transitions are controlled with the optimal laser pulses. These optimal laser pulses are constructed in OCT using the conjugate gradient method. The model system consists of the one dimensional ground electronic state of the 4(3H)-pyrimidinone/4-hydroxypyrimidine system. The potential energy profile for the ground electronic state is calculated from the CCSD method using an aug-cc-pVDZ basis set and the DM is calculated from the CASSCF method employing the Molpro package. The ground electronic state has a potential barrier of 180 kJ/mol and the barrier separates the tautomers. The optimal pulses are constructed in different time durations of 30000, 60000 and 90000 a.u. with various values of the penalty factor, α_0 i.e., 0.1 and 0.01. In the presence of the optimal laser pulse, the initial state population is transferred efficiently to the target state. We observed that field amplitudes of the optimal laser pulses decrease with higher time durations with the agreement of the pulse area theorem [128, 129]. Besides the sharp peak which is responsible for the considered transition, there are secondary peaks appear in frequency spectra because of the involvement of intermediate vibrational states. A lower number of secondary peaks in frequency spectra appear for a higher time duration. For higher time durations, a lower number of intermediate states are involved and the population transfer becomes more efficient for a particular transition . However, at the end of the time period, t=T almost 100% population is excited to the target vibrational state. Increasing the penalty factor results a reduction in the amplitude of the optimal laser field. In a similar way, the transition probability and cost functional decrease with a higher value of the penalty factor. Also, the vibrational excitation is controlled from the opmd (v=0) state to the hpmd (v=0) state. A strong field laser pulse is obtained from the conjugate gradient optimization. In this case, the optimal laser pulse excites the initial vibrational state to many intermediate states and also de-excites to various intermediate

states. The frequency spectrum of the control pulse indicates that a delocalized state participates predominantly in this transition.

In the present study, the conjugate gradient method is found to be effective to maximize the cost functional of a transition. The cost functional reaches near the convergence limit within a few iterations. The conjugate gradient method works well to design the optimal laser pulses for the various vibrational transitions.

Chapter 4

Optimal control of excited electronic state mediated tautomerization of 4(3H)-pyrimidinone

4.1 Introduction

4(3H)-pyrimidinone is a photo-physically active molecule and it is a simpler molecule than pyrimidine nucleobases (cytosine, thymine and uracil). It is important to understand its chemical properties from various experimental and theoretical studies [180, 181].

The tautomerization reaction involving proton transfer is an important phenomenon in biological systems especially in the structure of nucleic acids. 4(3H)-pyrimidinone is a good model compound for the prototropic tautomerism of heterocyclic compounds. In the tautomeric equilibrium [182, 183], 4(3H)-pyrimidinone (oxo tautomer) is converted to 4-hydroxypyrimidine (hydroxy tautomer) through the intramolecular hydrogen transfer reaction. The molecule co-exist in the tautomeric (∼1:1) equilibrium [182–186] with the hydroxy tautomer in the gas phase and inert gas (Ar and Ne) matrices. The

tautomeric equilibrium of 4(3H)-pyrimidinone has been studied experimentally in IR spectroscopy [182, 183], NMR spectroscopy [184], X-ray photoemission spectroscopy [186], free jet millimeter wave spectroscopy [185], etc. IR spectra of 4(3H)-pyrimidinone and 4-hydroxypyrimidine have been determined using various *ab initio* calculations [187]. Galvão *et al.* [189] investigated theoretically (using *Ab initio* calculations) the stability of 4(3H)-pyrimidinone in the equilibrium as compared to 2-pyridinone. Leś *et al.* [188] explained theoretically the temperature-dependent population of the tautomers in the gas phase. Upon exposure to the UV light ($<$ 310 nm), 4(3H)-pyrimidinone is converted to 4-hydroxypyrimidine [190–194]. In this condition, the intramolecular hydrogen transfer reaction occurs between the tautomers. In general, the excited state proton transfer (ESPT) reaction occurs through an intermolecular or intramolecular hydrogen bond. In this molecular process, the intramolecular hydrogen transfer reaction takes place without having an intramolecular or intermolecular hydrogen bond. The photo-induced tautomeric conversion of 4(3H)-pyrimidinone was theoretically [191, 193, 195, 196] studied using various methods of quantum chemistry. *Ab initio* studies combined with IR spectroscopy to separate tautomeric forms based on the phototautomeric effect. Theoretical studies were reported to explain the mechanism of the reaction as well as stability of the tautomers. Nowak *et al.* [196] reported that various electronic states (the ground, $\pi\pi^*$, $n\pi^*$ and $\pi\sigma^*$ states) are associated with the photo-induced oxo-hydroxy tautomerization. These states are nonadiabatically coupled in the photo-induced tautomerization reaction.

Control of an outcome of a quantum mechanical system by a laser field has been developed within the mathematical framework of optimal control theory (OCT) [81, 155–157, 197, 198]. Gradient-based algorithms and the genetic algorithm are used to optimize a desired outcome of a reaction by constructing a

suitable laser pulse. The optimally designed laser pulse drives a system to follow a specific path that optimizes a desired outcome. The genetic algorithm [107] has been extensively used in different scenarios of control problems, such as control of laser-driven photodissociation of pyrrole and phenol molecules [201–203], optimal control of laser-induced isomerization of malonaldehyde [204], optimal control of laser-induced molecular orientation, control of vibrational–rotational excitations [169] and molecular quantum gate operations [205, 206].

In this work, the model system consists of the ground state and $\pi\pi^*$ state. The oxo and hydroxy tautomers are represented as the reactant and product, respectively. The product population i.e., the hydroxy tautomer population is controlled in the presence of optimal laser pulses. The pump and dump ultrashort UV laser pulses are obtained employing the genetic algorithm. The product population is maximized by controlling the wave packet (WP) propagation. The tautomerization takes place through the pump-dump mechanism [41, 42] via the $\pi\pi^*$ state. Transition events (excitation and de-excitation) are treated separately from the propagation of the WP on the $\pi\pi^*$ state. The time separation between these two pulses is suitably chosen from the field-free WP evolution. The WP evolves freely on the excited state. The excitation and de-excitation processes are controlled using the UV laser pulses. Therefore, laser pulse properties e.g., phase, frequency and amplitude play an important role in those transitions. These laser pulse parameters are optimized using the genetic algorithm.

4.2 Theory

4.2.1 *Ab initio* calculations of the model system

The one dimensional model system is constructed to study the laser light-induced tautomerization using the pump-dump mechanism. The intramolecular hydrogen transfer reaction occurs in the tautomerization. The model system composes the two electronic states i.e., the ground electronic state and $\pi\pi^*$ state with

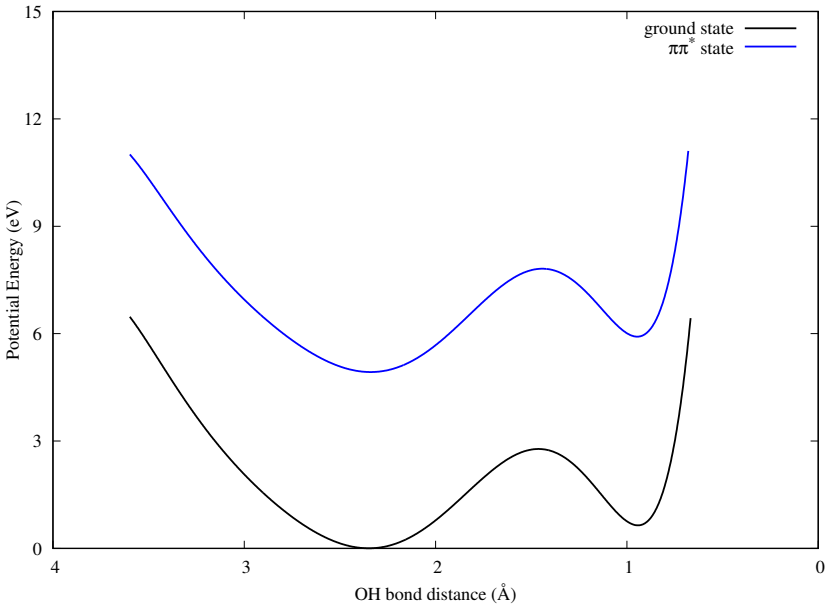

Figure 4.1: Above plots represent PE profiles of the ground electronic state (black) and $\pi\pi^*$ state (blue) of the model system.

varying the OH bond distance. The OH bond distance is treated as the reaction coordinate, r. The conversion of 4(3H)-pyrimidinone to 4-hydroxypyrimidine is studied in this model. Equilibrium geometries of both the tautomers are obtained with the second order M∅ller-Plesset perturbation (MP2) method using an aug-cc-pVDZ basis set employing the Gaussian package. Various molecular structures for calculations of single point energies are constructed by varying the OH distance using the optimized oxo tautomer as a reference geometry. The single point potential energies and transition dipole moment (TDM) values corresponding to these structures are calculated in the equation-of-motion coupled cluster singles and doubles (EOM-CCSD) method employing the Molpro package [199]. The x component of the TDM for the transition between these states is considered in optimal calculations. The calculated potential energies and TDM values are fitted with polynomial analytical functions,

$$V_{g/e}(r) = a_0 + \sum_{n=1}^{7} a_n r^n \tag{4.1}$$

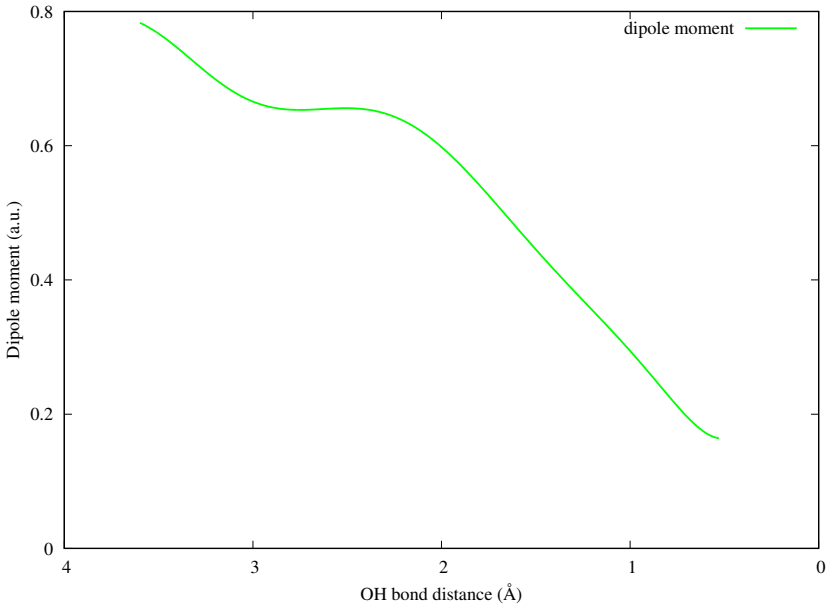

Figure 4.2: The above plot represents one dimensional TDM along the OH bond distance.

and

$$\mu_{eg}(r) = a_0 + \sum_{n=1}^{9} a_n r^n. \tag{4.2}$$

The fitted adiabatic potentials and TDM are depicted in Figs. (4.1) and (4.2). Both the adiabatic potentials are asymmetrical double wells. There are potential barriers of 2.8 and 7.8 eV (with reference to the energy of 4(3H)-pyrimidinone at the optimized geometry) of the ground electronic state and $\pi\pi^*$ state, respectively. Therefore, the potential barriers separate the tautomers on both the electronic states. Both the wells on potential energy (PE) functions represent the tautomers. Potential regions, i.e., $2.8 < \mathrm{r} < 6.8$ a.u. and $1.0 < \mathrm{r} < 2.8$ a.u. are defined as the oxo tautomer (reactant) and the hydroxy tautomer (product), respectively.

4.2.2 Nuclear dynamics in external field

The electric field of a laser field interacts with the molecule and modifies the molecular Hamiltonian. Within the semiclassical dipole approximation [87, 154],

Table 4.1: *Ab initio* PE data in eV are fitted using Eq. (4.1) where the reaction coordinate, r is in a.u.. Numerical values of parameters of V_g are tabulated below.

a_0=246.338	a_3=-170.184	a_6=0.424585
a_1=-495.515	a_4=41.0493	a_7=-0.0131989
a_2=401.797	a_5=-5.69567	

the laser field-induced molecular Hamiltonian of the model system ($\hat{H}$) reads

$$\hat{H} = \hat{H}_0 + \hat{H}_{int}, \tag{4.3}$$

where $\hat{H}_0$ is the molecular Hamiltonian under the field-free condition and expressed as

$$\hat{H}_0 = \hat{T}_N \begin{pmatrix} 1 & 0 \\ 0 & 1 \end{pmatrix} + \begin{pmatrix} \hat{V}_g & 0 \\ 0 & \hat{V}_e \end{pmatrix}, \tag{4.4}$$

where $\hat{V}_g$ and $\hat{V}_e$ are the PE functions. $\hat{T}_N$ is the kinetic energy operator reads as

$$\hat{T}_N = -\frac{1}{2\mu_{OH}} \frac{\partial^2}{\partial r^2}, \tag{4.5}$$

where $\mu_{OH} = \frac{m_O m_H}{m_O + m_H}$ in which m_O and m_H denote the masses of O and H, respectively. In Eq. (4.3), $\hat{H}_{int}$ is the laser-molecule interaction Hamiltonian,

$$\hat{H}_{int} = -\begin{pmatrix} 0 & \hat{\mu}_{eg} \\ \hat{\mu}_{eg} & 0 \end{pmatrix} .\epsilon(t), \tag{4.6}$$

where $\epsilon(t)$ is the electric field and $\hat{\mu}_{eg}$ is the TDM.

The wave function of the model system, $|\Psi(t)\rangle$ follows the time-dependent Schrödinger equation (TDSE),

$$i\hbar \frac{\partial}{\partial t} |\Psi(t)\rangle = \hat{H} |\Psi(t)\rangle. \tag{4.7}$$

The TDSE is solved numerically by employing the split-operator (SO) method [171, 200]. The fast Fourier transformation (FFT) algorithm [172] is used to solve the kinetic energy operation. The reaction coordinate, r ranges from 6.8 to 1.0 a_0 and consists of 1024 grid points. The total time duration for the

Table 4.2: *Ab initio* PE data in eV are fitted using Eq. (4.1) where the reaction coordinate, r is in a.u.. Numerical values of parameters of V_e are tabulated below

a_0=253.074	a_3=-173.081	a_6=0.437294
a_1=-499.792	a_4=41.939	a_7=-0.0136391
a_2=406.792	a_5=-5.84396	

WP evolution is 20 fs. The initial state is prepared by placing a Gaussian function in the reactant (oxo tautomer) region in the ground electronic state. The time-dependent electronic populations are determined by evaluating the expectation values of the projection operators, $|\psi_i\rangle\langle\psi_i|$, as

$$P_i(t) = \langle\Psi(t)|\psi_i\rangle\langle\psi_i|\Psi(t)\rangle, \qquad i = 1, 2. \tag{4.8}$$

The time-dependent population probabilities of the oxo tautomer ($Y_{react,i}(t)$) and hydroxy tautomer ($Y_{prod,i}(t)$) on both the electronic states are defined as

$$Y_{react,i}(t) = \int_{2.8}^{6.8} \psi_i^*(r;t)\psi_i(r;t).dr, \qquad i = 1, 2, \tag{4.9}$$

and

$$Y_{prod,i}(t) = \int_{1.0}^{2.8} \psi_i^*(r;t)\psi_i(r;t).dr, \qquad i = 1, 2, \tag{4.10}$$

respectively, where the lower and upper limits of the integrals are in atomic units.

4.2.3 Cost functional

The cost functional is constructed in the mathematical framework of OCT [81, 156, 157] to optimize a desired objective function. The cost functional is optimized in various problems using the genetic algorithm. In this study, the cost functional ($J[\epsilon(t)]$) reads

$$J[\epsilon(t)] = J_0 - \alpha_0 \int_0^T |\epsilon(t)|^2 dt, \tag{4.11}$$

where α_0 is the penalty factor and it restricts the laser pulse energy. In this study, α_0 sets to 0.001. J_0 is the objective function and it is expressed as

$$J_0 = Y_{prod,1}(T) + \frac{1}{T}\int_0^T Y_{prod,2}(t)dt + \frac{1}{T}\int_0^T Y_{react,2}(t)dt, \tag{4.12}$$

Table 4.3: *Ab initio* calculated TDM data in a.u. are fitted using Eq. (4.2) where the reaction coordinate, r is in Å. Numerical values of parameters of μ_{eg} are tabulated below.

a_0=1.18594	a_3=-11.6813	a_6=-0.726548	a_9=0.00380641
a_1=-5.74404	a_4=5.3992	a_7=0.327425	
a_2=11.9786	a_5=-0.39058	a_8=-0.0578271	

where $Y_{prod,1}(T)$ is the population of the hydroxy tautomer on the ground state at t=T. The second and third entities on the right hand side (RHS) of Eq. (4.12) are time-averaged population probabilities of the hydroxy tautomer and oxo tautomer on the $\pi\pi^*$ state, respectively. The population probabilities i.e., $Y_{prod,1}(T)$, $Y_{prod,2}(t)$ and $Y_{react,2}(t)$ are calculated using Eqs. (4.9) and (4.10). The objective (J_0) and the laser pulse parameters are optimized to get a maximum value of the cost functional in the genetic algorithm.

4.2.4 Laser pulse parameterization in the genetic algorithm

A pair of ultrashort laser pulses are optimized in the genetic algorithm. Each pulse consists of the Gaussian envelope function and a sinusoidal field. The laser field is expressed as,

$$\epsilon(t) = A_1\exp[-(t-t_1)^2/2\sigma_1^2].\sin(\omega_1 t + \alpha_1) + A_2\exp[-(t-t_2)^2/2\sigma_2^2].\sin(\omega_2 t + \alpha_2), \tag{4.13}$$

where A_1, A_2 are the amplitudes; ω_1, ω_2 are the frequencies, and α_1, α_2 are the phase of the laser pulses. σ_1 and σ_2 are the width parameters of the Gaussian envelope functions. The pump and dump laser pulses are positioned at t_1 and t_2, respectively. The parameters of the laser pulses i.e., A_1, A_2, ω_1, ω_2, α_1 and α_2 are optimized in the genetic algorithm. A set of these parameters define a laser field. A_1, A_2 vary from 0 to 0.5 a.u.; ω_1, ω_2 vary from 0 to 0.5 a.u., and α_1, α_2 vary from 0 to 0.5 a.u.. The genetic algorithm is a global search optimization technique based on the principles of genetics e.g., survival of the

fittest, selection, crossover, reproduction, mutation or randomization, etc. The specified parameters are involved in the optimization procedure. Every parameter value is stored in a binary number consisting of ten bits (0 or 1). A combination of these (six parameters of the sequence of the laser pulses) defines a chromosome. Therefore, a chromosome consisting of sixty bits determines a trial laser field. An initial population (set of chromosomes) is randomly selected from the defined parameter space. The cost functional expression is evaluated using the initial parameters. The cost functional value determines its fitness. In this work, the cost functional value closer to 2.0 is considered as the fittest for survival. The population undergoes various operations (e.g., selection, crossover, elitism, etc. as discussed in ref. [169, 201]) and creates a new generation. The cost functional is calculated for each chromosome of the new generation. These operations are repeated until the convergence of the cost functional. In this study, the cost functional shows good convergence behaviour [see Fig. (4.7)] to optimize the laser field parameters and it fulfils the convergence criteria within 30-50 generations.

4.3 Results and discussion

The laser field-induced tautomerization has been controlled in the two electronic states. The laser pulses convert the oxo tautomer to the hydroxy tautomer via the $\pi\pi^*$ state. The parameters of the laser pulses are optimized in optimal control theory using the genetic algorithm. The excited state-mediated conversion is performed using the *ab initio* calculated TDM and constant TDM (Condon approximation).

4.3.1 Optimal control using the *ab initio* calculated TDM

Here, the optimal calculations are performed employing the *ab initio* calculated TDM. It is clear from Fig. (4.3) that the $\pi\pi^*$ state-mediated tautomerization takes place in the presence of the optimal laser pulses. The optimal laser pulses

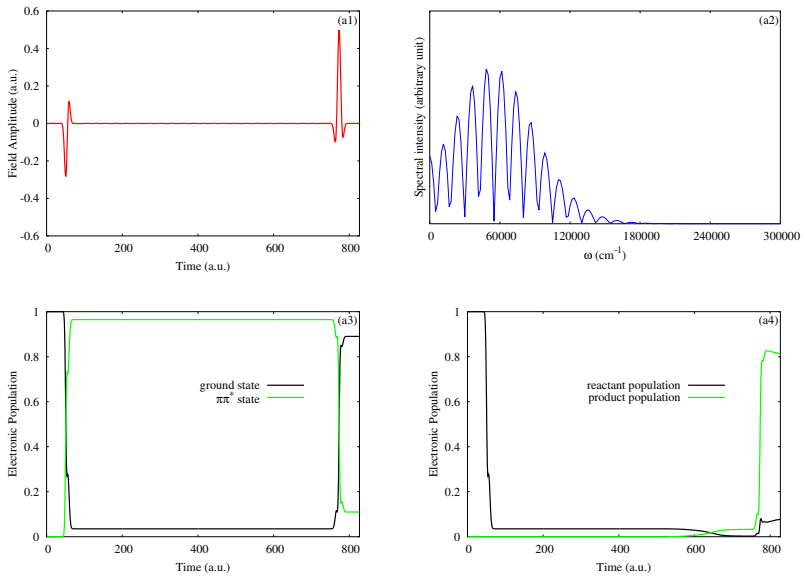

Figure 4.3: (a1) Temporal structure of the optimal laser pulse; (a2) frequency spectrum of it; (a3) population probabilities of the ground electronic state (black) and $\pi\pi^*$ state (green); (a4) population probabilities of the reactant (black) and product (green). These plots result from the optimal calculations using the *ab initio* calculated TDM.

i.e., the pump and dump pulses are designed using the genetic algorithm. The temporal structure of the optimal field appears as a smooth function. The frequency spectrum corresponding to the optimal field is broad and it has a carrier frequency of 48389 cm^{-1} [see Figs. 4.3(a1) and 4.3(a2)]. The optimal pump pulse is activated at 41 a.u. of time and it excites the initial state to the $\pi\pi^*$ state. It is noted from Fig. 4.3(a3) that about 94% of the WP population of the initial state is excited to the $\pi\pi^*$ state. The WP is propagated freely on the $\pi\pi^*$ state until the dump pulse is initiated. The WP has higher energy than the barrier on the $\pi\pi^*$ state. Hence, the WP of the $\pi\pi^*$ state crosses over the barrier. At the time when the WP arrives at the product configuration on the $\pi\pi^*$ state, the dump pulse is activated at 756 a.u. of time and it de-excites the WP to the ground electronic state. About 81% of the WP population reaches the product configuration via the $\pi\pi^*$ state. Therefore, the pump-dump events

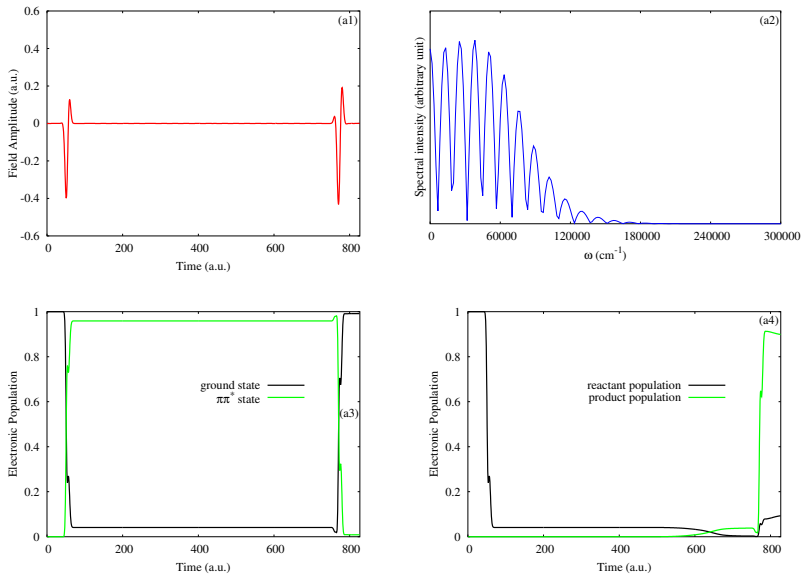

Figure 4.4: (a1) Temporal structure of the optimal laser pulse; (a2) frequency spectrum of it; (a3) population probabilities of the ground state (black) and $\pi\pi^*$ state (green); (a4) population probabilities of the reactant (black) and product (green). These plots result from the optimal calculations using the constant TDM (Condon approximation).

between the two electronic states result the intramolecular hydrogen transfer reaction, in other words, the phototautomerization of 4(3H)-pyrimidinone.

The shape of the time-evolved WP is interpreted from snapshots of the WP at various times. It is noted from Fig. (4.5) that the localized shape of the initial WP is not changed in the excitation process. A few nodes of the probability density of WP of the $\pi\pi^*$ state appear because of the steeper potential nature in the hydroxy tautomer region. The WP population in the product configuration in the $\pi\pi^*$ state is dumped to the ground electronic state. Therefore, a similar nodal pattern of the WP appears in the product region of the ground state. The objective is optimized and the cost functional is maximized using the genetic algorithm. It can be seen from Fig. 4.7(a1) that the cost functional reaches the convergence limit within 49 generations.

4.3.2 Optimal control using the constant TDM (Condon approximation)

Here, we have employed the TDM as a constant i.e., μ_{ge}=0.7 a.u. (Condon approximation) in the optimal calculations. It can be seen from Fig. 4.4(a1) that the temporal profile of the optimal laser field appears to be smooth. The carrier frequency of 38378 cm^{-1} is extracted from the frequency spectrum of the optimal laser pulses. The pump pulse is initiated at 36 a.u. of time and it excites the initial state vertically to the $\pi\pi^*$ state. The pump pulse induces a transition of 96% of the WP population. The WP is propagated freely on the $\pi\pi^*$ state and it crosses over the potential barrier. The WP arrives at the product region at 752 a.u. of time when the dump pulse is activated. Effectively, about 90% of the initial state population is transferred to the product configuration (hydroxy tautomer) via the $\pi\pi^*$ state.

It can be noted from Fig. 4.6(b1) that the structure of the initial WP is maintained in the excitation. The excited WP evolves on the $\pi\pi^*$ state in a localized fashion. The potential barrier and the steeper potential nature in the product configuration result a few nodes in the WP on the $\pi\pi^*$ state. As the shape of the WP is not varied in the de-excitation process, a few nodes appear in the WP at the product region [see Fig. (4.6)]. The objective for the tautomerization is optimized and laser pulse intensity is minimized in the optimization process. The cost functional shows good convergence behaviour and it is converged within 30 generations using the genetic algorithm [see Fig. (4.7)].

4.4 Summary

The $\pi\pi^*$ state-mediated tautomerization is controlled in the model system that composes the two electronic states i.e., the ground electronic state and $\pi\pi^*$ state. The optimal calculations are performed considering the *ab initio* calculated

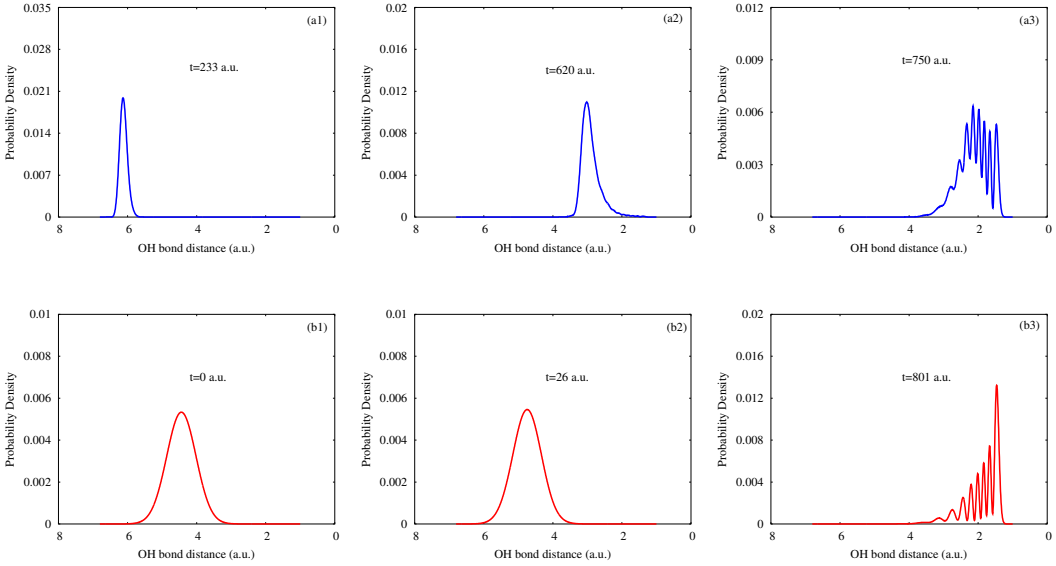

Figure 4.5: Shapshots of WP probability densities on the $\pi\pi^*$ state [at 233 a.u. (a1), 620 a.u. (a2) and 750 a.u. (a3)] and on the ground electronic state [at 0 a.u. (b1), 26 a.u. (b2) and 801 a.u. (b3)]. These WP probability densities are obtained from the optimal calculations using the *ab initio* calculated dipole.

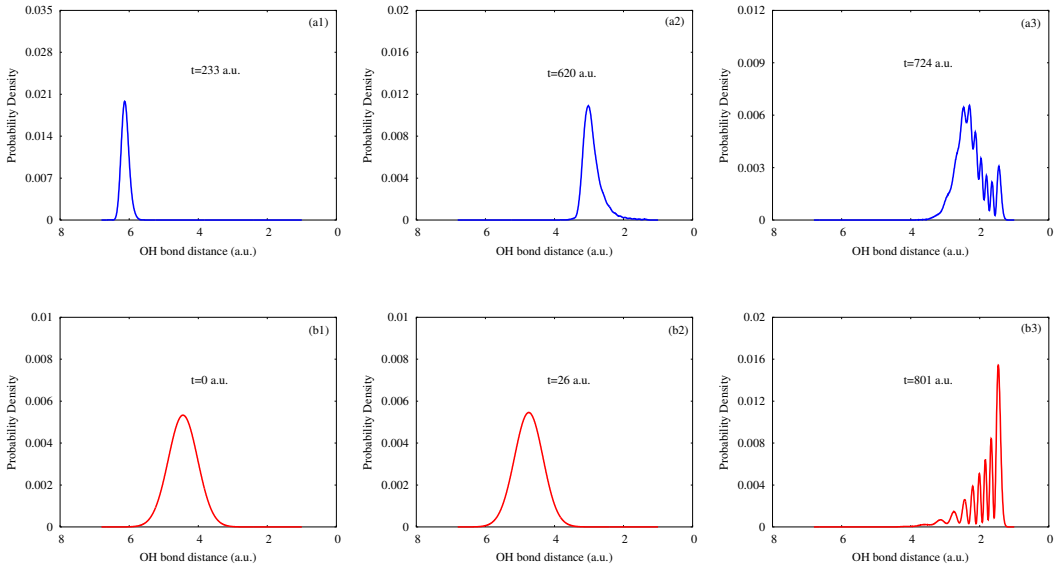

Figure 4.6: The above plots represent snapshots of WP probability densities on the $\pi\pi^*$ state [at 233 a.u. (a1), 620 a.u. (a2) and 750 a.u. (a3)] and on the ground electronic state [at 0 a.u. (b1), 26 a.u. (b2) and 801 a.u. (b3)]. These WP probability densities are obtained from the optimal calculations using the constant dipole (Condon approximation).

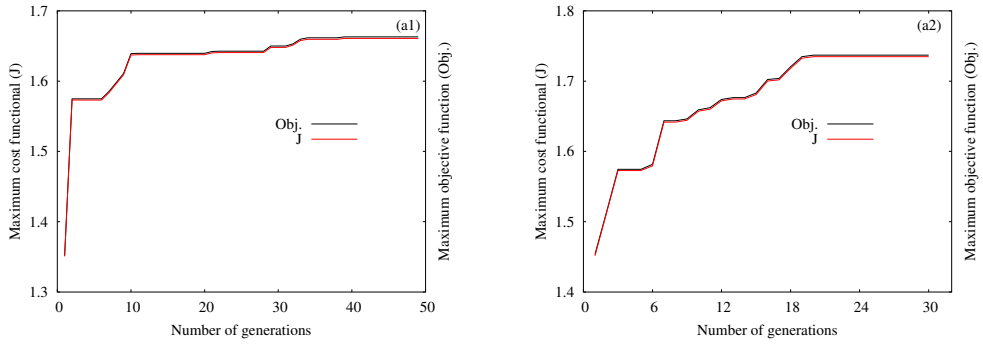

Figure 4.7: The optimization of the cost functional and the objective using the *ab initio* calculated TDM (a1) and the optimal calculations using the constant TDM (Condon approximation) (a2).

TDM and constant TDM (Condon approximation). A pair of ultrashort laser pulses are designed using the genetic algorithm. The tautomerization takes place through the pump-dump mechanism [41, 42] via the $\pi\pi^*$ state. The initial WP is excited by the optimal pump pulse to the $\pi\pi^*$ state. The excited WP freely moves and crosses over the barrier on the $\pi\pi^*$ state. When the WP reaches the product region on the $\pi\pi^*$ state, at that time the dump pulse is activated and it de-excites the WP back to the ground electronic state. Therefore, the optimal laser pulses transfer the reactant population to the product configuration in the ground state. The potential barrier and the topography of the product region introduce a few nodes in the WP. The constant dipole moment condition makes slightly better population transfer than the *ab initio* calculated TDM condition. The cost functional is maximized in the genetic algorithm.

Like the genetic algorithm, gradient-based algorithms (e.g., conjugate gradient method) can optimize laser pulse parameters to get a desired outcome of a reaction. Gradient-based algorithms solve coupled differential equations which are derived in optimal control theory whereas the genetic algorithm directly optimizes a cost functional. However, in the present study, the genetic algorithm works well to optimize the laser pulse parameters to perform the $\pi\pi^*$ state-mediated tautomerization.

Chapter 5

Optimal control of photodissociation of phenol using genetic algorithm

5.1 INTRODUCTION

Phenol is one of the important molecules relevant to many chemical reactions in the biological environment. For example, it is a chromophore of aromatic amino acid tyrosine. Therefore, a study of the photochemistry of phenol is of great interest from the experimental and theoretical point of view [207]. Electronic spectroscopy, vibrational spectroscopy, binding energy and structure have been extensively studied in phenol-water and phenol-ammonia clusters both experimentally and theoretically [208–217]. The excited state dynamics including the excited state proton transfer reaction has been studied in pump-probe experiments and with the aid of *ab initio* calculations [218–222] in phenol-water and phenol-ammonia clusters. Phenol-ammonia molecular clusters have long been considered an interesting prototype system for the excited state proton transfer reaction. Ground state proton transfer has been reported in a mid-IR spectroscopy study of the phenol-ammonia cluster [223]. Experimentally, the photodissociation of the OH bond of the phenol molecule from two excited singlet states was reported in an aqueous medium [224, 225]. Photo-induced

hydrogen atom elimination from the $\pi\sigma^*$ excited state of the phenol molecule was observed in a molecular beam experiment [226].

Ab initio electronic structure calculations were carried out to study the proton and electron transfer through the excited $\pi\sigma^*$ state of phenol [130, 227–229]. It appears from experimental as well as theoretical studies that three lowest electronic states viz., the ground electronic state, $\pi\pi^*$ state and $\pi\sigma^*$ state are essential for a study of the UV photochemistry of phenol [see Fig. (5.1)]. At the equilibrium geometry of the ground electronic state, the $\pi\pi^*$ is the first excited state that results from an excitation from the highest occupied molecular orbital (HOMO) (π character) to the lowest unoccupied molecular orbital (LUMO) (π^* character). The $\pi\sigma^*$ state is the second excited state and corresponds to an excitation to the 3s orbital of Rydberg type [227, 228]. The vertical excitation energies of the lowest $\pi\pi^*$ state and the lowest $\pi\sigma^*$ state was reported [227] at 4.46 and 5.77 eV, respectively. Extensive *ab initio* complete active space self-consistent field (CASSCF) calculations were performed to construct the multi-sheeted electronic potential energy surfaces (PESs) along three dissociative modes viz., OH stretching, CCOH torsional and COH bending angles to study the photo-induced hydrogen atom elimination of phenol [229].

Time-dependent wave packet dynamics was studied under a field free condition in a reduced dimensional model considering the three electronic states mentioned above and two modes (OH stretching coordinate and CCOH dihedral angle) [130]. Conical intersections (CIs) of the $\pi\pi^*$ and $\pi\sigma^*$ states at $\sim$1.16 Å and the $\pi\sigma^*$ and ground electronic states at 1.96 Å along the OH stretching coordinate were reported [130, 229]. Predissociation of the $\pi\pi^*$ state by the low lying repulsive $\pi\sigma^*$ state leads to a concerted OH bond dissociation. The initial state was prepared by launching different vibrational eigenstates of the

ground electronic state in the Frank-Condon region (FC) of the $\pi\pi^*$ state (δ excitation) in the absence of external field. The energetic minimum of the $\pi\pi^*$-$\pi\sigma^*$ CIs is higher in energy than the $|0,0\rangle$ and $|0,1\rangle$ initial states. Therefore, the latter vibrational eigenstates could not reach the S_0 and S_1 adiabatic asymptotic channels. Addition of one or more quantum of energy along the OH stretching coordinate could lead to the dissociation of $|1,0\rangle$, $|1,1\rangle$ and further high energy initial states at the S_0 and S_1 adiabatic asymptotes [130]. In addition to these observations a few interesting findings were reported in the literature [130] viz., the nonadiabatic dynamics at conical intersections (second CI controls the photodissociation in a specific channel) and the symmetry property considering the nodal structure of the time evolved wave packet. These observations motivated us to investigate how an optimal laser field couples with the considered states and modify the nonadiabatic dynamics and to see the outcome of the laser control from the ground electronic state instead of the upper excited state.

Control of the outcome of a quantum mechanical system by an external laser field has been extensively investigated within the mathematical framework of optimal control theory (OCT) [81, 155–157, 197, 198]. The geometric phase effect plays an important role in the branching ratio of controlled photodissociation [230] products of phenol studied with the optimal control theory framework. The genetic algorithm has been widely used in optimal control problems [107, 231, 232] such as optimal control of laser-induced molecular orientation [233], control of vibrational-rotational excitations [169, 234], molecular quantum gate operations [205, 206], control of laser-driven photodissociation of pyrrole [202, 203] and optimal control of laser-induced isomerization of malonaldehyde [204]. In the presence of an optimal laser pulse a system follows a specific path that maximizes the product yield. In this study, we have designed an optimal UV laser pulse that

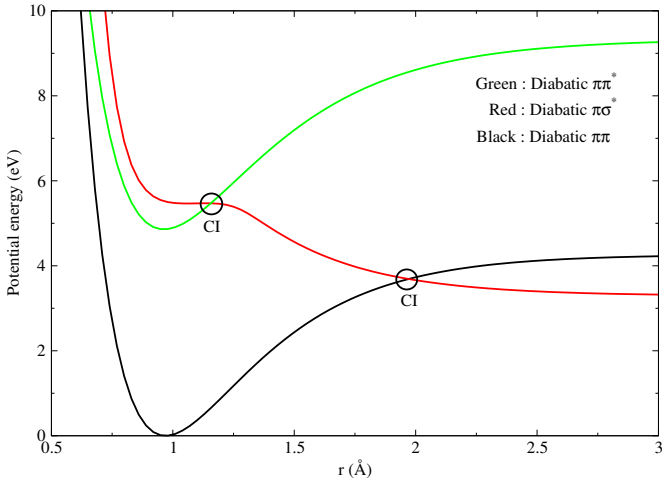

Figure 5.1: One dimensional cuts of the diabatic electronic ground state and the excited $\pi\pi^*$ and $\pi\sigma^*$ states of phenol along the OH stretching coordinate, r and for the coupling coordinate, $\theta = 0$.

maximizes the excited state mediated photodissociation in the lower two adiabatic asymptotic channels. An optimal laser pulse is designed in the optimal control theory framework using the genetic algorithm.

5.2 THEORY AND METHODOLOGY

5.2.1 Nuclear dynamics in the external laser field

Control of photodissociation of the OH bond of phenol is carried out with the three state and two mode model developed in the previous work [130]. In this reduced dimensional model, the OH stretching coordinate is the reaction coordinate, r and the CCOH dihedral angle, θ (rad) is the coupling coordinate. One dimensional cuts of the diabatic PESs for $\theta = 0$ are shown in Fig. (5.1). The equilibrium OH bond distance for the ground electronic state and the $\pi\pi^*$ diabatic electronic state occurs at 0.96 Å. Two dimensional diabatic and adiabatic PESs and diabatic interstate coupling elements as a function of the reaction coordinate and the coupling coordinate are shown in panels (a-c) of Fig. (5.2). There are two CIs marked with circles that occur between the S_0

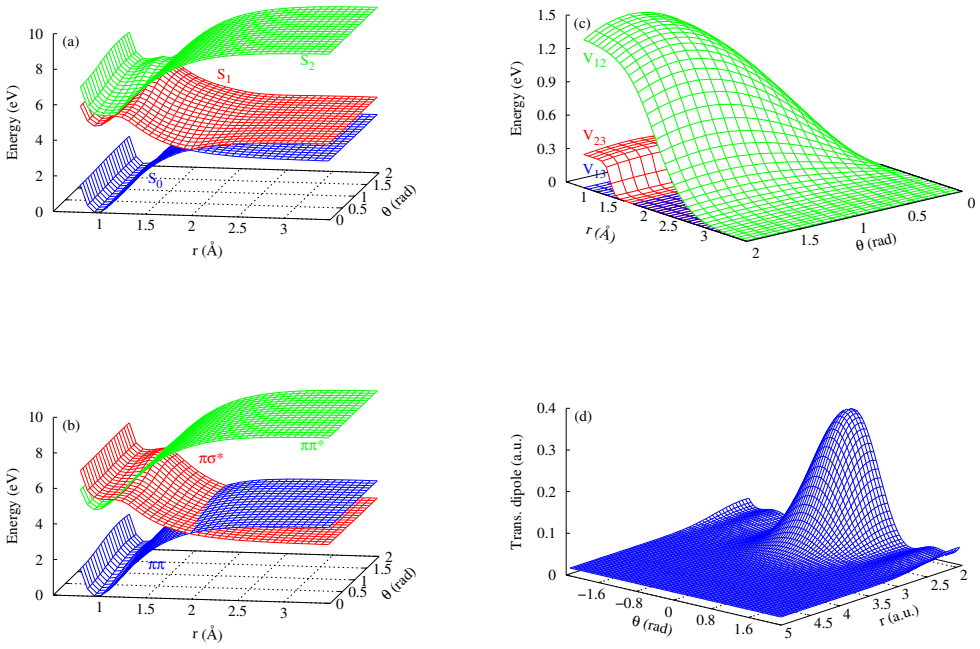

Figure 5.2: (a) Three-dimensional perspective plots of (a) adiabatic potential energy surfaces, (b) diabatic potential energy surfaces, (c) interstate coupling potentials and (d) transition dipole moment as a function of the reaction coordinate, r and the coupling coordinate, θ.

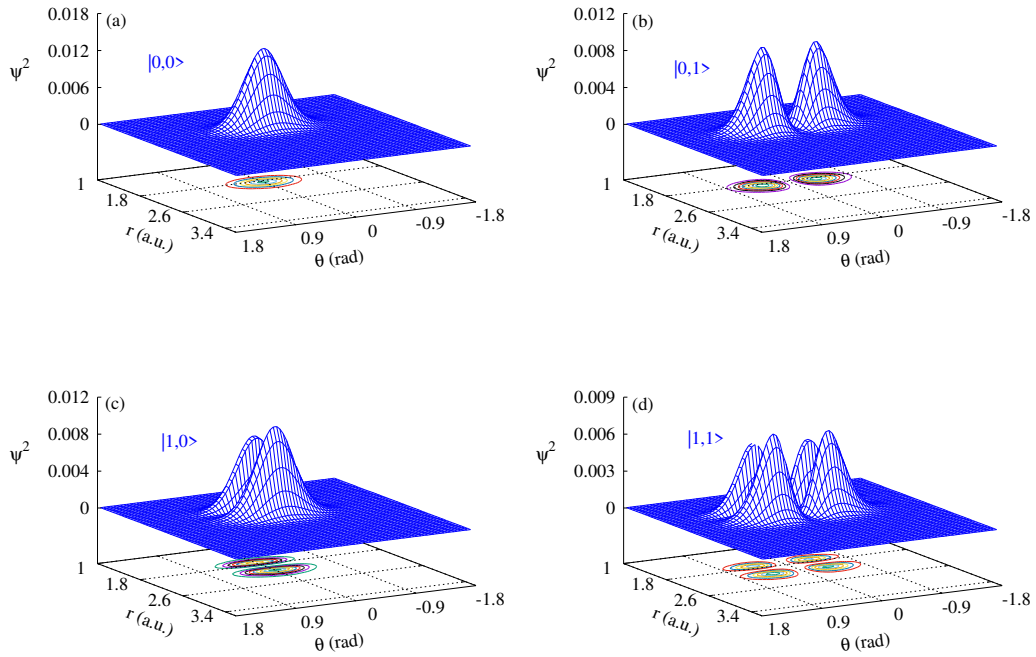

Figure 5.3: Eigenstates of the ground electronic state of phenol calculated using the pseudospectral method. The states are designated as $|n_r,n_\theta\rangle$, where n_r and n_θ represent the number of nodes along r and θ respectively.

and S_1 adiabatic PESs at 1.96 Å and between the S_1 and S_2 adiabatic PESs at 1.16 Å [see Fig. (5.2)]. Vibrational eigenfunctions of the ground electronic state and their eigenvalues are determined using the pseudospectral method [178, 179]. The theoretically calculated frequency values of the OH stretching and coupling coordinates are 3911 and 266 cm^{-1}, respectively. The experimental values for these frequencies are 3656 and 309 cm^{-1}, respectively [235, 236]. Therefore, the estimated fundamental frequency of both the modes compares well with their experimental value. The eigenfunctions are labeled $|n_r,n_\theta\rangle$, where n_r and n_θ are the number of nodes along the reaction coordinate, r and the coupling coordinate, θ, respectively [see Fig. (5.3)].

The electric field of the laser pulse interacts with the molecule. Within the semi-classical dipole approximation [87, 154], the molecular Hamiltonian of the three coupled diabatic electronic states can be written as,

$$\hat{H} = \hat{H}_0 + \hat{H}_{int}. \tag{5.1}$$

where

$$\hat{H}_0 = \hat{T}_N \begin{pmatrix} 1 & 0 & 0 \\ 0 & 1 & 0 \\ 0 & 0 & 1 \end{pmatrix} + \begin{pmatrix} \hat{V}_{11} & \hat{V}_{12} & \hat{V}_{13} \\ \hat{V}_{21} & \hat{V}_{22} & \hat{V}_{23} \\ \hat{V}_{31} & \hat{V}_{32} & \hat{V}_{33} \end{pmatrix}, \tag{5.2}$$

and

$$\hat{H}_{int} = -\begin{pmatrix} 0 & 0 & \hat{\mu}_{13} \\ 0 & 0 & 0 \\ \hat{\mu}_{13} & 0 & 0 \end{pmatrix} \epsilon(t). \tag{5.3}$$

In the above equation $\hat{H}_0$ is the Hamiltonian in the absence of the field and $\hat{T}_N$ is the nuclear kinetic energy operator. In the quasi diabatic representation the nuclear kinetic energy operator is diagonal and the interstate coupling is described by the potential energy operator. The diabatic electronic potential matrix elements are given by $\hat{V}_{ij}$. In this matrix the diagonal entries describe the diabatic electronic states and the off diagonal ones are the diabatic coupling with the neighboring states. The laser-molecule interaction Hamiltonian, $\hat{H}_{int}$ is given by [Eq. (5.3)]. In the latter $\hat{\mu}_{13}$ represents the transition dipole moment (TDM) operator for the $\pi\pi^* \leftarrow \pi\pi$ transition and $\epsilon(t)$ is the time-dependent electric field of the laser pulse. The TDM in the diabatic representation is nonzero [130]. The quantity $\hat{\mu}_{13}$ represents the x component of the TDM [see Fig. 5.2(d)]. The kinetic energy operator ($\hat{T}_N$), diabatic electronic states ($\hat{V}_{11}$, $\hat{V}_{22}$ and $\hat{V}_{33}$), diabatic coupling elements ($\hat{V}_{12}$, $\hat{V}_{23}$ and $\hat{V}_{13}$) and TDM ($\hat{\mu}_{13}$) used in the calculations are taken from the previous work [130].

The time evolution of the wave function, $|\Psi(t)\rangle$ is described by the time-dependent Schrödinger equation

$$i\hbar\frac{\partial}{\partial t}|\Psi(t)\rangle = \hat{H}|\Psi(t)\rangle. \tag{5.4}$$

The above equation is solved numerically in the diabatic electronic representation using the second-order split operator [171, 200] and the fast Fourier transformation (FFT) [172] methods. The wave packet is propagated on the coupled [179, 237] PESs for 700 fs with a time step of $\Delta t = 0.02$ fs. The coordinate grid for the calculations consists of 512 points along the reaction coordinate, r ranging from 1.0 a_0 to 30.0 a_0 and 128 points along the coupling coordinate θ ranging from -π to +π. A sine-damping function [237]

$$f(r_i) = \sin\left[\frac{\pi}{2}\frac{r_{mask} + \Delta r_{mask} - r_i}{\Delta r_{mask}}\right], \qquad r_i \geq r_{mask}. \tag{5.5}$$

is employed to absorb the wave function components at the grid boundary to avoid reflection or wrap around. The damping function is activated at $\mathrm{r_{mask}}$=26.0 a_0 and it smoothly decays from 1.0 to 0.0 in the interval of $\Delta\mathrm{r_{mask}}$(=$\mathrm{r_{max}}$-$\mathrm{r_{mask}}$). The time-dependent diabatic and adiabatic electronic populations are estimated by calculating the expectation values of the associated projection operators, $|\psi^d\rangle\langle\psi^d|$ and $|\psi^a\rangle\langle\psi^a|$ [238] as

$$P_i^d(t) = \langle\Psi(t)|\psi_i^d\rangle\langle\psi_i^d|\Psi(t)\rangle, \qquad i = 1, 2, 3 \tag{5.6}$$

$$P_i^a(t) = \langle\Psi(t)|\psi_i^a\rangle\langle\psi_i^a|\Psi(t)\rangle, \qquad i = 1, 2, 3 \tag{5.7}$$

The dissociation probability is determined by calculating the time-integrated flux through a dividing surface located at, $r = r_{flux}$, at the asymptotic reaction channels as follows

$$P^D(t) = \frac{\hbar}{\mu}\int_{t=0}^{t} Im\left[\langle\Psi(r,\theta,t)|\frac{\partial\Psi(r,\theta,t)}{\partial r}\rangle\right]\Bigg|_{r=r_{flux}} dt. \tag{5.8}$$

where $\mu = \frac{m_H m_O}{m_H + m_O}$ in which m_H and m_O represent the masses of H and O, respectively.

5.2.2 Cost functional and genetic algorithm

The cost functional is formulated in the mathematical framework of optimal control theory [81, 156, 157] with a target to optimize a desired objective with

optimal values of laser field parameters. Maximization of the cost functional is performed under different scenarios with the aid of the genetic algorithm [107, 120, 125] to optimize laser field parameters and to get the desired outcome of the system. In this study, the functional form of the cost functional $J[\epsilon(t)]$ used in the genetic algorithm is given by

$$J[\epsilon(t)] = J_o - \alpha_0 \int_0^T |\epsilon(t)|^2 dt, \tag{5.9}$$

In the above equation α_0 is a penalty factor to the field intensity and J_o is the objective function and it is defined as a sum of the time accumulated flux on the S_0 and S_1 asymptotic channels. The time integrated outgoing flux is calculated at time, $t = T$ where T is the total duration of the wave packet propagation [Eq. (5.8)].

The initial guess field for the laser pulse in the genetic algorithm reads

$$\epsilon(t) = \epsilon_0 \sin(\omega t) \cdot \mathrm{s}(t), \tag{5.10}$$

where ω is the carrier frequency which is varied from 38,627 cm^{-1} to 49,600 cm^{-1} (in the range of 10,974 cm^{-1}) and ϵ_0 is the amplitude of the field which is varied from 0 to 0.03 a.u.. The envelope function, $\mathrm{s}(t)$ modulates the laser field and ensures that the field goes to zero smoothly at the initial and final time. Generally, it is defined by four positive time parameters, t_0, t_1, t_2 and t_3 where $t_0 < t_1 < t_2 < t_3$ and is given as

$$\mathrm{s}(t) = \begin{cases} \sin^2\left[\frac{\pi}{2}\left(\frac{t-t_0}{t_1-t_0}\right)\right] & \text{for} \quad t_0 \le t \le t_1, \\ 1 & \text{for} \quad t_1 \le t \le t_2, \\ \sin^2\left[\frac{\pi}{2}\left(\frac{t_3-t}{t_3-t_2}\right)\right] & \text{for} \quad t_2 \le t \le t_3 = T. \end{cases} \tag{5.11}$$

Normally, t_0 is defined as 0 and t_3 as T. The time duration t_0 to t_1 is the rise time and t_2 to t_3 is the switch off period of the pulse. The duration

t_1 to t_2 is a plateau region where the envelope function reaches its maximum value, 1. The amplitude (ϵ_0), frequency (ω) and two time parameters t_1 and t_2 are varied to maximize the cost functional ($J[\epsilon(t)]$). The genetic algorithm is a global search optimization tool consisting of principles of genetics viz., survival of the fittest, selection and reproduction through crossover combined with mutation or randomization. Each parameter value is stored in a binary number containing ten bits (0 or 1). The chromosome consists of four parameter strings containing total 40 bits with different combinations of these parameters. The genetic algorithm finds the optimal solution from the said possibilities. The calculation starts with an initial guess population (population or total number of individuals in a generation, N=10). The individuals (chromosome, a set of parameters, define an electric field) in this population are randomly selected from parameter space that is defined earlier. Using a set of parameters *i.e.*, chromosome, we evaluated the cost functional value that measures its fitness. In this study, the cost functional value near to 1.0 makes the chromosome more fit for survival. The population evolves through various genetic operations such as tournament selection, elitism, mutation and crossover as suggested in Ref. [169]. These operations are performed in every generation until the convergence of the cost functional is achieved. The cost functional is converged with the optimal laser parameter set within 25-80 generations as shown in Figs. 5.4(a5), 5.4(b5), 5.5(c5) and 5.5(d5). It can be seen that the cost functional increases with the number of generation until it reaches the convergence.

5.3 RESULTS AND DISCUSSION

The initial states prepared from different vibrational levels of the electronic ground state of phenol are optimally excited in order to assess their impact on the photodissociation dynamics. The optimal solution for the laser parameters is obtained using the genetic algorithm in an effort to optimize the total dissociative

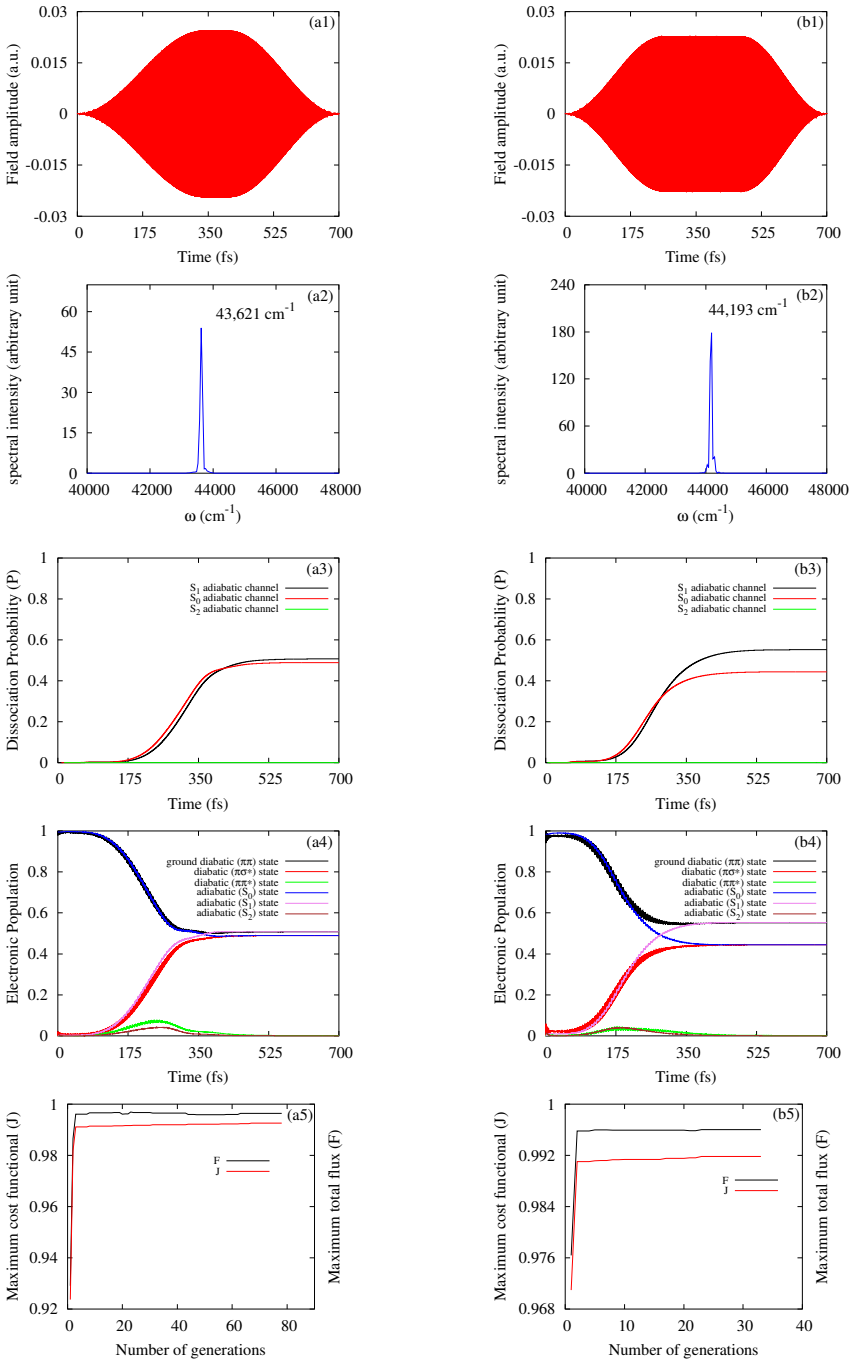

Figure 5.4: Figures (a1)-(a5) and (b1)-(b5) are obtained with the $|0,0\rangle$ and $|0,1\rangle$ initial state, respectively. The temporal profile of the optimal laser field (panels a1 and b1), the frequency spectrum of the optimal pulse (panels a2 and b2), the time integrated dissociative flux at the adiabatic asymptote (panels a3 and b3), the electronic population probability (panels a4 and b4) and the cost functional as well as the total dissociative flux calculated at each generation in the genetic algorithm (panels a5 and b5) are shown (see the text for details).

flux. Fig. (5.4) and Fig. (5.5) show that the optimal laser pulses that optically excite the system and lead to the OH bond dissociation (∼100%) of phenol at both S_0 and S_1 asymptotes.

5.3.1 Photodissociation of the $|0,0\rangle$ and $|0,1\rangle$ vibrational levels of the ground electronic state

The initial wave function of the $|0,0\rangle$ and $|0,1\rangle$ vibrational eigenstates of the ground state are subjected to a Frank-Condon transition to the excited state with the aid of the optimal laser pulse. For the $|0,0\rangle$ and $|0,1\rangle$ initial conditions, central frequencies of 43,621 cm^{-1} (229 nm) and 44,193 cm^{-1} (226 nm) of the optimal laser pulse, respectively, are extracted from the frequency spectrum (cf., Figs. 5.4(a2) and 5.4(b2)). When these eigenstates are subjected to a vertical transition to the $\pi\pi^*$ state in the absence of a laser pulse hardly any dissociation (less than 5%) occurs at both S_0 and S_1 asymptotes [130]. These wave functions have energy less than 50% of the potential barrier present on the $\pi\pi^*$ state along the reaction coordinate.

The laser field parameters are optimized using the genetic algorithm in order to maximize the cost functional [Eq. (5.9)] constructed in the framework of optimal control theory. An optimal field driven mechanism is understood with the help of the variation in population probability and the total dissociative flux in time as shown in Figs. 5.4(a3), 5.4(a4), 5.4(b3) and 5.4(b4), respectively. The laser field pumps a small portion of the wave packet at each time step from the ground state to the excited state in the Franck-Condon region under the resonance condition. The excited wave packet predominantly populates the $\pi\sigma^*$ state and a very small portion of the high energy component (less than 8%) moves to the $\pi\pi^*$ state for the $|0,0\rangle$ and $|0,1\rangle$ initial conditions. The $\pi\sigma^*$ state is populated in time through the intensity borrowing effect discussed elsewhere [230]. Due to the non-vanishing diabatic coupling in the Frank-Condon region,

a small portion of the wave packet on the $\pi\pi^*$ state moves to the $\pi\sigma^*$ state and also comes back in time to the $\pi\pi^*$ state leading to interference as shown in Figs. 5.6(a3) and 5.6(b3). The population probability on the $\pi\pi^*$ state slowly rises in time and reaches a maximum approximately at 251 fs (about 7% of the population) and 179 fs (about 4% of the population) for the $|0,0\rangle$ and $|0,1\rangle$ initial state, respectively. The wave packet populations in the Frank-Condon region of the $\pi\sigma^*$ state and the $\pi\pi^*$ state reach the (S_1-S_2) CIs and then move to the $\pi\sigma^*$ state away from the Frank-Condon region because of the repulsive nature of the latter state. It can be seen from Figs. 5.4(a4) and 5.4(b4) that the wave packet population on the ground electronic state monotonically decreases whereas, it increases on the $\pi\sigma^*$ state in time. The wave packet population reaches the (S_0-S_1) CIs within ∼15 fs and dissociates through both the channels. The wave packet reaches the S_0 and S_1 adiabatic asymptotes in ∼15 fs. The high energy component of the wave packet reaches the S_1 asymptote. The population probability in both the channels converges in 700 fs. For the $|0,0\rangle$ initial condition the S_1 asymptotic channel gets (∼51%) slightly more dissociative flux as compared to the S_0 asymptotic channel (∼49%). On the other hand, the S_1 asymptotic channel gets (∼55%) more dissociative flux than the S_0 asymptotic channel (∼44%) for the $|0,1\rangle$ initial condition as shown in Figs. 5.4(a3) and 5.4(b3). The initial wave function prepared with the $|0,0\rangle$ vibrational eigenstate bifurcates and spreads along the coupling coordinate, θ on the $\pi\sigma^*$ state. The wings of the wave packet follow the adiabatic path leading to the dissociation on the S_1 asymptotic channel. On the other hand, the wave packet localized on the reaction coordinate (r) prefers to follow the diabatic path and leads to a dissociation on the S_0 asymptotic channel. In contrary, when one quantum of energy is added along the coupling coordinate *i.e.*, for the $|0,1\rangle$ initial state the S_1 adiabatic channel gets comparatively higher flux about 11% than the S_0 channel as shown in Figs. 5.4(a3) and 5.4(b3). For the $|0,1\rangle$ initial state

the wave packet on the $\pi\sigma^*$ state spreads along the coupling coordinate θ, (cf., Fig. 5.6(b2)). Hence the wave packet on the $\pi\sigma^*$ state prefers to follow the adiabatic path for the dissociation. Therefore, under the optimal condition the photo-induced dissociation preferentially occurs at the S_1 asymptotic channel for the $|0,1\rangle$ initial condition.

Some interesting symmetry properties of the wave packet follow from Fig. (5.6). The diabatic interstate coupling between the $\pi\pi^*$ and $\pi\sigma^*$ states determines the symmetry property of the wave packet. This coupling element is an odd function of the coupling coordinate, θ. For the $|0,0\rangle$ and $|0,1\rangle$ initial conditions, the snapshots of the wave packet probability density at a given time evolving on the diabatic ground state, $\pi\sigma^*$ state and $\pi\pi^*$ state are shown in Fig. (5.6). For the $|0,0\rangle$ initial wave function, the ground state wave packet is symmetric [see Fig. 5.6(a1)] along the coupling coordinate. It can be seen from the contour of Fig. 5.6(a2) that the wave packet on the $\pi\sigma^*$ state develops a nodal line at $\theta = 0$ for the $|0,0\rangle$ initial state. This nodal line results from the geometric phase effect of the nuclear wave function. The components of the time evolved wave packet move with the opposite phase around S_1-S_2 CIs and interfere destructively at $\theta = 0$. For the $|0,1\rangle$ initial wave function, the ground state wave packet is an odd function of the coupling coordinate θ and a nodal line develops at $\theta = 0$ [see Fig. 5.6(b1)]. The wave packet on the $\pi\sigma^*$ state is symmetric with respect to the coupling coordinate because of the diabatic coupling. In the field induced excitation, it can be seen from Figs. 5.6(a3) and 5.6(b3) that the wave packet on the $\pi\pi^*$ state restores its initial shape as the $\pi\pi^*$ state has a potential well analogous to the ground state. The distortion of the shape of the wave packet occurs on the $\pi\pi^*$ state because of the interference with the wave packet component of the $\pi\sigma^*$ state [see Figs. 5.6(a3) and 5.6(b3)]

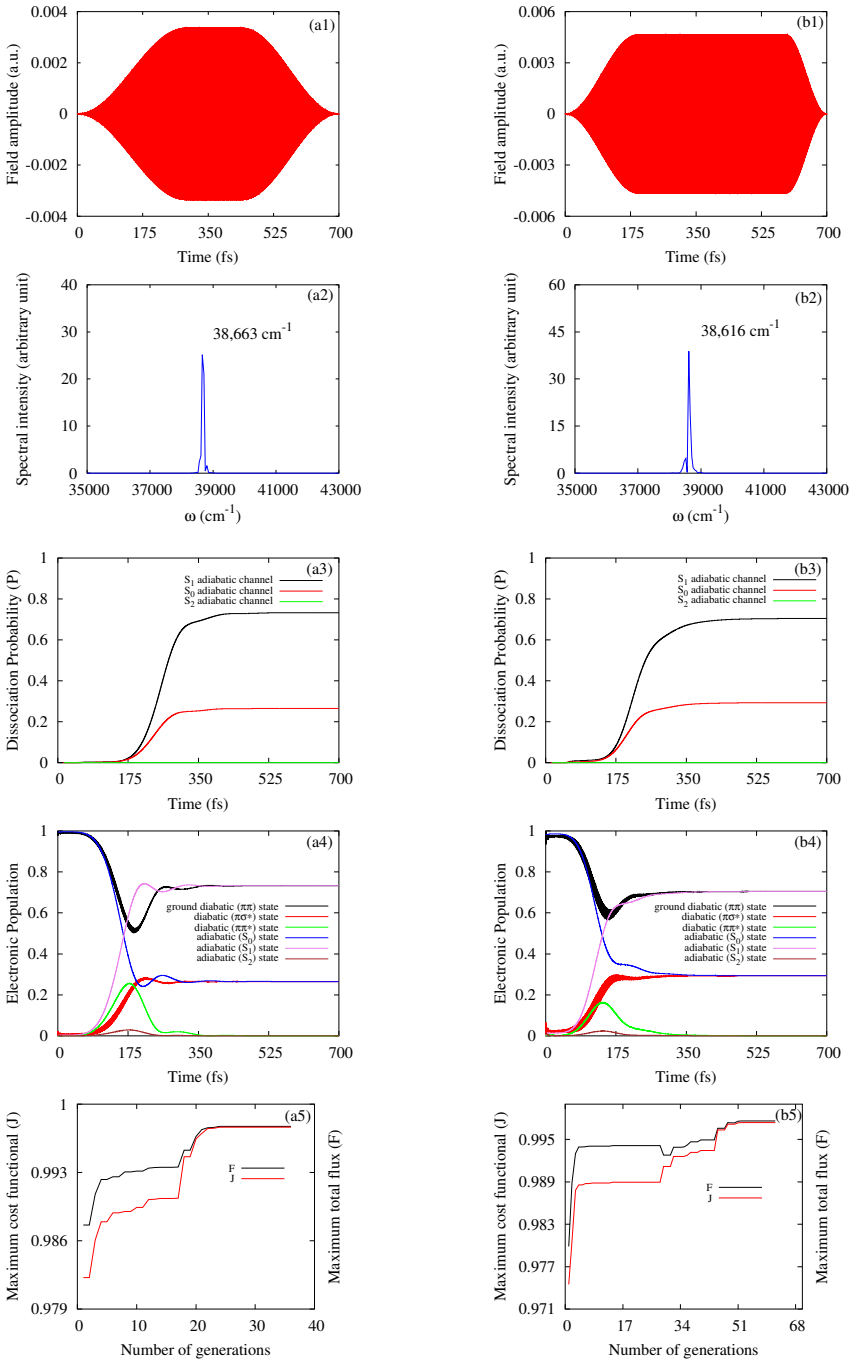

Figure 5.5: Figures (a1)-(a5) and (b1)-(b5) are obtained with the $|1,0\rangle$ and $|1,1\rangle$ initial state, respectively. The temporal profile of the optimal laser field (panels a1 and b1), the frequency spectrum of the optimal pulse (panels a2 and b2), the time integrated dissociative flux at the adiabatic asymptote (panels a3 and b3), the electronic population probability (panels a4 and b4) and the cost functional as well as the total dissociative flux calculated at each generation in the genetic algorithm (panels a5 and b5) are shown (see the text for details).

Initial state	J	Dissociation	ϵ_{max}
$\|0,0\rangle$	0.992616	0.996373	2.4457×10^{-2}
$\|0,1\rangle$	0.991823	0.996025	2.2757×10^{-2}
$\|1,0\rangle$	0.997652	0.997736	3.3724×10^{-3}
$\|1,1\rangle$	0.997397	0.997626	4.6628×10^{-3}

Table 5.1: Results of the photodissociation in the presence of the optimal UV laser pulse of a time duration of 700 fs with different vibrational states ($|0,0\rangle$, $|0,1\rangle$, $|1,0\rangle$ and $|1,1\rangle$) as the initial states. Optimal control calculations have been performed for $\alpha_0 = 0.001$. ϵ_{max} refers to the maximum amplitude value of the optimized laser pulse and J is the value of the cost functional. All parameters are in a.u..

5.3.2 Photodissociation of the $|1,0\rangle$ and $|1,1\rangle$ vibrational levels of the ground electronic state

It is shown in Fig. (5.5) that the initial wave function prepared from the $|1,0\rangle$ and $|1,1\rangle$ vibrational levels of the ground electronic state leads to photodissociation with the optimized UV laser pulse. The central frequencies of the optimal UV pulses are 38,663 cm^{-1} (259 nm) and 38,616 cm^{-1} (259 nm) obtained from the frequency spectra [see Figs. 5.5(a2) and 5.5(b2)] with the $|1,0\rangle$ and $|1,1\rangle$ initial conditions, respectively. When one quantum of energy is added to the OH stretching coordinate viz., the $|1,0\rangle$ and $|1,1\rangle$ states they overcome the energy barrier through the barrier crossing mechanism under the field free condition [130].

The optimal UV laser pulse excites the system from the ground state to the excited state in the Frank-Condon region. It is observed that the optimal field excites a small portion of the wave function in time to both the $\pi\pi^*$ and $\pi\sigma^*$ states. It can be seen from Figs. 5.5(a4) and 5.5(b4) that the wave packet population on the $\pi\pi^*$ state raises to a maximum at 178 fs (about 26% of the population) and 143 fs (about 16% of the population) for the $|1,0\rangle$ and $|1,1\rangle$ initial conditions, respectively. The $\pi\sigma^*$ state population increases in time via the intensity borrowing effect as discussed earlier. The wave packet population

on the $\pi\sigma^*$ state reaches the S_1-S_2 CI and rapidly moves to the repulsive region of the $\pi\sigma^*$ state. A small portion of the wave packet population of the $\pi\sigma^*$ state transfers to the attractive well region of the $\pi\pi^*$ state due to the non-vanishing diabatic coupling element. This wave packet population interferes with the wave packet population of the $\pi\pi^*$ state [see Figs. 5.7(a3) and 5.7(b3)]. The wave packet components on the $\pi\pi^*$ state overcome the energy barrier through S_0-S_1 CI and populates the $\pi\sigma^*$ state. The wave packet population reaches the S_0 and S_1 adiabatic asymptotes in about 15 fs. The population probability convergences in 700 fs for both the $|1,0\rangle$ and $|1,1\rangle$ initial conditions. For the $|1,0\rangle$ and $|1,1\rangle$ initial states the time evolved wave packet has sufficient energy to reach the S_1 adiabatic asymptote. Therefore, the photodissociation takes place predominantly in the adiabatic asymptote of S_1 over that of the S_0 state. The S_1 adiabatic channel gets ($\sim$73%) more dissociative flux than the S_0 adiabatic channel ($\sim$27%) for the $|1,0\rangle$ initial state. Similarly, for the $|1,1\rangle$ initial state the S_1 adiabatic channel gets ($\sim$70%) more dissociative flux as compared to the S_0 adiabatic channel ($\sim$29%). The $|1,1\rangle$ initial state wave function has a nodal line along the coupling coordinate as well as along the reaction coordinate [see Fig. 5.7(a1)] whereas, only one nodal line along the reaction coordinate appears for the $|1,0\rangle$ initial state. Addition of one quantum of energy along the coupling coordinate i.e., for the $|1,1\rangle$ initial state, the lower adiabatic channel (S_0 channel) gets about 2% more dissociation as compared to the $|1,0\rangle$ initial condition [see Figs. 5.5(a3) and 5.5(b3)]. We observed the "odd-even" effect for the $|1,1\rangle$ initial condition in the presence of the optimal laser field. A similar effect was reported under the field free condition in the previous article [130]. A similar effect was also reported by Baer *et al.* in a state-to-state scattering study within a quasi-Jahn-Teller model [239].

The snapshots of the wave packet probability density shown in Fig. (5.7)

reveal the symmetry properties of the wave packet on different electronic states. For the $|1,0\rangle$ initial state condition, it is seen that the wave packet on the ground state is an even function of the coupling coordinate, θ. The probability density on the $\pi\sigma^*$ state has a nodal line along the coupling coordinate for the $|1,0\rangle$ initial condition. This asymmetric nature of the wave packet arises because of the diabatic coupling between the $\pi\pi^*$ and $\pi\sigma^*$ states. For the $|1,1\rangle$ initial condition, it can be seen from Fig. 5.7(b1) that the wave packet on the ground state is an odd function of the coupling coordinate θ. This initial state has a nodal line along the coupling coordinate at $\theta = 0$. The wave packet on the $\pi\sigma^*$ state is symmetric with respect to the coupling coordinate shown in Fig. 5.7(b2). The wave packet maintains its original shape on the $\pi\pi^*$ state for both the initial conditions as shown in Figs. 5.7(a3) and 5.7(b3). Additional nodes in the wave packet appear on the $\pi\pi^*$ state because of the interference due to the interstate ($\pi\pi^*$-$\pi\sigma^*$) diabatic coupling.

It is shown in Figs. 5.4(a2), 5.4(b2), 5.5(a2) and 5.5(b2) that the optimal frequency spectrum of the $|0,0\rangle$ and $|1,0\rangle$ initial states overlap with the frequency spectrum of the $|0,1\rangle$ and $|1,1\rangle$ initial states, respectively. The carrier frequencies of the optimal pulses of the $|1,0\rangle$ and $|1,1\rangle$ initial conditions (38,663 and 38,616 cm^{-1}, respectively) are lower by about $\sim$5267 cm^{-1} than for the $|0,0\rangle$ and $|0,1\rangle$ initial conditions (43,621 and 44,193 cm^{-1}, respectively). This can be explained from the vibrational levels of the ground state and the excitation mechanism that follows under the optimal condtions. The $|1,0\rangle$ and $|1,1\rangle$ vibrational eigenstates have energies 6113 and 6354 cm^{-1}, respectively, which is higher (by $\sim$3,900 cm^{-1}) than the $|0,0\rangle$ (2202 cm^{-1}) and $|0,1\rangle$ (2468 cm^{-1}) vibrational levels. For the $|0,0\rangle$ and $|0,1\rangle$ initial states the wave function is excited almost entirely to the $\pi\sigma^*$ state which is the higher energy electronic state as compared to the $\pi\pi^*$ state in the Frank-Condon region. However, the optical excitation of the $|1,0\rangle$

and $|1,1\rangle$ initial states occurs to both the $\pi\pi^*$ and $\pi\sigma^*$ states. Therefore, the $|0,0\rangle$ and $|0,1\rangle$ initial states required higher frequency pulse to maximize the total dissociative flux under the resonance condition than the $|1,0\rangle$ and $|1,1\rangle$ states. The optimal pulse for the $|1,0\rangle$ initial condition has a higher carrier frequency than for the $|1,1\rangle$ initial condition. This is because of the lower energy of the $|1,0\rangle$ eigenstate as compared to the $|1,1\rangle$ eigenstate. In contrast to the above the optimal pulse for the $|0,0\rangle$ initial condition has a lower carrier frequency than for the $|0,1\rangle$ condition. This can be explained from the excitation mechanism. It can be seen from Figs. 5.4(a4) and 5.4(b4) that the slightly large fraction (about 3%) of the wave function for the $|0,0\rangle$ initial condition is excited to the $\pi\pi^*$ state than the $|0,1\rangle$ initial condition. Although it is a less favored excitation under the optimal condition, a smaller fraction of the ground state wave packet follows less energetic excitation path for the $|0,0\rangle$ initial state. Therefore, the optimal pulse for the $|0,0\rangle$ initial state has a lower frequency than the $|0,1\rangle$ initial state.

The dissociation probability nearly reaches a maximum ($\sim$100%) for these initial states for $\alpha_0 = 0.001$ [cf., Table (5.1)]. In all cases the optimal pulse has a simple structure with the intensity of 0.1-25 TW/cm^2 as shown in Figs. 5.4(a1), 5.4(b1), 5.5(a1) and 5.5(b1). These smooth structured UV pulses are experimentally feasible. Figures 5.4(a5), 5.4(b5), 5.5(a5) and 5.5(b5) show the convergence behavior of the cost functional in the genetic algorithm. The cost functional value increases in every generation and converges to a constant value in 30-80 generations. Therefore, convergence of the cost functional in the genetic algorithm is found to be excellent.

5.3.3 Effect of penalty factor (α_0) on the dissociation

In order to explore the effect of α_0, optimal simulations are performed for different values of α_0. The penalty factor, α_0 in Eq. (5.9) limits laser field energy to

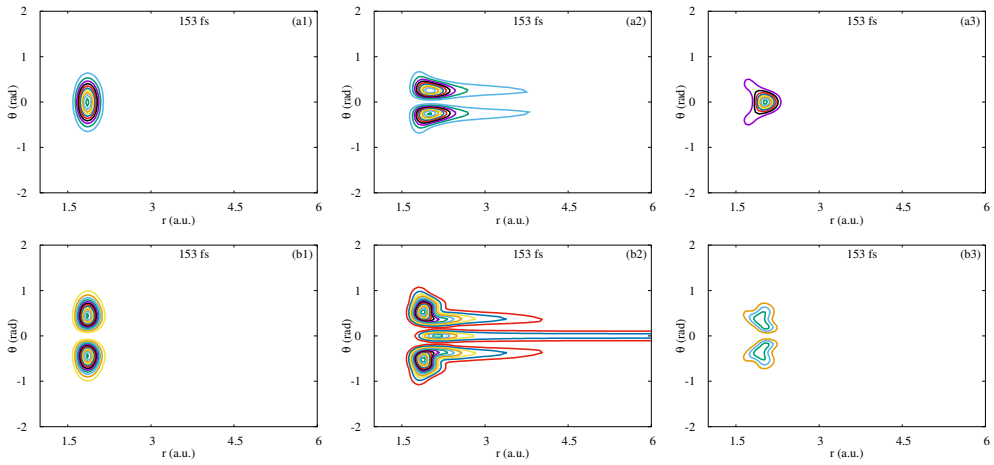

Figure 5.6: Snapshots of the wave packet probability density as a function of the OH stretching coordinate (r) and the coupling coordinate (θ): (a1) probability density on the ground state at 153 fs, (a2) probability density on the $\pi\sigma^*$ state at 153 fs and (a3) probability density on the $\pi\pi^*$ state at 153 fs for the $|0,0\rangle$ initial state. (b1) probability density on the ground state at 153 fs, (b2) probability density on the $\pi\sigma^*$ state at 153 fs and (b3) probability density on the $\pi\pi^*$ state at 153 fs for the $|0,1\rangle$ initial state.

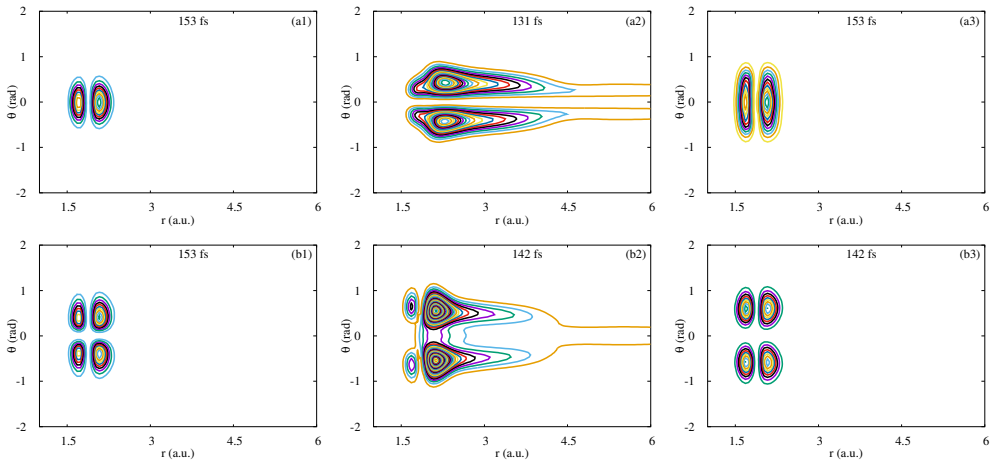

Figure 5.7: Snapshots of the wave packet probability density as a function of the OH stretching coordinate (r) and the coupling coordinate (θ): (a1) probability density on the ground state at 153 fs, (a2) probability density on the $\pi\sigma^*$ state at 131 fs and (a3) probability density on the $\pi\pi^*$ state at 153 fs for the $|1,0\rangle$ initial state. (b1) probability density on the ground state at 153 fs, (b2) probability density on the $\pi\sigma^*$ state at 142 fs and (b3) probability density on the $\pi\pi^*$ state at 142 fs for the $|1,1\rangle$ initial state.

Initial state	α_0	J	Dissociation	ϵ_{max}
$\|0,0\rangle$	0.001	0.992616	0.996373	2.4457×10^{-2}
	0.01	0.973432	0.993514	1.5630×10^{-2}
	0.1	0.801899	0.935423	1.5484×10^{-2}
$\|0,1\rangle$	0.001	0.991823	0.996025	2.2757×10^{-2}
	0.01	0.964716	0.992228	1.8094×10^{-2}
	0.1	0.835364	0.958104	1.3138×10^{-2}
$\|1,0\rangle$	0.001	0.997652	0.997736	3.3724×10^{-3}
	0.01	0.994738	0.997826	7.5072×10^{-3}
	0.1	0.942949	0.994334	8.1525×10^{-3}
$\|1,1\rangle$	0.001	0.997397	0.997626	4.6628×10^{-3}
	0.01	0.987711	0.997593	1.1760×10^{-2}
	0.1	0.986148	0.996798	4.3402×10^{-3}

Table 5.2: Results of the photodissociation in the presence of the optimal UV laser pulse of time duration 700 fs with different vibrational levels ($|0,0\rangle$, $|0,1\rangle$, $|1,0\rangle$ and $|1,1\rangle$) as the initial states. Optimal control calculations have been performed at different values of α_0 (0.1, 0.01 and 0.001). The quantity ϵ_{max} refers to the maximum amplitude value of the optimized laser pulse and J is the value of the cost functional. All parameters are in a.u..

maximize the cost functional value. In general, variation of the α_0 value results different field amplitudes of the laser pulse under the optimal condition. We have considered higher values of α_0 *i.e.*, 0.01 and 0.1. The laser pulse time duration is set to 700 fs in these optimal calculations. All the initial parameters for the genetic algorithm are kept same for different α_0 values. The results obtained from these calculations are tabulated in Table (5.2). It can be clearly seen that the cost functional values (J) under the optimal condition decreases for the lower value of α_0. In addition, the dissociation yield reduces in a similar way except for the $|1,0\rangle$ initial condition for α_0=0.01. In the latter condition a small increase in the dissociation yield results from higher value of ϵ_{max} under the optimal condition. Considering dissociation yields and cost functional values optimization processes are found to be good for a very small value of α_0 *i.e.*, 0.001. ϵ_{max} values under the optimal condition are in the range of 0.003-0.025 a.u. for different values of α_0.

5.4 SUMMARIZING REMARKS

Photodissociation dynamics of the OH bond of phenol is examined in this article with the optimal UV laser pulse under the resonance condition. The laser pulse parameters are optimized with the aid of the genetic algorithm in an effort to maximize the cost functional. The cost functional is maximized in order to optimize the total dissociative flux and to minimize the laser pulse energy. Optimal control simulation is performed with three coupled electronic states and two nuclear degrees of freedom consisting of the OH stretching coordinate and the CCOH dihedral angle. The total outgoing dissociative flux is maximized in the optimization process and calculated in the S_0 and S_1 adiabatic asymptotic channels. The photodissociation process occurs through different mechanisms for different initial states. Under the optimal condition, the wave packet does not get sufficient energy to reach the S_2 asymptote and the dissociation entirely ($\sim$100%) takes place in the S_0 and S_1 asymptotic channels.

The optimal UV pulse excites the system predominantly to the $\pi\sigma^*$ state over the $\pi\pi^*$ state for the $|0,0\rangle$ and $|0,1\rangle$ initial states. Although excitation to the $\pi\sigma^*$ state is prefered for these initial states, it is not 100%. Although less favored some excitations occur to the $\pi\pi^*$ state. On the other hand, for the $|1,0\rangle$ and $|1,1\rangle$ initial states, the system is excited to both the $\pi\pi^*$ and $\pi\sigma^*$ states. The $\pi\sigma^*$ state gets the excited wave packet population in time through the intensity borrowing effect. The time accumulated flux in these channels (S_0 and S_1) varies for different initial state conditions. For the $|0,0\rangle$ initial state the S_1 adiabatic asymptotic channel gets slightly ($\sim$2%) more dissociative flux than the S_0 channel. Addition of one quantum of energy along the coupling coordinate in the initial state diffuses the time evolved wave function along the coupling coordinate on the $\pi\sigma^*$ state. Hence, the wave function preferentially follows the adiabatic path and leads to an increase in the dissociative flux in the S_1

channel. Therefore, the S_1 channel gets more flux (about 11%) as compared to the S_0 channel for the $|0,1\rangle$ initial condition. For the $|1,0\rangle$ and $|1,1\rangle$ initial states, the dissociation occurs in the S_1 channel preferentially over the S_0 channel as the high energy component of the wave packet dissociates through the S_1 channel. The diabatic coupling element between the $\pi\pi^*$ and $\pi\sigma^*$ states plays an important role to determine the symmetry of the wave function on the $\pi\sigma^*$ state. This coupling element is an odd function of the coupling coordinate, θ. Because of this coupling element, the nodal structure in the wave function develops on the $\pi\sigma^*$ state. In the presence of the optimal UV laser field the barrierless (via the $\pi\sigma^*$ state) photodissociation process is observed for the $|0,0\rangle$ and $|0,1\rangle$ initial states. On the other hand, both the barrierless and barrier-crossing (via the $\pi\pi^*$ state) mechanisms operate in the photodissociation of the $|1,0\rangle$ and $|1,1\rangle$ initial states. The photodissociation process (mechanism) in the optimal laser field is sensitive to the initial condition.

To this end, we note that in this study we have used the genetic algorithm as an optimization tool where the cost functional is treated as a fitness function. Various techniques such as gradient-based algorithms can be used to obtain an optimal laser pulse in the optimal control theory framework. In this theoretical scenario the first derivative of the cost functional with respect to different variables leads to coupled differential equations and gradient-based algorithms are used to solve these equations to generate an optimal electric field. On the other hand the genetic algorithm maximizes the cost functional and minimizes the laser intensity directly. In this study the genetic algorithm works well to converge the cost functional and the results appear to be experimentally feasible.

Chapter 6

Design of IR laser pulse for photodissociation of phenol using genetic algorithm

6.1 Introduction

Phenol is an important chromophore in many biological environments. Exploration of the photochemistry of phenol is important from an experimental as well as a theoretical point of view [207, 228]. Studies on the phenol-water and phenol-ammonia clusters are important to understand solvent chemistry and molecular biology. Electronic spectroscopy, vibrational spectroscopy, acid-base chemistry, binding energy and structure of the phenol-ammonia and phenol-water clusters have been studied theoretically as well as experimentally [208–217, 240, 241]. The ground state proton transfer reaction in the phenol-ammonia cluster studied with mid-IR spectroscopy [223] as well as with single-photon ionization spectroscopy [242]. The proton transfer reaction via excited states in the phenol-water and phenol-ammonia cluster has been observed both experimentally and theoretically [218, 221, 222, 227, 243–248]. The proton transfer reaction in the ground state [223, 242] and excited states [246–248] of phenol-ammonia cluster depends on the cluster size. The OH bond dissociation of phenol studied from the S_1 and S_2 states in an aqueous

medium [224, 225]. The photodissociation of the OH bond occurs at 248 nm in a molecular beam experiment [226] and the hydrogen atom was eliminated from the $\pi\sigma^*$ state. *Ab initio* calculations [130, 227, 229, 235] have been carried out extensively to study the hydrogen atom elimination from the $\pi\sigma^*$ state. In those studies, it is concluded that the $\pi\sigma^*$ state crosses the $\pi\pi^*$ state as well as the ground state [see Fig. (6.1)]. The $\pi\pi^*$ is the first excited state which results from an excitation from the highest occupied molecular orbital (HOMO) (π character) to the lowest unoccupied molecular orbital (LUMO) (π^* character) The $\pi\sigma^*$ state corresponds to excitation to the 3s orbital which is of Rydberg type.

Ab initio calculations viz., the complete active space self-consistent field (CASSCF) calculations have been carried out to construct the two-dimensional model which has three states and two nuclear degrees of freedom, and the time-dependent wave packet propagation was studied in absence of an electric field [130]. In the latter work, the initial state was prepared from different vibrational eigenfunctions of the ground electronic state. Those eigenstates are placed in the Frank-Condon (FC) region of the $\pi\pi^*$ state in the absence of an electric field (δ excitation). The conical intersections (CIs) among the S_1 and S_2 states give rise to a potential barrier of 0.6 eV. Because of the energetic reason the $|0,0\rangle$, $|0,1\rangle$ and $|0,2\rangle$ initial states do not cross over the barrier in the field-free condition. On the other hand, addition of a quantum of energy with reference to the OH stretching coordinate (equivalent to an IR excitation) results $|1,0\rangle$, $|1,1\rangle$ and $|1,2\rangle$ eigenfunctions which can cross over the potential barrier and dissociate. The wave packet (WP) shows some interesting symmetry properties and the CIs between the S_0-S_1 state drives the flux in a specific channel for the dissociation. These observations motivated us to perform the present laser induced-control study. In the previous investigation [201] the photodissociation is studied with UV laser pulses. Here, we investigate the photodissociation of

phenol with $|0,0\rangle$, $|0,1\rangle$ and $|0,2\rangle$ initial conditions employing IR laser pulses. Frequencies of laser pulses are considered in the IR region because of the energetic reason as one quantum energy with reference to the OH stretching coordinate makes the dissociation possible in field-free condition. Also, we are motivated to examine how an IR laser pulse modifies the nonadiabatic dynamics in the coupled potential energy surfaces (PESs) and drives dissociative flux along a particular channel.

Control of the dynamical behaviour of a quantum mechanical system by external laser light has been formulated within the mathematical framework of optimal control theory (OCT) [81, 155–157, 197, 198]. Control of the branching ratio of the photodissociated products of phenol was studied in the optimal control theory framework [230]. In this study, because of the CIs in the coupled states, the geometric phase gives rise an interesting effect on the nonadiabatic dynamics. The genetic algorithm together with optimal control theory [107] has been used to solve many control problems e.g., optimal control of photodissociation of phenol in presence of the UV laser pulse [201], control of photodissociation of pyrrole [202, 203], control of laser-driven isomerization of malonaldehyde [204], control of multiphoton dissociation [168, 170], control of laser-induced vibrational-rotational excitation [169] and control of molecular gate operations [205, 206]. In the present work, the optimal control of the photodissociation is studied with the model [130], involving three states and two nuclear degrees of freedom. An IR laser pulse is constructed with the aid of genetic algorithm in the optimal control theory framework. Total dissociative flux in the S_0 and S_1 channels is optimized in the optimization process.

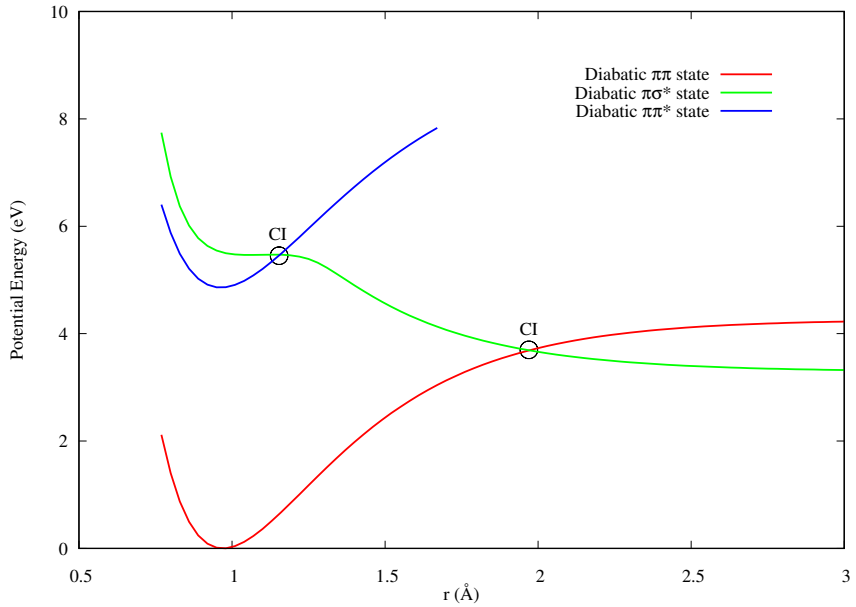

Figure 6.1: Diabatic ground electronic ($\pi\pi$) state (red), $\pi\sigma^*$ state (green) and $\pi\pi^*$ state (blue) of planar phenol molecule.

6.2 Theory and methodology

6.2.1 Quantum dynamics with an electric field

The multiphoton dissociation of the OH bond of phenol is studied in the lowest three electronic states i.e., the ground electronic state, $\pi\pi^*$ state and $\pi\sigma^*$ state including two nuclear degrees of freedom i.e., the OH stretching coordinate, r and CCOH dihedral angle, θ. The model Hamiltonian was developed [130] to study the photodissociation dynamics. The OH stretching mode is treated as the reaction coordinate and CCOH dihedral angle is defined as the coupling coordinate. The diabatic potential energy functions for the planar phenol molecule (θ=0) are presented in Fig. (6.1). The optimized equilibrium geometry of the phenol molecule of the ground electronic state occurs at r=0.96 Å. The ground electronic state and $\pi\pi^*$ state have analogous topography in the FC region. The CIs between the $\pi\sigma^*$ state and the $\pi\pi^*$ state and between the $\pi\sigma^*$ state and ground electronic state occur at 1.16 Å and 1.96 Å, respectively [see

Figs. (6.1) and (6.2)]. Two dimensional diabatic, adiabatic PESs and diabatic interstate coupling elements as a function of the reaction coordinate and the coupling coordinate are shown in Fig. (6.2). The eigenfunctions and eigenvalues of the ground electronic state are determined employing the pseudo-spectral method [178, 179, 249, 250]. The eigenfunctions are defined as $|n_r, n_\theta\rangle$ [see Fig. (6.3)] where n_r and n_θ are number of nodal lines along r and θ, respectively. The fundamental frequencies of the OH stretching coordinate and CCOH torsional coordinate obtained from the theoretical calculations are 3911 and 266 cm^{-1}, respectively. Experimental values of those frequencies are 3656 and 269 cm^{-1}, respectively [235, 236]. The theoretical frequencies are therefore in good accord with the experimental values. Note that the theoretical frequencies are harmonic whereas, the experimental ones are fundamental.

The electric field of a laser pulse interacts with the molecule and consequently, it modifies the molecular Hamiltonian. Within the semiclassical dipole approximation [87, 154], the molecular Hamiltonian of three states in a diabatic electronic basis reads

$$\hat{H} = \hat{H}_0 + \hat{H}_{int}, \tag{6.1}$$

where

$$\hat{H}_0 = \hat{T}_N \begin{pmatrix} 1 & 0 & 0 \\ 0 & 1 & 0 \\ 0 & 0 & 1 \end{pmatrix} + \begin{pmatrix} \hat{V}_{11} & \hat{V}_{12} & \hat{V}_{13} \\ \hat{V}_{21} & \hat{V}_{22} & \hat{V}_{23} \\ \hat{V}_{31} & \hat{V}_{32} & \hat{V}_{33} \end{pmatrix}, \tag{6.2}$$

and

$$\hat{H}_{int} = -\begin{pmatrix} 0 & 0 & \hat{\mu}_{13} \\ 0 & 0 & 0 \\ \hat{\mu}_{13} & 0 & 0 \end{pmatrix} \epsilon(t). \tag{6.3}$$

In the above equation, $\hat{H}$ is the molecular Hamiltonian in the presence of a laser field. $\hat{H}_0$ is the molecular Hamiltonian in the field-free condition and $\hat{H}_{int}$ is the laser-molecule interaction Hamiltonian. In the above equation, $\hat{T}_N$ is the nuclear kinetic energy operator. $\hat{V}_{ii}$ where i=1,2 and 3 are the diabatic PESs.

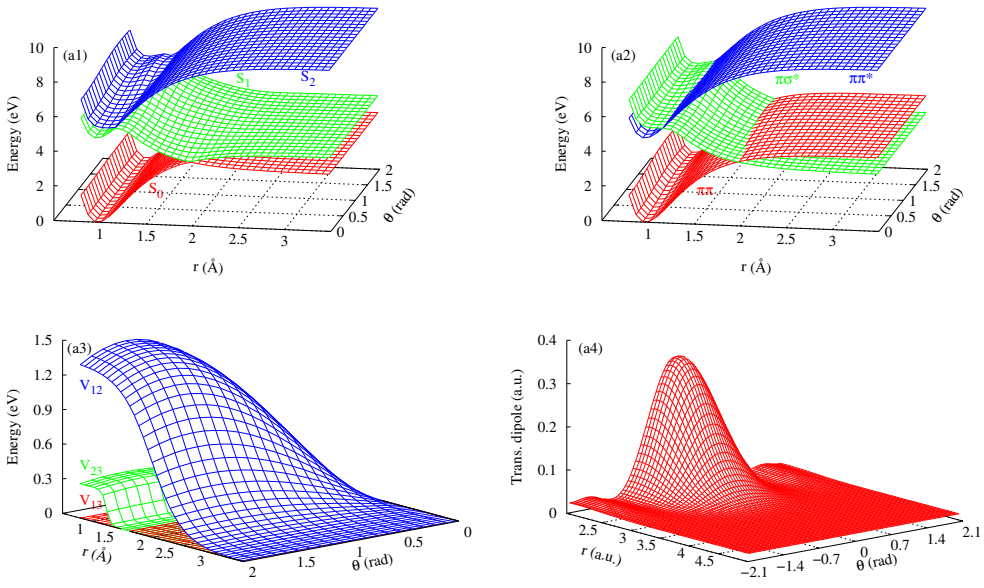

Figure 6.2: (a1) Adiabatic representation: the ground electronic (S_0) state (red), S_1 state (green) and S_2 state (blue). (a2) Diabatic representation: the ground electronic ($\pi\pi$) state (red), $\pi\sigma^*$ state (green) and $\pi\pi^*$ state (blue). (a3) Diabatic interstate coupling surfaces: V_{12} (blue), (V_{23}) (green), V_{13} (red). (a4) Diabatic TDM (red).

The off-diagonal elements are the interstate coupling elements i.e., $\hat{V}_{12}$ (coupling between the ground electronic ($\pi\pi$) state and $\pi\sigma^*$ state), $\hat{V}_{13}$ (coupling between the $\pi\sigma^*$ state and the $\pi\pi^*$ state) and $\hat{V}_{23}$ (coupling between the ground electronic ($\pi\pi$) state and $\pi\pi^*$ state). $\epsilon(t)$ is the time-dependent electric field of the laser pulse. In Eq. (6.3), $\hat{\mu}_{13}$ is the x component of the transition dipole moment (TDM) between the ground electronic state and $\pi\pi^*$ state. The kinetic energy operator ($\hat{T}_N$), PESs ($\hat{V}_{ii}$, i=1,2 and 3), the interstate coupling element ($\hat{V}_{12}$, $\hat{V}_{13}$ and $\hat{V}_{23}$) and TDM ($\hat{\mu}_{13}$) used in the present study are taken from Ref. [130].

The nuclear motion of the model system with a laser pulse is described by the time-dependent Schrödinger equation (TDSE)

$$i\hbar\frac{\partial}{\partial t}|\Psi(t)\rangle = \hat{H}|\Psi(t)\rangle. \tag{6.4}$$

The TDSE is solved numerically with the molecular Hamiltonian (discussed above) using the split-operator method (SO) [171, 200]. The fast Fourier transformation (FFT) method [172] is employed to calculate the operation of the kinetic energy. The WP is evolved [179, 237] on three-coupled PESs for a time duration of 2000 fs considering a time increment of 0.02 fs. The reaction coordinate (1.0 $a_0 \leq$ r $\leq$ 30.0 a_0) and the coupling coordinate ($-\pi \leq \theta \leq +\pi$) consists of 512 and 128 grid points, respectively. To avoid the reflection or wrap-around of the wave function at the grid edge, a sine-damping function [237] is employed along the reaction coordinate, r,

$$f(r_i) = \sin\left[\frac{\pi}{2}\frac{r_{mask} + \Delta r_{mask} - r_i}{\Delta r_{mask}}\right], \qquad r_i \geq r_{mask}, \tag{6.5}$$

that is activated at r_{mask}=26.0 a_0 and it decays smoothly from 1.0 to 0.0 over the interval Δr_{mask}=r_{max}-r_{mask} where r_{max} is the maximum value of r. The dissociation probability is estimated by evaluating the time-integrated flux on a

dividing surface located at $r = r_{flux}$ and it reads

$$P^D(t) = \frac{\hbar}{\mu} \int_{t=0}^{t} Im \left[\langle \Psi(r,\theta,t) | \frac{\partial \Psi(r,\theta,t)}{\partial r} \rangle \right] \Bigg|_{r=r_{flux}} dt, \tag{6.6}$$

where μ is the reduced mass of H and O. The time-dependent diabatic and adiabatic electronic populations [135] are calculated from the expectation values of the corresponding projection operators. These are defined as

$$P_i^d(t) = \langle \Psi(t) | \psi_i^d \rangle \langle \psi_i^d | \Psi(t) \rangle, \qquad i = 1, 2, 3, \tag{6.7}$$

$$P_i^a(t) = \langle \Psi(t) | \psi_i^a \rangle \langle \psi_i^a | \Psi(t) \rangle, \qquad i = 1, 2, 3. \tag{6.8}$$

6.2.2 Cost functional

The cost functional is constructed in the mathematical framework of the optimal control theory [81, 156, 157] with an aim to optimize an objective function with optimal values of laser field parameters. In the present study, the mathematical expression of the cost functional used in the genetic algorithm reads

$$J[\epsilon(t)] = J_o - \alpha_0 \int_0^T |\epsilon(t)|^2 dt. \tag{6.9}$$

In the above equation, J_0 is the objective function for the dissociation and it is calculated as a sum of the time-integrated outgoing flux on the S_0 and S_1 adiabatic channels. The time-integrated outgoing flux is calculated using Eq. (6.6) at time t=T where T is the total time duration for the nuclear dynamics. In the above equation, α_0 is the penalty factor that limits the laser field intensity. In the present study, α_0 is set to 0.0001.

6.2.3 Laser pulse parameterization employing the genetic algorithm

The initial guess laser field in the genetic algorithm is given by,

$$\epsilon(t) = \epsilon_0 \sin(\omega t) \cdot \mathrm{s}(t), \tag{6.10}$$

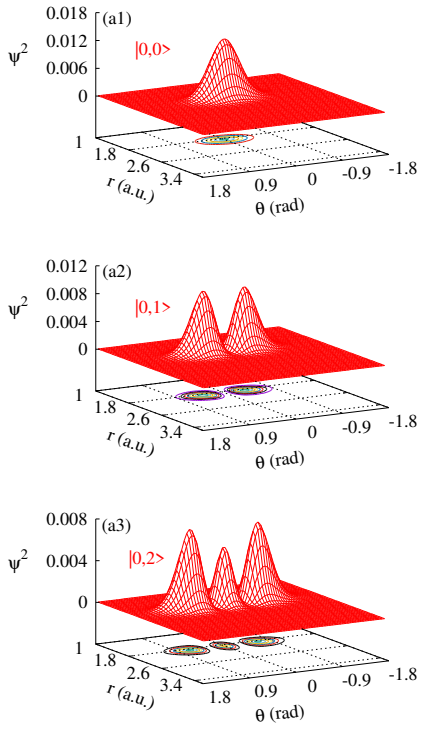

Figure 6.3: Vibrational wave functions of the ground electronic state of phenol as a function of the reaction coordinate, r and coupling coordinate, θ. These wave functions are defined as $|n_r, n_\theta\rangle$ where n_r and n_θ are the nodal lines along r and θ, respectively. (a1) $|0,0\rangle$ eigenfunction, (a2) $|0,1\rangle$ eigenfunction and (a3) $|0,2\rangle$ eigenfunction.

where, ω=ω_0 + ω_{range} and the quantity ω_0 depends on the initial state and ω_{range} varies from 0 to 1097 cm^{-1}. ω_0 for the $|0,0\rangle$, $|0,1\rangle$ and $|0,2\rangle$ initial conditions are 3911 cm^{-1} ($\omega_0^{00\rightarrow10}$, energy difference between the $|0,0\rangle$ and $|1,0\rangle$ levels), 3886 cm^{-1} ($\omega_0^{01\rightarrow11}$, energy difference between the $|0,1\rangle$ and $|1,1\rangle$ levels) and 3877 cm^{-1} ($\omega_0^{02\rightarrow12}$, energy difference between the $|0,2\rangle$ and $|1,2\rangle$ levels), respectively. In the above equation, ϵ_0 is the amplitude that varies from 0 to 0.60 a.u., and $s(t)$ is an envelope function that regulates the shape of the field. Here, $s(t)$ is given as

$$\mathrm{s}(t) = \begin{cases} \sin^2\left[\frac{\pi}{2}\left(\frac{t-t_0}{t_1-t_0}\right)\right] & \text{for} \quad t_0 \leq t \leq t_1, \\ 1 & \text{for} \quad t_1 \leq t \leq t_2, \\ \sin^2\left[\frac{\pi}{2}\left(\frac{t_3-t}{t_3-t_2}\right)\right] & \text{for} \quad t_2 \leq t \leq t_3 = T, \end{cases} \tag{6.11}$$

where t_0, t_1, t_2 and t_3 are time parameters. Here, t_0 is considered as 0 and t_3 as T (total time). t_0 to t_1 is the rising period and t_2 to t_3 is the turn-off period. The envelope function reaches a maximum value, i.e., 1 within the time duration between t_1 to t_2.

In the present study, amplitude (ϵ_0), frequency (ω) and two time parameters (t_1 and t_2) are optimized employing the genetic algorithm. The genetic algorithm is a global search optimization tool uses the idea of the principles of genetics like reproduction, selection, crossover, mutation, etc. In the algorithm, each parameter of the laser pulse is stored in a binary number carrying ten bits (0 or 1). A chromosome defines a laser pulse in the algorithm, and it is composed of four parameters i.e., a total of 40 bits. The parameter values are varied within the range defined earlier. A population considered in the genetic algorithm corresponds to 10 individuals. The individuals are the candidate solutions for the laser pulse. The algorithm starts the calculation with an initial guess population. The individuals in this population are selected randomly from the parameter space. The cost functional value is calculated with the help of the initial population. The resulting cost functional value determines the fitness of

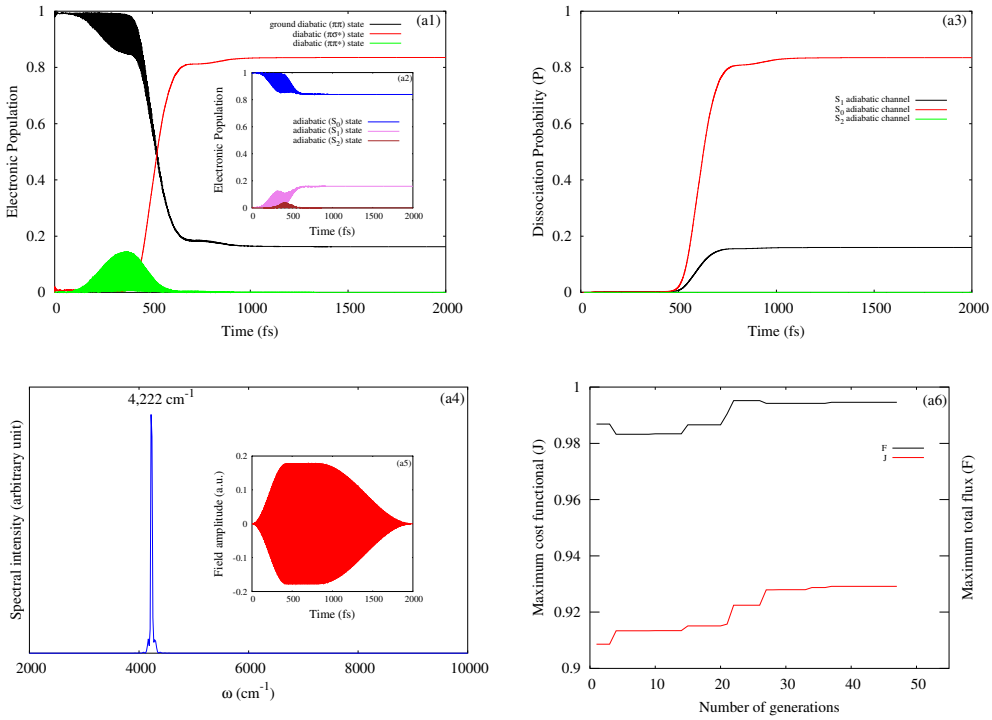

Figure 6.4: (a1) Time-dependent diabatic electronic population probabilities of the ground ($\pi\pi$) state (black), $\pi\sigma^*$ state (red) and $\pi\pi^*$ state (green); (a2) Time-dependent adiabatic electronic population of the S_0 (blue), S_1 (violet) and S_2 state (brown); (a3) Time-accumulated dissociative flux at the S_0 (red), S_1 (black) and S_2 (green) adiabatic channels; (a4) Frequency spectrum (blue) and (a5) temporal structure (red) of the optimal laser pulse; (a6) Variation of the total dissociative flux (black) and the cost functional (red) in the genetic algorithm. These results are obtained with the $|0,0\rangle$ initial state.

an individual (a set of parameters). For the dissociation, the cost functional value closer to 1.0 corresponds to the individual (a chromosome i.e., a set of parameters) to be fit for survival. The population goes through different genetic operations like selection, elitism, crossover, etc. as suggested in Refs. [169, 201]. These events generate a new population repeatedly until the cost functional fulfils the convergence criteria. In this study, the cost functional shows good convergence behaviour, and it is optimized within 20-50 generations [see Figs. 6.4(a6), 6.6(a6) and 6.8(a6)]

6.3 Results and discussion

Optimal calculations are performed with different initial states which are prepared from the vibrational levels ($|0,0\rangle$, $|0,1\rangle$ and $|0,2\rangle$). The initial state is excited in the multiphoton excitation fashion to the $\pi\pi^*$ state in the presence of the optimal IR laser pulse.

6.3.1 Photodissociation of the $|0,0\rangle$ vibrational level

The initial state wave function is prepared from the $|0,0\rangle$ vibrational level of the ground electronic state. The optimal IR laser pulse is constructed with the genetic algorithm. The optimal IR laser pulse excites the initial state (i.e., $|0,0\rangle$) to the $\pi\pi^*$ state. The excited WP of the $\pi\pi^*$ state has adequate energy to overcome the potential barrier and dissociates predominantly on the S_0 adiabatic channel as can be seen from Fig. (6.4). The central frequency of the optimal IR laser pulse, 4,222 cm^{-1} [see Fig. 6.5(a4)] is calculated using the frequency spectrum. Because of the S_1-S_2 CI, there is a potential barrier as high as 0.6 eV (with reference to the minimum of the $\pi\pi^*$ state) along the reaction coordinate. In field-free condition, the initial states are prepared in the FC region of the $\pi\pi^*$ state (δ excitation) [130]. As the $|0,0\rangle$ initial state has 2,202 cm^{-1} energy which is lower than the potential barrier, hardly any dissociation takes place in the field-free condition.

The optimal IR laser pulse excites the system from the ground electronic state to the $\pi\pi^*$ state, and the system dissociates in the lower two channels [see Fig. (6.4)]. The photodissociation mechanism is understood with the help of time-dependent electronic population probabilities, the time-accumulated fluxes and the snapshots of the probability densities of the WP. A series of events take place in the field-driven photodissociation dynamics. The optimal IR laser pulse interacts with the initial state and a little fraction of the latter

is excited to the $\pi\pi^*$ state in the multiphoton fashion. The dump component of the pulse de-excites the WP population (a small portion) of the $\pi\pi^*$ state onto vibrationally excited levels of the ground electronic state. The laser field induces the pump-dump events which continue till 600 fs (approximately). Because of these events, the WP becomes vibrationally hot with reference to the reaction coordinate both on the ground state and $\pi\pi^*$ state [see Fig. (6.5)]. The vibrationally hot WPs develop nodal lines along the OH stretching coordinate. The dumped WP interferes with the WP population on the ground state. Similarly, the pumped WP interferes with the WP population on the $\pi\pi^*$ state. The WP population on the $\pi\pi^*$ state reaches a maximum at 372 fs. A small portion of the WP population of the $\pi\pi^*$ state goes to the $\pi\sigma^*$ state in the FC region because of the non-vanishing interstate diabatic coupling element. This small population moves on with time to both the attractive well of the $\pi\pi^*$ state and the repulsive region of the $\pi\sigma^*$ state. The earlier part of the WP population interferes with the WP population on the $\pi\pi^*$ state.

The vibrationally hot WP on the $\pi\pi^*$ state has higher energy than the barrier and easily crosses over the potential barrier and moves rapidly on the repulsive region of the $\pi\sigma^*$ state. The WP dissociates at the S_0 and S_1 channels in 480 fs. Mostly, the WP population on the $\pi\sigma^*$ state evolves in a localized way (around the θ=0) and prefers to follow the diabatic path. A small portion of the WP population becomes diffused along the coupling coordinate and prefers the adiabatic path. Therefore, the WP population of the $\pi\sigma^*$ state correlates to the S_0 adiabatic channel (about 84% of the population) predominantly over S_1 channel (about 16% of the population). Hence, the laser field-induced dissociation preferentially takes place in the S_0 adiabatic channel for the $|0,0\rangle$ initial state. It is noted from Table (6.1) that more than 99% dissociation takes place through the S_0 and S_1 channels. With this initial state, the cost functional

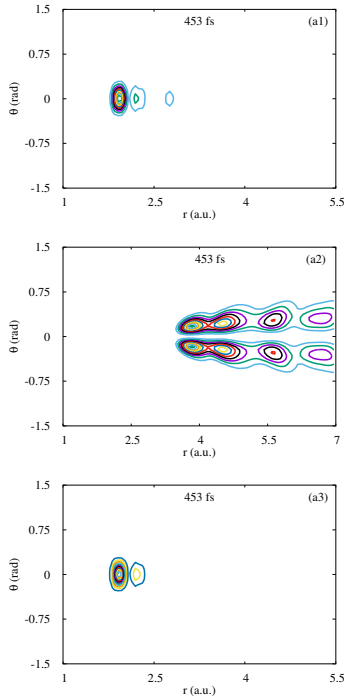

Figure 6.5: Snapshots of the WP probability density as a function of the OH stretching coordinate (r) and coupling coordinate (θ): (a1) probability density on the diabatic ground electronic state at 453 fs, (a2) probability density on the diabatic $\pi\sigma^*$ state at 453 fs and (a3) probability density on the diabatic $\pi\pi^*$ state at 453 fs of the $|0,0\rangle$ initial state.

acquires the convergence at 47 generations in the genetic algorithm [see Fig. 6.4(a6)].

The FC zone, CIs are located in the $\theta = 0$ region (planar geometry of the phenol molecule) of the PESs. The WP shows a few interesting symmetry properties. The WP of the ground electronic state is symmetric with respect to the coupling coordinate at time, t=0 [see Fig. (6.5)]. The $\pi\pi^*$ state gets population from the initial state via the pump-dump mechanism. Therefore, the WP of this state shows the symmetry property like the ground electronic state. As the time progress multiple nodal lines appear along the reaction coordinate in the WP probability density both on the ground electronic state and $\pi\pi^*$ state. The WP of the ground state and $\pi\pi^*$ state are even functions with reference to the coupling coordinate [see Figs. 6.5(a1) and 6.5(a3)]. The diabatic interstate coupling element between the $\pi\sigma^*$-$\pi\pi^*$ is an odd function of the coupling coordinate, θ [130]. The WP of the $\pi\sigma^*$ state has a nodal line along $\theta = 0$ i.e., anti-symmetric with respect to the coupling coordinate because of the diabatic coupling. This nodal line results from the geometric phase effect. In the adiabatic representation, the WP components move with an opposite phase around the S_1-S_2 CI and interfere destructively leading to a nodal line at $\theta = 0$ [see Fig. 6.5(a2)].

6.3.2 Photodissociation of the $|0,1\rangle$ vibrational level

In this section, we discuss the laser pulse-induced photodissociation of the $|0,1\rangle$ vibrational level. The central frequency, i.e., 4422 cm^{-1} is determined from the frequency spectrum [see Fig. 6.6(a4)]. In the field-free condition, the photodissociation hardly (less than 5%) takes place because the $|0,1\rangle$ vibrational level has lower energy as compared to the height of the potential barrier [130]. It can be seen from Fig. (6.6) that the optimal IR laser pulse excites the initial

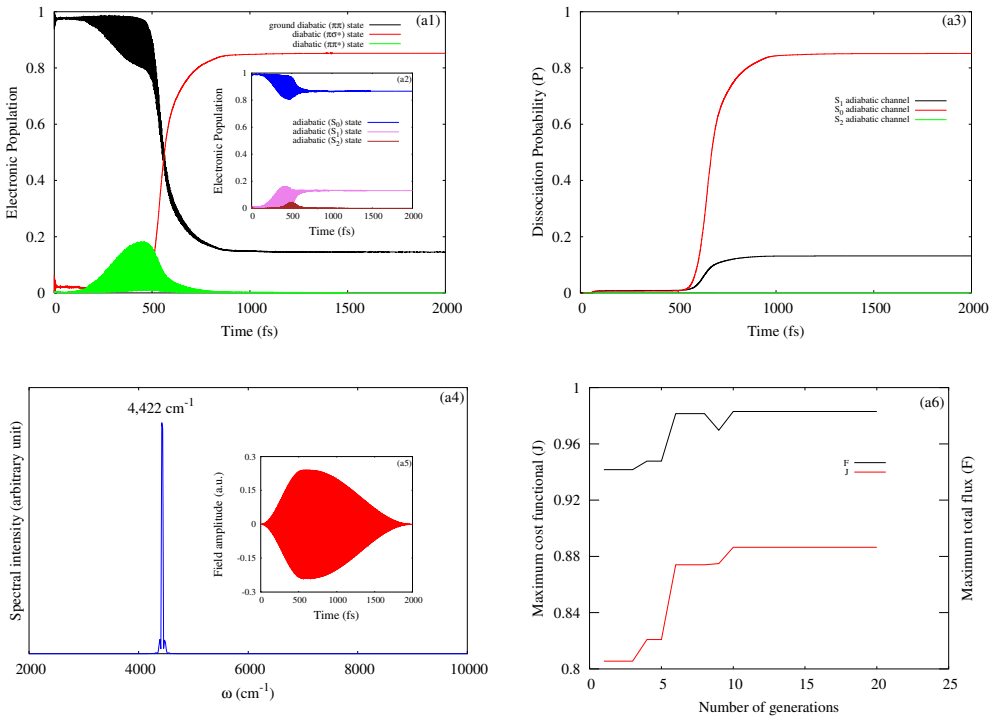

Figure 6.6: (a1) Time-dependent diabatic electronic population probabilities of the ground ($\pi\pi$) state (black), $\pi\sigma^*$ state (red) and $\pi\pi^*$ state (green); (a2) Time-dependent adiabatic electronic population of the S_0 (blue), S_1 (violet) and S_2 state (brown); (a3) Time-accumulated dissociative flux at the S_0 (red), S_1 (black) and S_2 (green) adiabatic channels; (a4) Frequency spectrum (blue) and (a5) temporal structure (red) of the optimal laser pulse; (a6) Variation of the total dissociative flux (black) and the cost functional (red) in the genetic algorithm. These results are obtained with the $|0,1\rangle$ initial state.

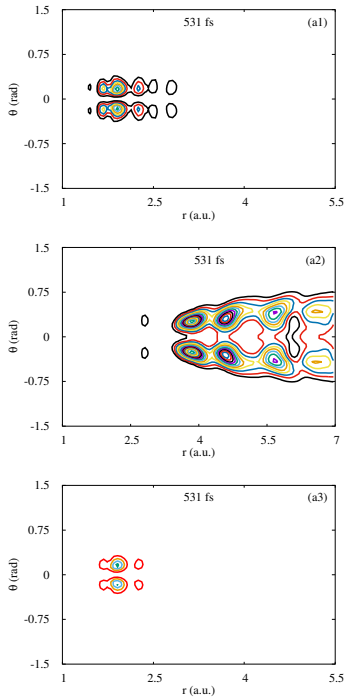

Figure 6.7: Snapshots of the WP probability density as a function of the OH stretching coordinate (r) and coupling coordinate (θ): (a1) probability density on the diabatic ground electronic state at 531 fs, (a2) probability density on the diabatic $\pi\sigma^*$ state at 531 fs and (a3) probability density on the diabatic $\pi\pi^*$ state at 531 fs of the $|0,1\rangle$ initial state.

state, and the dissociation takes place in the S_0 and S_1 adiabatic channels. The multiphoton excitation of the initial state happens to the $\pi\pi^*$ state in the presence of the optimal IR laser pulse. The excited population on the $\pi\pi^*$ state is dumped back to the upper vibrational levels of the ground electronic state. Because of the pump-dump events, the WP becomes vibrationally excited both on the ground electronic state and $\pi\pi^*$ state. The excitation process takes place through the pump-dump events in a similar way as for the $|0,0\rangle$ initial state. The pump-dump events continue till 800 fs (approximately). The excited WP population on the $\pi\pi^*$ state increases with time and reaches a maximum at 446 fs. The WP on the $\pi\pi^*$ state is vibrationally excited with respect to the OH stretching mode.

Initial state	J	Dissociation	ϵ_{max}
$\|0,0\rangle$	0.929145	0.994570	0.178299
$\|0,1\rangle$	0.886508	0.982989	0.241054
$\|0,2\rangle$	0.850502	0.979883	0.278592

Table 6.1: The photodissociation in the presence of the optimal IR laser pulse of time duration 2000 fs with different vibrational levels (i.e., $|0,0\rangle$, $|0,1\rangle$ and $|0,2\rangle$) as an initial state has been performed for $\alpha_0 = 0.0001$. In the table, the dissociation denotes the flux, ϵ_{max} refers to maximum amplitude of the optimized laser pulse, and J is the value of the cost functional. All parameters are in a.u..

Because of the energetic reason, it crosses over the barrier. The WP moves rapidly on the $\pi\sigma^*$ state. The WP starts dissociating through both the S_0 and S_1 channels approximately at 550 fs. The WP follows a localized motion and prefers the diabatic path for the dissociation. It can be seen from Figs. 6.6(a1), 6.6(a2) and 6.6(a3) that the S_0 and S_1 adiabatic channels get about 85% and 15% of population probabilities, respectively. In this case the cost functional convergences at 20 generations in the genetic algorithm [see Fig. 6.6(a6)].

As the ground state and $\pi\pi^*$ state are connected in the pump-dump events, both the WPs show similar symmetry properties. The WPs of the ground electronic state and $\pi\pi^*$ state are odd functions with reference to the coupling mode. The WP of the $\pi\sigma^*$ state is an even function with respect to the coupling coordinate because of the diabatic coupling element between the $\pi\pi^*$ state and $\pi\sigma^*$ state.

6.3.3 Photodissociation of the $|0,2\rangle$ vibrational level

Here, we discuss the photodissociation of the $|0,2\rangle$ initial state [see Fig. (6.8)]. The central frequency, 4355 cm^{-1} is extracted from the frequency profile of the optimal laser pulse. It is observed that the $|0,2\rangle$ vibrational level could not dissociate because of the energy barrier in the field-free condition [130]. The multiphoton excitation of the initial state is taken place to the $\pi\pi^*$ state. The

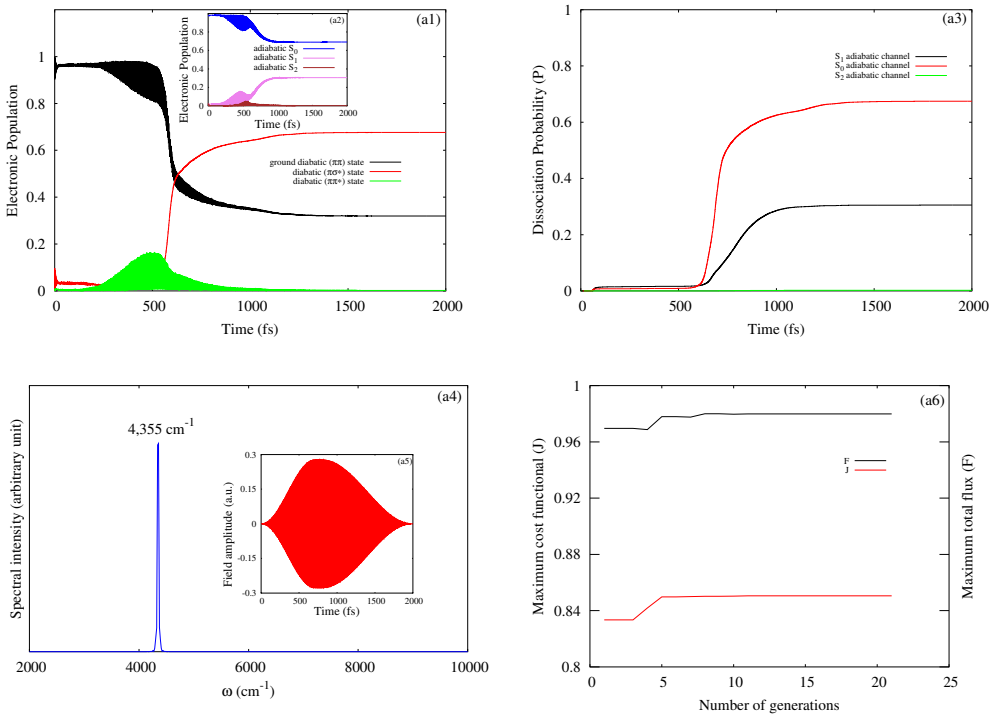

Figure 6.8: (a1) Time-dependent diabatic electronic population probabilities of the ground ($\pi\pi$) state (black), $\pi\sigma^*$ state (red) and $\pi\pi^*$ state (green); (a2) Time-dependent adiabatic electronic population of the S_0 (blue), S_1 (violet) and S_2 state (brown); (a3) Time-accumulated dissociative flux at the S_0 (red), S_1 (black) and S_2 (green) adiabatic channels; (a4) Frequency spectrum (blue) and (a5) temporal structure (red) of the optimal laser pulse; (a6) Variation of the total dissociative flux (black) and the cost functional (red) in the genetic algorithm. These results are obtained with the $|0,2\rangle$ initial state.

$|0,2\rangle$ initial state undergoes dissociation through the mechanism discussed earlier for the $|0,0\rangle$ and $|0,1\rangle$ initial states. The pump component of the optimal IR laser pulse excites the initial state to the $\pi\pi^*$ state. The WP population of the $\pi\pi^*$ state is de-excited to the ground electronic state in subsequent times because of the dumping component of the control pulse. These pump-dump events repeat till 1000 fs (approximately). The WP on the ground electronic state as well as on the $\pi\pi^*$ state becomes vibrationally hot along the reaction coordinate. The $\pi\pi^*$ state gets the WP population through the excitation process and reaches a maximum at 489 fs. The WP on the $\pi\pi^*$ state crosses the barrier and it is propagated rapidly on the $\pi\sigma^*$ state. It is clear from Fig. 6.8(a3) that the dissociation on both the channels begins approximately at 600 fs. The WP preferentially follows the diabatic path because of its localized motion and dissociates dominantly in the S_0 channel. The dissociation of 68% and 31% of the WP population takes place at the S_0 and S_1 channels, respectively [see Fig. 6.8(a3)]. For the $|0,2\rangle$ initial condition, the cost functional converges at 21 generations in the genetic algorithm [see Fig. 6.8(a6)].

Similar to the $|0,0\rangle$ and $|0,1\rangle$, the $|0,2\rangle$ initial state condition also shows different symmetry properties of the WPs of different states. The multiphoton pump-dump events create a vibrationally hot WP both on the ground electronic state and $\pi\pi^*$ state. Therefore, the WPs of these states are symmetric with reference to the coupling coordinate [see Figs. 6.9(a1) and 6.9(a3)]. The diabatic coupling element determines the symmetry property of the WP of the $\pi\sigma^*$ state. The WP of the $\pi\sigma^*$ state is an odd function with respect to the coupling coordinate. A nodal line [see Fig. 6.9(a2)] appears in the WP probability density (along θ=0) because of the geometric phase effect.

The optimal IR laser pulses for all the initial conditions discussed above

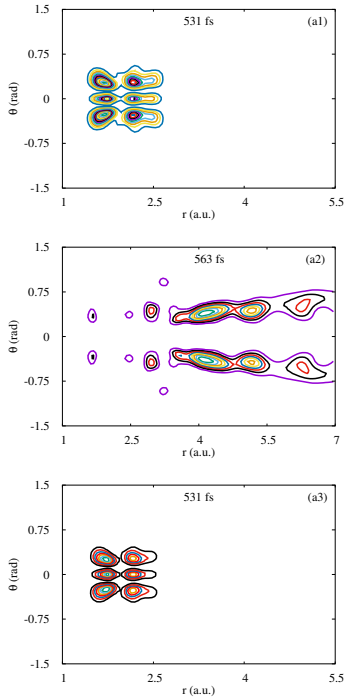

Figure 6.9: Snapshots of the WP probability density as a function of the OH stretching coordinate (r) and coupling coordinate (θ): (a1) probability density on the diabatic ground electronic state at 531 fs, (a2) probability density on the diabatic $\pi\sigma^*$ state at 563 fs and (a3) probability density on the diabatic $\pi\pi^*$ state at 531 fs of the $|0,2\rangle$ initial state.

have a smooth temporal profile. Maximum amplitudes (ϵ_{max}) of these strong optimal pulses range between 0.17-0.28 a.u. [see Table (6.1)]. The dissociation in a particular channel e.g., S_0 and S_1 depends on the initial state. The time-accumulated fluxes calculated at the adiabatic asymptotic channels are varied for different initial states. Addition of a quantum of energy along the coupling mode to the initial state diffuses the WP with reference to the coupling coordinate. The diffused components of the WP follow the adiabatic path and dissociate in the S_1 adiabatic channel. On the other hand, the WP components move in a localized fashion around the θ=0 line and dissociate favourably in the S_0 adiabatic channel. Considering the $|0,0\rangle$, $|0,1\rangle$ and $|0,2\rangle$ initial state it can be seen from Figs. 6.4(a1), 6.4(a2) and 6.4(a3), 6.6(a1), 6.6(a2), 6.6(a3), 6.8(a1), 6.8(a2) and 6.8(a3) that the S_1 channel gets a lower dissociation probability for the $|0,1\rangle$ initial state than the $|0,0\rangle$ and $|0,2\rangle$ initial states. Therefore, the "odd-even" effect is observed for the dissociation of these initial states. This effect was reported in the field-free condition [130] and in the presence of the optimal UV laser pulse [201]. A similar effect was reported by Baer *et al.* in the quasi-Jahn-Teller system [239].

6.4 Summarizing remarks

The multiphoton photodissociation of the OH bond of phenol has been performed employing the optimally designed strong IR laser pulses. The vibrational eigenfunctions of the ground electronic state viz., $|0,0\rangle$, $|0,1\rangle$ and $|0,2\rangle$ are considered as initial states for the optimal calculations. These eigenfunctions have lower energy as compared to the potential barrier present on the $\pi\pi^*$ state. These vibrational eigenfunctions hardly dissociate in the field free condition [130] because of the potential barrier. The multiphoton pump-dump events are repeatedly operational in the field-induced condition. Consequently, the WP population becomes vibrationally hot both on the ground electronic state and

$\pi\pi^*$ state. Hence, the WP crosses the potential barrier, and the $\pi\sigma^*$ state mediated photodissociation is observed. The dissociation of the WP takes place almost entirely (more than 99%) on the lower two adiabatic channels. In all three conditions, the WP evolves in a localized fashion around θ=0 line and dissociates preferentially to the S_0 channel. Hence, the S_0 channel gets higher time-accumulated flux as compared to the S_1 channel. Addition of a quantum energy of the coupling mode to the initial state makes the time-evolved WP diffuse along the coupling coordinate. The diffused WP population follows the adiabatic path and enhances the dissociation probability at the S_1 adiabatic asymptotic channel. The S_1 adiabatic channel gets slightly lower dissociative flux for the $|0,1\rangle$ initial state than the $|0,0\rangle$ and $|0,2\rangle$ initial states. Therefore, the "odd-even" effect [130, 201, 239] is observed in this multiphoton photodissociation. Overall, the dissociation in a particular channel is sensitive to an initial state. The WPs show some interesting symmetry properties. The symmetry of the WPs of the ground electronic state and $\pi\pi^*$ state are the same as they involved in the pump-dump events. The symmetry of the WP of the $\pi\sigma^*$ state is decided by the diabatic $\pi\pi^*$-$\pi\sigma^*$ coupling element. The genetic algorithm converges the cost functional within 25-60 generations, and the latter shows good optimization behaviour for the multiphoton dissociation. This control work is useful for the photodissociation reaction which has a potential barrier in the excited state.

Chapter 7

Summary and outlook

In this thesis, IR and UV optimal laser pulses are constructed theoretically for various molecular processes viz., selective vibrational population transfer, tautomerization and photodissociation. These molecular processes are studied in the polyatomic systems. The optimal laser pulses are constructed in optimal control theory. The cost functional is set up to optimize an objective of a molecular process via manipulation of the nuclear dynamics. The cost functional is composed of an objective (a desired outcome), the fluence term related to the laser pulse intensity and the time-dependent Schrödinger equation (TDSE) as a dynamical constraint (as these systems follow the TDSE). The objective is optimized and the penalty term (laser field intensity) is minimized in the process of optimization to maximize the cost functional. Finally, the cost functional is converged and the optimal laser pulse is obtained for a molecular process. The quantum dynamics of these processes is studied within the adiabatic and diabatic (nonadiabatic dynamics of coupled electronic states) representations. The laser-molecular interaction is treated within the semiclassical dipole approximation. The split operator method combined with the fast Fourier transformation (FFT) algorithm is used to carry out the time evolution of the laser field-driven molecular processes.

Selective preparations of various vibrational states of the ground electronic state of the 4(3H)-pyrimidinone/4-hydroxypyrimidine system are performed with optimal laser pulses. The ground electronic state along the OH bond distance is calculated using the Coulpled Cluster Singles and Doubles (CCSD) method with an aug-cc-pVDZ basis set and the dipole moment is calculated from the complete-active-space self-consistent-field (CASSCF) method using the Molpro package. The ground electronic state has a potential barrier as high as 180 kJ/mol between two tautomers. Optimal laser pulses are designed employing the conjugate gradient method. These optimal pulses are constructed in different timescales of 30000, 60000 and 90000 a.u. with the penalty factor (α_0) values of 0.1 and 0.01. The effect of variation of the pulse duration as well as the penalty factor on the population probability and structure of the laser pulse (both temporal and frequency) are examined.

We observed that field amplitudes of the optimal laser pulses decrease with a higher time duration with an agreement of the pulse area theorem. In frequency spectra, besides the sharp peak which is responsible for the considered transition, there are secondary peaks appear because of the involvement of intermediate vibrational states. Lower numbers of intermediate states are involved for an increased time duration. As a result, a small number of secondary peaks appear in frequency spectra. We observed that the population transfer becomes more efficient for a transition for higher time durations. Nevertheless, at the final time, almost 100% population reaches the target vibrational state. A higher penalty factor results a reduction in the amplitude of the optimal laser pulse for a particular vibrational excitation. Similarly, the transition probability and cost functional are lowered with a rise of the penalty factor. A strong field laser pulse is obtained for the vibrational transition from 4(3H)-pyrimidinone (opmd) v=0 to 4-hydroxypyrimidine (hpmd) v=0. We observed that various intermediate

vibrational states are involved in the optimal condition. A delocalized state participates dominantly in the population transfer process as compared to other intermediate states. In the optimization process, the cost functional reaches near the convergence limit within a few iterations. In the present work, the conjugate gradient method works well to design laser pulses for various vibrational transitions.

The $\pi\pi^*$ state-mediated tautomerization is controlled through the pump-dump mechanism in the 4(3H)-pyrimidinone/4-hydroxypyrimidine system. The intramolecular hydrogen transfer reaction takes place in the photo-induced tautomerization. Various parameters of laser pulses are optimized using the genetic algorithm. The model system contains two electronic states i.e., the ground electronic state and $\pi\pi^*$ state. The potential energy functions of these states along the OH stretching coordinate are calculated using the equation-of-motion coupled cluster singles and doubles (EOM-CCSD) method with an aug-cc-pVDZ basis set using the Molpro package. Potential barriers are present between the tautomers in both potential energy surfaces. An initial wave packet (WP) is prepared by placing a Gaussian WP in the reactant region. The optimal calculations are carried out with the *ab initio* calculated and constant transition dipole moments.

The results of this study show that a pair of UV laser pulses perform the $\pi\pi^*$ state-mediated tautomerization. The optimal UV laser pulses (pump and dump) are designed in the genetic algorithm. The pump laser pulse excites the initial WP to the $\pi\pi^*$ state. The excited WP freely evolves and crosses over the barrier on the $\pi\pi^*$ state. When the WP reaches the product configuration on the $\pi\pi^*$ state, the dump pulse is activated and it dumps the WP back to the ground electronic state. In this study, the genetic algorithm works well to optimize

laser pulse parameters to induce the $\pi\pi^*$ state-mediated tautomerization. The constant dipole moment condition shows slightly better population transfer as compared to the *ab initio* calculated transition dipole moment condition.

The photodissociation of the OH bond of phenol is optimally controlled in the presence of the UV laser pulse. In this study, the laser pulse parameters are optimized using the genetic algorithm in an effort to maximize the cost functional. The photodissociation dynamics is carried out on the three lowest electronic states i.e., the ground electronic state, $\pi\pi^*$ state and $\pi\sigma^*$ state including two nuclear degrees of freedom i.e., the OH stretching coordinate and CCOH dihedral angle. These electronic states are coupled through conical intersections. Vibrational wave functions (defined by, $|n_r, n_\theta\rangle$, where n_r and n_θ denote the number of nodes along the reaction coordinate and coupling coordinate, respectively) of the ground electronic state are calculated using the spectral quantization method. An initial state is prepared from vibrational wave functions ($|0,0\rangle$, $|0,1\rangle$, $|1,0\rangle$ and $|1,1\rangle$) on the ground electronic state. The nonadiabatic nuclear dynamics on the coupled electronic states is performed in the diabatic representation. The total outgoing dissociative flux is maximized in the optimization process, calculated in the S_0 and S_1 adiabatic asymptotic channels.

The result shows that the photodissociation process takes place through different mechanisms for different initial states. The optimal UV pulse excites the initial state population predominantly to the $\pi\sigma^*$ state over the $\pi\pi^*$ state for the $|0,0\rangle$ and $|0,1\rangle$ initial conditions. The excitation to the $\pi\sigma^*$ state is favoured for these initial states though it is not 100%. In these conditions, a small WP population of the initial state is excited to the $\pi\pi^*$ state. On contrary, the system is excited to both the $\pi\pi^*$ and $\pi\sigma^*$ states for the $|1,0\rangle$ and $|1,1\rangle$ initial states.

In both excitations, the $\pi\sigma^*$ state gets the excited WP population through the intensity borrowing effect. The time accumulated flux in S_0 and S_1 channels varies for different initial states. For the $|0,0\rangle$ initial state S_1 adiabatic asymptotic channel gets slightly ($\sim$2%) more dissociative flux than the S_0 channel. The addition of one quantum of energy along the coupling coordinate in the initial state i.e., $|0,1\rangle$ diffuses the time-evolved wave function along the coupling coordinate on the $\pi\sigma^*$ state. Hence, the WP population preferentially follows the adiabatic path and leads to an increase of the dissociative flux in the S_1 channel. Therefore, the S_1 channel gets more outgoing flux (about 11%) as compared to the S_0 channel for the $|0,1\rangle$ initial state. For the $|1,0\rangle$ and $|1,1\rangle$ initial states, the dissociation occurs in the S_1 channel preferentially over the S_0 channel as high energy components of the WP dissociate through the S_1 channel. In this study, the diabatic coupling element between the $\pi\pi^*$ and $\pi\sigma^*$ states determines the symmetry of the wave function on the $\pi\sigma^*$ state. The nodal line in the wave function appears on the $\pi\sigma^*$ state as the coupling element is an odd function of the coupling coordinate, θ. However, in the presence of the optimal UV laser pulse, the WP does not get sufficient energy to reach the S_2 asymptote and the dissociation entirely ($\sim$100%) takes place in the S_0 and S_1 asymptotic channels. It is observed that the $|0,0\rangle$ and $|0,1\rangle$ initial states dissociate via the $\pi\sigma^*$ state through the barrierless mechanism. On the other hand, both the barrierless and barrier-crossing mechanisms via the $\pi\pi^*$ state take place for the $|1,0\rangle$ and $|1,1\rangle$ initial states. In this study, the result shows that the photodissociation mechanism in the presence of the optimal laser field is sensitive to an initial state.

The photodissociation of the OH bond of phenol has been further extended in the presence of the optimal IR laser pulse. The vibrational eigen functions viz., $|0,0\rangle$, $|0,1\rangle$ and $|0,2\rangle$ are considered initial states for the optimal calculations. These eigenfunctions have lower energy as compared to the potential barrier

present along the OH stretching coordinate on the $\pi\pi^*$ state. These vibrational eigenfunctions hardly dissociate in the field-free condition because of the potential barrier. Optimal laser pulses for the photodissociation of these eigenfunctions are designed using the genetic algorithm.

Our result shows that an alternative photodissociation mechanism is observed in the presence of the optimal IR laser pulse. The optimal laser pulse excites a small portion of the WP population of the initial state to the $\pi\pi^*$ state. The excited WP population is dumped back onto vibrationally excited levels of the ground electronic state. The excitation (pump) and de-excitation (dump) are the multiphoton processes. The multiphoton pump-dump events are taken place repeatedly in the field-induced condition. Consequently, the WP population becomes vibrationally hot on the ground electronic state as well as on the $\pi\pi^*$ state. As the WP becomes vibrationally hot it crosses the potential barrier and $\pi\sigma^*$ mediated photodissociation is observed. The laser field-induced dissociation takes place almost entirely (more than 99%) on the lower two adiabatic channels. In all three conditions, the WP moves in a localized fashion around the θ=0 line and dissociates favourably to the S_0 channel. Therefore, the S_0 channel gets higher time-accumulated outgoing flux as compared to the S_1 channel. The time-evolved WP is diffused along the coupling coordinate while adding one quantum of energy of the coupling mode to the initial state. The diffused WP population prefers the adiabatic path on the PESs and increases the dissociation probability at the S_1 adiabatic asymptotic channel. The S_1 adiabatic channel gets slightly lower dissociative flux for the $|0,1\rangle$ initial state than the $|0,0\rangle$ and $|0,2\rangle$ initial states. Therefore, in this study, the "odd-even" effect is observed. Overall, the dissociation in a particular channel depends on an initial state. The symmetry of the WP of the ground electronic state and $\pi\pi^*$ state are the same as these states are involved in the pump-dump events. The symmetry of the

WP of the $\pi\sigma^*$ state is determined by the diabatic $\pi\pi^*$-$\pi\sigma^*$ coupling element. The genetic algorithm shows good optimization behaviour for the convergence of the cost functional. This control work is useful for the excited state-mediated hydrogen transfer reaction which has a potential barrier in the excited state.

Future directions

- In the 4(3H)-pyrimidinone/4-hydroxypyrimidine system, one can extend further the control work by including several excited states e.g., the $\pi\pi^*$, $\pi\sigma^*$ and $n\pi^*$ states with the ground electronic state along one or more coupling modes. For this, first one need to find suitable coupling modes and then one can calculate potential energy surfaces along these coordinates.

- The control work of the photodissociation of phenol can be further extended by adding one or two coupling modes to the model system. First, one needs to select these additional modes and perform *ab initio* calculations to get potential energy surfaces.

- To perform control work in a more realistic way, one needs to construct model systems by including multi-states and multi-modes. In those cases, first one needs to calculate potential energy surfaces along multiple modes. The control work can be performed with the OCT-MCTDH package that can handle a multi-states and multi-modes problems.

Appendix A

Derivation of pulse design equations

Rabitz and co-workers developed the cost functional is given as (here we drop the bold form notation (vector aspects) of the electric field, ϵ and the dipole moment, μ for simplicity),

$$J[\epsilon(t)] = \langle\psi(T)|\hat{O}|\psi(T)\rangle - \alpha_o \int_0^T [\epsilon(t)]^2 dt - 2Re\left[\int_0^T \langle\chi(t)\left|\frac{\partial}{\partial t} + i\hat{H}\right|\psi(t)\rangle dt\right] \quad \text{(A.1)}$$

This equation can be simplified as

$$\begin{aligned} J[\epsilon(t)] = &\ \langle\psi(T)|\hat{O}|\psi(T)\rangle \ -\alpha_o \int_0^T [\epsilon(t)]^2 dt - 2Re\left[\int_0^T \langle\chi(t)\left|\frac{\partial}{\partial t} + i\hat{H}\right|\psi(t)\rangle dt\right] \\ = &\ \langle\psi(T)|\hat{O}|\psi(T)\rangle \ -\alpha_o \int_0^T [\epsilon(t)]^2 dt - \int_0^T \langle\chi(t)\left|\frac{\partial}{\partial t} + i\hat{H}\right|\psi(t)\rangle dt \\ &- \int_0^T \langle\chi(t)\left|\frac{\partial}{\partial t} + i\hat{H}\right|\psi(t)\rangle^* dt \\ = &\ \langle\psi(T)|\hat{O}|\psi(T)\rangle \ -\alpha_o \int_0^T [\epsilon(t)]^2 dt - \int_0^T \left[\langle\chi(t)\left|\frac{\partial}{\partial t}\right|\psi(t)\rangle + i\langle\chi(t)\left|\hat{H}\right|\psi(t)\rangle\right] dt \\ &- \int_0^T \left[\langle\chi(t)\left|\frac{\partial}{\partial t}\right|\psi(t)\rangle^* - i\langle\chi(t)\left|\hat{H}\right|\psi(t)\rangle^*\right] dt \end{aligned} \quad \text{(A.2)}$$

The cost functional explicitly depends on $\psi(t)$, $\epsilon(t)$ and $\chi(t)$. Therefore, the variation of the cost functional is given as,

$$\delta J = \frac{\partial J}{\partial \psi(t)}\delta\psi(t) + \frac{\partial J}{\partial \chi(t)}\delta\chi(t) + \frac{\partial J}{\partial \epsilon(t)}\delta\epsilon(t) \quad \text{(A.3)}$$

At an optimal condition, i.e., $\delta J = 0$ therfore we have the following equations,

$$\frac{\partial J}{\partial \psi(t)}\delta\psi(t) = 0, \tag{A.4}$$

$$\frac{\partial J}{\partial \chi(t)}\delta\chi(t) = 0, \tag{A.5}$$

$$\frac{\partial J}{\partial \epsilon(t)}\delta\epsilon(t) = 0. \tag{A.6}$$

The variation of the cost functional with respect to the wave function, $\psi(t)$ is given as,

$$\begin{aligned}\frac{\partial J}{\partial \psi(t)}\delta\psi(t) &= \langle\delta\psi(T)|\hat{O}|\psi(T)\rangle + \langle\psi(T)|\hat{O}|\delta\psi(T)\rangle \\ &- \int_0^T \left[\langle\chi(t)\left|\frac{\partial}{\partial t}\right|\delta\psi(t)\rangle + i\langle\chi(t)\left|\hat{H}\right|\delta\psi(t)\rangle\right]dt \\ &- \int_0^T \left[\langle\chi(t)\left|\frac{\partial}{\partial t}\right|\delta\psi(t)\rangle^* - i\langle\chi(t)\left|\hat{H}\right|\delta\psi(t)\rangle^*\right]dt \end{aligned} \tag{A.7}$$

$$\begin{aligned}\frac{\partial}{\partial t}\langle\chi(t)|\delta\psi(t)\rangle &= \langle\chi(t)|\frac{\partial}{\partial(t)}|\delta\psi(t)\rangle + \langle\frac{\partial}{\partial(t)}\chi(t)|\delta\psi(t)\rangle \\ \equiv \langle\chi(t)|\frac{\partial}{\partial(t)}|\delta\psi(t)\rangle &= \frac{\partial}{\partial t}\langle\chi(t)|\delta\psi(t)\rangle - \langle\frac{\partial}{\partial(t)}\chi(t)|\delta\psi(t)\rangle \end{aligned} \tag{A.8}$$

From equation (A.7) and (A.8), we get

$$\begin{aligned}\frac{\partial J}{\partial \psi(t)}\delta\psi(t) &= \langle\delta\psi(T)|\hat{O}|\psi(T)\rangle + \langle\psi(T)|\hat{O}|\delta\psi(T)\rangle \\ &- \int_0^T dt\left[\frac{\partial}{\partial t}\langle\chi(t)|\delta\psi(t)\rangle - \langle\frac{\partial}{\partial(t)}\chi(t)|\delta\psi(t)\rangle + i\langle\chi(t)\left|\hat{H}\right|\delta\psi(t)\rangle\right]dt \\ &- \int_0^T dt\left[\frac{\partial}{\partial t}\langle\chi(t)|\delta\psi(t)\rangle^* - \langle\frac{\partial}{\partial(t)}\chi(t)|\delta\psi(t)\rangle^* - i\langle\chi(t)\left|\hat{H}\right|\delta\psi(t)\rangle^*\right]dt \\ &= \langle\delta\psi(T)|\hat{O}|\psi(T)\rangle + \langle\psi(T)|\hat{O}|\delta\psi(T)\rangle \\ &- \langle\chi(T)|\delta\psi(T)\rangle + \langle\chi(0)|\delta\psi(0)\rangle + \int_0^T dt\langle\frac{\partial}{\partial(t)}\chi(t)|\delta\psi(t)\rangle \\ &- i\int_0^T dt\langle\chi(t)|\hat{H}|\delta\psi(t)\rangle - \langle\chi(T)|\delta\psi(T)\rangle^* + \langle\chi(0)|\delta\psi(0)\rangle^* \\ &+ \int_0^T dt\langle\frac{\partial}{\partial(t)}\chi(t)|\delta\psi(t)\rangle^* + \int_0^T dt\langle\chi(t)|\hat{H}|\delta\psi(t)\rangle^* \end{aligned}$$

$\delta\psi(0) = 0$ as $\psi(0)$ is an initial wave function.

$$\begin{aligned}
\frac{\partial J}{\partial\psi(t)}\delta\psi(t) &= \langle\delta\psi(T)|\hat{O}|\psi(T)\rangle + \langle\psi(T)|\hat{O}|\delta\psi(T)\rangle \\
&- \langle\chi(T)|\delta\psi(T)\rangle + \int_0^T dt\langle\frac{\partial}{\partial(t)}\chi(t)|\delta\psi(t)\rangle \\
&- i\int_0^T dt\langle\chi(t)|\hat{H}|\delta\psi(t)\rangle - \langle\chi(T)|\delta\psi(T)\rangle^* \\
&+ \int_0^T dt\langle\frac{\partial}{\partial(t)}\chi(t)|\delta\psi(t)\rangle^* + \int_0^T dt\langle\chi(t)|\hat{H}|\delta\psi(t)\rangle^* \\
&= \langle\delta\psi(T)|[\hat{O}|\psi(T)\rangle - |\chi(t)\rangle] - [\langle\psi(T)|\hat{O} - \langle\chi(T)]\delta\psi(T)\rangle \\
&+ \int_0^T dt\langle(\frac{\partial}{\partial t} + i\hat{H})\chi(t)|\delta\psi(t)\rangle + \int_0^T dt\langle(\frac{\partial}{\partial t} + i\hat{H})\chi(t)|\delta\psi(t)\rangle^*
\end{aligned} \tag{A.9}$$

From equations (A.4) and (A.9) we get,

$$i\frac{\partial\chi(t)}{\partial t} = \hat{H}\chi(t) \tag{A.10}$$

with a boundary condition, $|\chi(T)\rangle = \hat{O}|\psi(T)\rangle$

The variation of the cost functional with respect to the lagrange multiplier, $\chi(t)$,

$$\begin{aligned}
\frac{\partial J}{\partial\chi(t)}\delta\chi(t) &= -\int_0^T \left[\langle\delta\chi(t)\left|\frac{\partial}{\partial t} + i\hat{H}\right|\psi(t)\rangle\right] dt, \\
&- \int_0^T \left[\langle\delta\chi(t)\left|\frac{\partial}{\partial t} - i\hat{H}\right|\psi(t)\rangle^*\right] dt.
\end{aligned} \tag{A.11}$$

From equation (A.5) and (A.11) we get,

$$i\frac{\partial\psi(t)}{\partial t} = \hat{H}\psi(t), \tag{A.12}$$

with a initial boundary condition, $\psi(t = 0) = \phi_i$.

The variation of the cost functional with respect to the electric field, $\epsilon(t)$,

$$\begin{aligned}\frac{\partial J}{\partial \epsilon(t)}\delta\epsilon(t) &= -2\alpha_o \int_0^T \epsilon(t)\delta\epsilon(t)dt - i\int_0^T dt\langle\chi(t)|\frac{\partial \hat{H}}{\partial\epsilon(t)}.\delta\epsilon(t)|\psi(t)\rangle, \\ &+ i\int_0^T dt\langle\chi(t)|\frac{\partial \hat{H}}{\partial\epsilon(t)}.\delta\epsilon(t)|\psi(t)\rangle^*, \\ &= \int_0^T dt[-2\alpha_0\epsilon(t) - i\langle\chi(t)|\frac{\partial \hat{H}}{\partial\epsilon(t)}|\psi(t)\rangle + \langle\chi(t)|\frac{\partial \hat{H}}{\partial\epsilon(t)}|\psi(t)\rangle^*]\delta\epsilon(t).\end{aligned}$$

At an optimal condition,

$$\frac{\partial J}{\partial \epsilon(t)}\delta\epsilon(t) = 0.$$

Therefore,

$$\begin{aligned}&\Rightarrow -2\alpha_0\epsilon(t) - i\langle\chi(t)|\frac{\partial \hat{H}}{\partial\epsilon(t)}.\delta\epsilon(t)|\psi(t)\rangle + \langle\chi(t)|\frac{\partial \hat{H}}{\partial\epsilon(t)}|\psi(t)\rangle^* = 0 \\ &\Rightarrow -2\alpha_0\epsilon(t) - 2Im\langle\chi(t)|\frac{\partial \hat{H}}{\partial\epsilon(t)}|\psi(t)\rangle = 0 \\ &\Rightarrow \epsilon(t) = \frac{1}{\alpha_0}Im\langle\chi(t)|\frac{\partial \hat{H}}{\partial\epsilon(t)}|\psi(t)\rangle \qquad \text{(A.13)}\end{aligned}$$

The total Hamiltonian of a system, $\hat{H}$ is given as,

$$\begin{aligned}\hat{H} &= \hat{H}_0 - \mu.\epsilon(t), \\ \Rightarrow \frac{\partial \hat{H}}{\partial\epsilon(t)} &= -\mu, \qquad \text{(A.14)}\end{aligned}$$

where $\hat{H}_0$ is the field-free Hamiltonian of the molecule and μ is the dipole moment function. From equation (A.13) and (A.14) we get,

$$\epsilon(t) = -\frac{1}{\alpha_0}Im\langle\chi(t)|\mu|\psi(t)\rangle. \qquad \text{(A.15)}$$

Therefore, the pulse design equations can be summarized as,

$$\begin{aligned}i\frac{\partial\psi(t)}{\partial t} &= \hat{H}\psi(t), \psi(0) = \phi_i, \qquad \text{(A.16)} \\ i\frac{\partial\chi(t)}{\partial t} &= \hat{H}\chi(t), \chi(T) = \hat{O}\psi(t), \qquad \text{(A.17)} \\ \epsilon(t) &= -\frac{1}{\alpha_0}Im\langle\chi(t)|\mu|\psi(t)\rangle. \qquad \text{(A.18)}\end{aligned}$$

Appendix B

Derivation of the leading error term in the split-operator method

Expanding the time propagator we get the expression reads as (for simplicity we drop the overhead hat symbol on operators),

$$\begin{aligned} e^{\frac{-i\hat{H}}{\hbar}dt} &= e^{\frac{-i(T+V)dt}{\hbar}} = 1 - i(T+V)\frac{dt}{\hbar} \\ &\quad + \frac{(-i)^2(T+V)^2dt^2}{2\hbar^2} + \frac{(-i)^3(T+V)^3dt^3}{3!\hbar^3} + \cdots \\ &= 1 - i(T+V)\frac{dt}{\hbar} - \frac{(T^2+V^2+TV+VT)dt^2}{2\hbar^2} \\ &\quad + i\frac{(T^3+TVT+T^2V+TV^2+VT^2+V^2T+VTV+V^3)dt^3}{3!\hbar^3} \\ &\quad + \cdots \end{aligned} \tag{B.1}$$

Now expanding the right hand side of the above equation we get the following expression,

$$\begin{aligned} e^{-iVdt/2\hbar}e^{-iTdt/\hbar}e^{-iVdt/2\hbar} &= \left[1 - iV\frac{dt}{2\hbar} + \frac{(-iVdt)^2}{8\hbar^2} + \cdots\right]\left[1 - iT\frac{dt}{\hbar} + \frac{(-iTdt)^2}{2\hbar^2} + \cdots\right] \\ &\quad \times \left[1 - iV\frac{dt}{2\hbar} + \frac{(-iVdt)^2}{8\hbar^2} + \cdots\right] \\ &= 1 - i(T+V)\frac{dt}{\hbar} - \frac{(T^2+V^2+TV+VT)dt^2}{2\hbar^2} \\ &\quad + i\left(\frac{V^3}{6} + \frac{T^3}{6} + \frac{VTV}{4} + \frac{V^2T}{8} + \frac{VT^2}{4} + \frac{T^2V}{4} + \frac{TV^2}{8}\right)\frac{dt^3}{\hbar^3} \\ &\quad + \cdots \end{aligned} \tag{B.2}$$

Comparing the exact expression, Eq. (B.1), with the approximation, Eq. (B.2) the leading error term is given as,

$$\text{Error} = i\frac{dt^3}{\hbar^3}\left(\frac{T\,[V,T]}{12} + \frac{[T,V]\,T}{12} + \frac{[T,V]\,V}{24} + \frac{V\,[V,T]}{24}\right) \tag{B.3}$$

$$= i\frac{dt^3}{\hbar^3}\left(\frac{[T,[V,T]}{12} + \frac{[V,[V,T]}{24}\right). \tag{B.4}$$

Bibliography

[1] D. J. Tannor, *Introduction to Quantum Mechanics : A Time-Dependent Perspective*,University Science Books, USA (2007).

[2] R. J. Gordon and S. A. Rice, Annu. Rev. Phys. Chem. **48**, 601 (1997).

[3] V. S. Letokhov, Phys. Today **30**, 23 (1977).

[4] N. Bloembergen and A. H. Zewail, Phys. Today **31**, 23 (1978).

[5] A. H. Zewail, Phys. Today **33**, 27 (1980).

[6] F. F. Crim, Ann. Rev. Phys. Chem. **35**, 657 (1984).

[7] F. F. Crim, Ann. Rev. Phys. Chem. **44**, 397 (1993).

[8] S. Rice and M. Zhao, *Optical Control of Molecular Dynamics*, John Wiley and Sons, New York, (2000).

[9] M. Shapiro and P. Brumer, *Principles of the Quantum Control of Molecular Processes*, John Wiley and Sons, New York, (2002).

[10] N. Bloembergen and A. H. Zewail, J. Phys. Chem. **88**, 5459 (1984).

[11] T. Elsaesser and W. Kaiser, Annu. Rev. Phys. Chem. **42**, 83 (1991).

[12] A. H. Zewail, J. Phys. Chem. **100**, 12701 (1996).

[13] M. Gruebele and R. Bigwood, Int. Rev. Phys. Chem. **17**, 91 (1998).

[14] T. M. Ticich, M. D. Likar, H. R. Dübal, L. J. Butler, and F. F. Crim, J. Chem. Phys. **87**, 5820 (1987).

[15] F. F. Crim, Science **249**, 1387 (1990).

[16] I. Bar, Y. Cohen, D. David, S. Rosenwaks, and J. J. Valentini, J. Chem. Phys. **93**, 2146 (1990).

[17] T. Arusi-Parpar, R. P. Schmid, R. J. Li, I. Bar, and S. Rosenwaks, Chem. Phys. Lett. **268**, 163 (1997).

[18] A. M. Weiner, D. E. Leaird, J. S. Patel, and J. R. Wullert, Opt. Lett. **15**, 326 (1990).

[19] M. M. Wefers and K. A. Nelson, Opt. Lett. **18**, 2032 (1993).

[20] A. M. Weiner, Rev. Sci. Instrum. **71**, 1929 (2000).

[21] R. A. Kaindl, M. Wurm, K. Reimann, P. Hamm, A. M. Weiner, and M. Woerner, J. Opt. Soc. Am. B **17**, 2086 (2000).

[22] T. Brixner and G. Gerber, Opt. Lett. **26**, 557 (2001).

[23] D. Goswami, Phys. Rep. **374**, 385 (2003).

[24] C. Rulliére (Ed.), *Femtosecond Laser Pulses: Principles and Experiments (Second Edition)*, Springer, New York, (2005).

[25] A. H. Zewail (Ed.), *Photochemistry and Photobiology*, Harwood Academic, London, (1983)

[26] E. R. Menzel, *Laser Spectroscopy: Techniques and Applications*, Marcel Dekker, Inc., New York, (1995).

[27] P. Hannaford (Ed.), *Femtosecond Laser Spectroscopy*, Springer, New York, (2005).

[28] V. S. Letokhov, *Laser Control of Atoms and molecules*, Oxford University press, (2007).

[29] E. Schreiber, *Femtosecond real-time spectroscopy of small molecules and cluster*, Springer, New York, (1998).

[30] J. Manz and L. Wöste (Eds.), *Femtosecond Chemistry*, VCH Publishers, Inc., New York, (1995).

[31] P. Gaspard and I. Burghardt (Eds.), *Chemical reactions and their control on the femtosecond time scale*, Adv. Chem. Phys. 101, Wiley, New York, (1997).

[32] V. Sundström (Ed.), *Femtochemistry and Femtobiology*, World Scientific, Singapore, (1997).

[33] A. H. Zewail, J. Phys. Chem. A **104**, 5660 (2000).

[34] S. Mukamel, *Principles of Nonliner Optics and Spectroscopy*, Oxford University Press, (1995).

[35] *Coherent control of photochemical and photobiological systems* (2006), J. Photochem. Photobiol. A, Volume 180, issue 3, pages 225-334.

[36] *Coherent control with femtosecond laser pulses* (2001), Eur. Phys. J. D, Volume 14, issue 2.

[37] A. Bandrauk, Molecules in Laser Fields, Nato ASI series C Mathematical and Physical Sciences, Kluwer Academic Publishers, (1995).

[38] N. P. Moore, G. M. Menkir, A. N. Markewitch, and P. G. R. J. Levis, *Laser control and manipulation of molecules*, edited by R. J. Gordon (American Chemical Society: Washington, DC, 2001), ACS Symposium Series in Chemistry.

[39] *Focus on quantum control* (2009), New J. Phys., Volume 11, pages 105031-105053.

[40] R. Chakrabarti and H. Rabitz, Int. Rev. Phys. Chem. **26**, 671 (2007).

[41] D. J. Tannor and S. A. Rice, J. Chem. Phys. **83**, 5013 (1985).

[42] D. J. Tannor, R. Kosloff and S. A. Rice, J. Chem. Phys. **85**, 5805 (1986).

[43] T. Baumert, M. Grosser, R. Thalweiser, and G. Gerber, Phys. Rev. Lett. **67**, 3753 (1991).

[44] T. Baumert, B. Bühler, M. Grosser, R. Thalweiser, V. Weiss, E. Wiedenmann, and G. Gerber, J. Phys. Chem. **95**, 8103 (1991).

[45] E. D. Potter, J. L. Herek, S. Pedersen, Q. Liu, and A. H. Zewail, Nature **355**, 66 (1992).

[46] T. Baumert and G. Gerber, Isr. J. Chem. **34**, 103 (1994).

[47] J. L. Herek, A. Materny, and A. H. Zewail, Chem. Phys. Lett. **228**, 15 (1994).

[48] T. Baumert, J. Helbing, and G. Gerber, Adv. Chem. Phys. **101**, 47 (1997).

[49] F. Gai, J. C. McDonald, and P. A. Anfinrud, J. Am. Chem. Soc. **119**, 6201 (1997).

[50] S. L. Logunov, V. V. Volkov, M. Braun, and A. M. El-Sayed, Proc. Natl. Acad. Sci. USA **98**, 8475 (2001).

[51] D. S. Larsen, M. Vengris, I. H. Van Stokkum, M. A. van der Horst, F. L. de Weerd, K. J. Hellingwerf, and R. van Grondelle, Biophys. J. **86** 2538 (2004).

[52] M. Vengris, D. S. Larsen, M. A. van der Horst, O. F. A. Larsen, K. J. Hellingwef, and R. van Grondelle, J. Phys. Chem. B **109**, 4197 (2005).

[53] D. S. Larsen and R. van Grondelle, Chem. Phys. Chem. **6**, 828 (2005).

[54] P. Brumer and M. Shapiro, Chem. Phys. Lett. **126**, 541 (1986).

[55] M. Shapiro, J. W. Hepburn and P. Brumer, Chem. Phys. Lett. **149**, 451 (1988).

[56] M. Shapiro and P. Brumer, Acc. Chem. Res. **22**, 407 (1989).

[57] P. Brumer and M. Shapiro, Annu. Rev. Phys. Chem. **43**, 257 (1992).

[58] C. K. Chan, P. Brumer, and M. Shapiro, J. Chem. Phys. **94**, 2688 (1991).

[59] Z. Chen, P. Brumer, and M. Shapiro, J. Chem. Phys. **98**, 6843 (1993).

[60] S. Lee, J. Chem. Phys. **107**, 2734 (1997).

[61] C. Cheng, Y. Y. Yin, and D. S. Elliott, Phys. Rev. Lett. **64**, 507 (1990).

[62] S. M. Park, S. P. Lu, and R. J. Gordon, J. Chem. Phys. **94**, 8622 (1991).

[63] S. P. Lu, S. M. Park, Y. Xie, and R. J. Gordon, J. Chem. Phys. 96, 6613 (1992).

[64] X. Wang, R. Bersohn, K. Takahashi, M. Kawasakai, and H. L. Kim, J. Chem. Phys. **105**, 2992 (1996).

[65] Y. Y. Yin, D. S. Elliott, R. Shehadeh, and R. E. Grant, Chem. Phys. Lett. **241**, 591 (1995).

[66] B. Sheehy, B. Walker, and L. F. DiMauro, Phys. Rev. Lett. **74**, 4799 (1995).

[67] V. D. Kleiman, L. Zhu, J. Allen, and R. J. Gordon, J. Chem. Phys. **103**, 10800 (1995).

[68] L. Zhu, V. D. Kleiman, X. Li, S. P. Lu, K. Trentelman, and R. J. Gordon, Science **270**, 77 (1995).

[69] C. Chen and D. S. Elliott, Phys. Rev. A **53**, 272 (1996).

[70] U. Gaubatz, P. Rudecki, M. Becker, S. Schiemann, M. Klz, and K. Bergmann, Chem. Phys. Lett. **149**, 463 (1988).

[71] U. Gaubatz, P. Rudecki, S. Schiemann, and K. Bergmann, J. Chem. Phys. **92**, 92, 5363 (1990).

[72] G. W. Coulston and K. Bergmann, J. Chem. Phys. **96**, 3467 (1992).

[73] K. Bergmann, H. Theuer, and B. W. Shore, Rev. Mod. Phys. **70**, 1003 (1998).

[74] T. Halfmann and K. Bergmann, J. Chem. Phys. **104**, 7068 (1996).

[75] T. Halfmann, L. P. Yatsenko, M. Shapiro, B. W. Shore, and K. Bergmann, Phys. Rev. A **58**, R46 (1998).

[76] N. V. Vitanov, T. Halfmann, B. W. Shore, and K. Bergmann, Ann. Rev. Phys. Chem. **52**, 763 (2001).

[77] D. J. Tannor and S. A. Rice, Adv. Chem. Phys. **70**, 441 (1988).

[78] A. P. Peirce, M. A. Dahleh, and H. Rabitz, Phys. Rev. A **37**, 4950 (1988).

[79] S. Shi, A. Woody, and H. Rabitz, J. Chem. Phys. **88**, 6870 (1988).

[80] S. Shi and H. Rabitz, Chem. Phys. **139**, 185 (1989).

[81] S. Shi and H. Rabitz, J. Chem. Phys. **92**, 364 (1990).

[82] R. Kosloff, S. A. Rice, P. Gaspard, S. Tersigni, and D. J. Tannor, Chem. Phys. **139**, 201 (1989).

[83] W. Jakubetz, J. Manz, and H. J. Schreier, Chem. Phys. Lett. **165**, 100, (1990).

[84] M. V. Korolkov, Y. A. Logvin, and G. K. Paramonov, J. Phys. Chem. **100**, 8070 (1996).

[85] M. V. Korolkov, J. Manz, and G. K. Paramonov, Chem. Phys. **217**, 341 (1997).

[86] W. Zhu, J. Botina, and H. Rabitz, J. Chem. Phys. **108**, 1953 (1998).

[87] K. Sundermann and R. de Vivie-Riedle, J. Chem. Phys. **110**, 1896 (1999).

[88] T. Hornung and R. de Vivie-Riedle, Europhys. Lett. **64**, 703 (2003).

[89] G. G. Balint-Kurti, F. Manby, Q. Ren, M. Artamonov, T. S. Ho, and H. Rabitz, J. Chem. Phys. **122**, 084110 (2005).

[90] Q. Ren, G. G. Balint-Kurti, F. R. Manby, M. Artamonov, T. S. Ho, and H. Rabitz, J. Chem. Phys. **124**, 014111 (2006).

[91] S. Zou, G. G. Balint-Kurti, and F. R. Manby, J. Chem. Phys. **127**, 044107 (2007).

[92] K. Nakagami, Y. Mizumoto, and Y. Ohtsuki, J. Chem. Phys. 129, 194103 (2008).

[93] H. Umeda, M. Takagi, S. Yamada, S. Koseki, and Y. Fujimura, J. Am. Chem. Soc. **124**, 9265 (2002).

[94] F. Grobmann, L. Feng, G. Schmidt,T. Kunert, and R. Schmidt, Europhys. Lett. **60**, 201 (2002).

[95] M. Artamonov, T. S. Ho, and H. Rabitz, Chem. Phys. **305**, 213 (2002).

[96] K. Hokia, S. Kosekib, T. Matsushitab, R. Sahnounc, and Y. Fujimura, J. Photochem. Photobiol. A: Chemistry **178**, 258 (2006).

[97] Y. Kurosaki, M. Artamonov, T. S. Ho, and H. Rabitz, J. Chem. Phys. **131**, 044306 (2009).

[98] I. Barth, J. Manz, Y. Shigeta, and K. Yagi, J. Am. Chem. Soc. **128**, 7043 (2006).

[99] M. Yamaki, S. -I. Nakayama, K. Hoki, H. Kono, and Y. Fujimara, Phys. Chem. Chem. Phys. **11**, 1662 (2009).

[100] Y. Kurosaki, K. Yokoyama, and A. Yokoyama, J. Chem. Phys. **131**, 144305 (2009).

[101] C. M. Tesch and R. de Vivie-Riedle, Phys. Rev. Lett. **89**, 157901 (2002).

[102] C. M. Tesch and R. de Vivie-Riedle, J. Chem. Phys. **121**. 12158 (2004).

[103] D. Babikov, J. Chem. Phys. **121**, 7577 (2004).

[104] S. Suzuki, K. Mishima, and K. Yamashita, Chem. Phys. Lett. **410**, 358 (2005).

[105] M. Tsubouchi and T. Momose, Phys. Rev. A **77**, 052326 (2008).

[106] M. Schröder and A. Brown, J. Chem. Phys. **131**, 034101 (2009).

[107] R. S. Judson and H. Rabitz, Phys. Rev. Lett. **68**, 1500 (1992).

[108] C. J. Bardeen, V. V. Yakovlev, K. R. Wilson, S. D. Carpenter, P. M. Weber, and W. S. Warren, Chem. Phys. Lett. **280**, 151 (1997).

[109] A. Assion, T. Baumert, M. Bergt, T. Brixmer, B. Kiefer, V. Seyfried, M. Strehle, and G. Gerber, Science **282**, 919 (1998).

[110] D. Yelin, D. Meshulach, and Y. Silberberg, Opt. Lett. **22**, 1793 (1997).

[111] D. Meshulach and Y. Silberberg, Nature **396**, 239 (1998).

[112] V. D. Kleimann. S. M. Arrivo, J. S. Melinger, and E. J. Heilweil, Chem. Phys. **233**, 207 (1998).

[113] T. C. Weinacht, J. Ahn, and P. H. Bucksbaum, Nature **397**, 233 (1999).

[114] D. J. Tannor, R. Kosloff, and A. Bartana, Faraday Discuss. **113**, 365 (1999).

[115] T. Brixner, M. Strehle, and G. Gerber, Appl. Phys. B **68**, 281 (1999).

[116] T. Hornung, R. Meier, and M. Motzkus, Chem.Phys. Lett. **326**, 445 (2000).

[117] R. Bartels, S. Backus, E. Zeek, L. Misoguti, G. Vdovin, I. P. Christov, M. M. Murnane and H. C. Kapteyn, Nature **406**, 164 (2000).

[118] R. J. Levis, G. M. Menkir, and H. Rabitz, Science **292**, 709 (2001).

[119] J. Herek, W. Wohllehen, R. Cogdell, D. Zeidler, and M. Motzkus, Nature **417**, 533 (2002).

[120] T. Brixner and G. Gerber, Chem. Phys. Chem. **4**, 418 (2003).

[121] C. Ventalon, J. M. Fraser, M. H. Vos, A. Alexandrou, J. -L. Martin, and M. Joffre, Proc. Natl. Acad. Sci. USA **101**, 13216 (2004).

[122] M. Dantus and V. V. Lozovoy, Chem. Rev. **104**, 1813 (2004).

[123] V. I. Prokhorenko, A. M. Nagy, S. A. Waschuk, L. S. Brown, R. R. Birge, and R. J. D. Miller, Science **313**, 1257 (2006).

[124] V. I. Prokhorenko, A. M. Nagy, L. S. Brown, and R. J. D. Miller, Chem. Phys. **341**, 296 (2007).

[125] P. Nuernberger, G. Vogt, T. Brixner, and G. Gerber, Phys. Chem. Chem. Phys. **9**, 2470 (2007).

[126] J. Savolainen, R. Fanciulli, N. Dijkhuizen, A. L. Moore, J. Hauer, T. Buckup, M. Motzkus, and J. L. Herek, Proc. Natl. Acad. Sci. USA **105**, 7641 (2008).

[127] D. G. Kuroda, C. P. Singh, Z. Peng and V. D. Kleiman, Science **326**, 263 (2009).

[128] T. Cheng and A. Brown, J. Chem. Phys. **124**, 034111 (2006).

[129] M. Holhaus and B. Just, Phys. Rev. A **49**, 1950 (1994).

[130] Z. Lan, W. Domcke, V. Vallet, A. L. Sobolewski, and S. Mahapatra, J. Chem. Phys. **122**, 224315 (2005).

[131] J. D. Jackson, *Classical Electrodynamics*, Wiley, New York, (1962).

[132] H. Goldstein, *Classical Mechanics, 2nd Ed.*, Addison-Wesley, Reading, MA, (1980).

[133] R. Loudon, *The Quantum Theory of Light, 2nd ed.*, Clarendon, Oxford, (1983).

[134] M. Born and R. Oppenheimer, Ann. Phys. **84**, 457 (1927).

[135] H. Köppel, W. Domcke, and L. S. Cederbaum, Adv. Chem. Phys. **57**, 59 (1984).

[136] F. T. Smith, Phys. Rev. **179**, 111 (1969).

[137] M. Baer, Adv. Chem. Phys. **124**, 39 (2002).

[138] C. A. Mead and D. G. Truhlar J. Chem. Phys. **77**, 6090 (1982)

[139] T. Pacher, L. S. Cederbaum, and H. Köppel J. Chem. Phys. **89**, 7367 (1988)

[140] J. von Neumann and E. Wigner, Phys. Z. **30**, 467 (1929).

[141] E. Teller, J. Phys. Chem. **41**, 109 (1937).

[142] H. A. Jahn and E. Teller, Proc. Roy. Soc. **244**, 1 (1937).

[143] D. R. Yarkony J. Phys. Chem. A **105**, 6277 (2001)

[144] W. Domcke, D. R. Yarkony Annu. Rev. Phys. Chem. **63**, 325 (2012)

[145] Z. Lan, *Photo-induced Nonadiabatic Dynamics of Aromatic Molecules via Conical Intersections. Electronic-structure and Time-dependent Quantum Dynamics Calculations*, Thesis, Munich (2007).

[146] H. C. Longuet-Higgins, U. Öpik , M. H. L Pryce, and R. A. Sack Proc. Roy. Soc. A, **244**, 1 (1958).

[147] G. Herzberg and H. C. Longuet-Higgins, Discuss. Faraday Soc. **35**, 77 (1963).

[148] F. Boukaline, Chem. Phys. **441**, 31 (2014).

[149] E. Lawrence, *An Introduction to Mathematical Optimal Control Theory: version 0.2* (online lecture notes; http://math.berkeley.edu/evans/).

[150] A. E. Bryson and Y. C. Ho, *Applied Optimal Control: Optimization, Estimation and Control*, Boca Raton, FL: taylor and Francis, (1975).

[151] R. F. Stengel, *Optimal Control and Estimation*, Mincola, NY: Dover, (1994).

[152] S. A. Rice and M. Zhao, *Optical Control of Molecular Dynamics*, Wiley Interscience, New York, (2000).

[153] M. Shapiro and P. Brumer, *Principles of the Quantum Control of Molecular Processes*, John Wiley and Sons Canada, Ltd., (2003).

[154] S. P. Shah and S. A. Rice, J. Chem. Phys. **113**, 6536 (2000).

[155] J. Somlói, V. A. Kazakov, and D. J. Tannor, Chem. Phys. **172**, 85 (1993).

[156] W. Zhu and H. Rabitz, J. Chem. Phys. **109**, 385 (1998).

[157] W. Zhu, J. Botina, and H. Rabitz, J. Chem. Phys. **108**, 1953 (1998).

[158] W. Zhu and H. Rabitz, Phys. Rev. A **58**, 4741 (1998).

[159] Y. Ohtsuki, G. Turinici, and H. Rabitz, J. Chem. Phys. **120**, 5509 (2004).

[160] W. H. Press, S. A. Teukolsky, W. T. Vetterling, and B. P. Flannery, *Numerical Recipes*, Cambridge U. P., Cambridge, MA, (1992).

[161] J. Combariza, B. Just, J. Manz, and G. Paramonov, J. Phys. Chem. **95**, 10351 (1991).

[162] G. G. Balint-Kurti, S. Zou and A. Brown, Adv. Chem. Phys. **138**, 43 (2008).

[163] W. H. Press, S. A. Teukolsky, W. T. Vetterling, and B. P. Flannery, *Numerical Recipes*, Cambridge University Press, Cambridge, (2000).

[164] E. Polak, *Computational Methods in Optimization, Mathematics in Science and engineering*, Vol. 77, Academic Press, New York, (1971).

[165] E. G. Birgin, J. M. Martinez and M. Raydan SIAM J. Optim. **10**, 1196 (2000).

[166] P. Gross, D. Neuhauser, and H. Rabitz, J. Chem. Phys. **96**, 2834 (1992).

[167] L. R. Rabiner and C. M. Rader (Eds), *Digital Signal Processing*, IEEE Press, New York, (1972).

[168] S. Sharma, H. Singh, J. N. Harvey, and G. G. Balint-Kurti, J. Chem. Phys. **133**, 174103 (2010).

[169] S. Sharma, H. Singh, and G. G. Balint-Kurti, J. Chem. Phys. **132**, 064108 (2010).

[170] S. Sharma and H. Singh, Chem. Phys. **390**, 68 (2011)

[171] M. D. Feit, J. A. Fleck, Jr., and A. Steiger, J. Comp. Phys. **47**, 412, 1982.

[172] D. Kosloff and R. Kosloff, J. Comput. Phys. **52**, 35 (1983).

[173] C. C. Marston and G. G. Balint-Kurti, J. Chem. Phys. **91**, 3571 (1989).

[174] P. Dutta, S. Adhikari, and S. P. Bhattacharyya, Chem. Phys. Lett. **212**, 677 (1993).

[175] M. D. Feit and J. A. Fleck, Jr., J. Chem. Phys. **78**, 301 (1983).

[176] M. D. Feit and J. A. Fleck, Jr., J. Chem. Phys. **80**, 2578 (1984)

[177] G. C. Schatz and M. A. Ratner, *Quantum Mechanics in Chemistry*, Dover Publications, New York, (2002).

[178] R. T. Skodje, R. Sadeghi, H. Köppel, and J. L. Krause, J. Chem. Phys. **101**, 1725 (1994).

[179] S. Ghosal and S. Mahapatra, J. Phys. Chem. A **109**, 1530 (2005).

[180] B. Marchetti, T. N. Karsili, M. N. Ashfold, and W. Domcke, Phys. Chem. Chem. Phys. **18**, 20007 (2016).

[181] B.-F. He, Y.-Y. Zhao, K.-M. Pei, H.-G. Wang, and X.-M. Zheng, J. Raman Spec. **44**, 834 (2013).

[182] M. Nowak, K. Szczepaniak, A. Barski, and D. Shugar, J. Mol. Struct. **62**, 47 (1980).

[183] D. Shugar and K. Szczepaniak, Inter. J. Quan. Chem. **20**, 573 (1981).

[184] Y. Inoue, N. Furutachi, and K. Nakanishi, J. Org. Chem. **31**, 175 (1966).

[185] R. Sanchez, B. M. Giuliano, S. Melandri, L. B. Favero, and W. Caminati, J. Am. Chem. Soc. **129**, 6287 (2007).

[186] B. M. Giuliano et al., J. Phys. Chem. A **114**, 12725 (2010).

[187] L. Lapinski, M. J. Nowak, A. Leś, and L. Adamowicz, Vib. Spec. **8**, 331 (1995).

[188] A. Les and L. Adamowicz, J. Phys. Chem. **94**, 7021 (1990).

[189] T. L. Galvão, I. M. Rocha, M. D. Ribeiro da Silva, and M. A. Ribeiro da Silva, J. Phys. Chem. A **117**, 12668 (2013).

[190] M. Nowak, J. Fulara, and L. Łapiński, J. Mol. Struct. **175**, 91 (1988).

[191] L. Lapinski, J. Fulara, and M. J. Nowak, Spectrochimica Acta Part A: Molecular Spectroscopy **46**, 61 (1990).

[192] A. Gerega, L. Lapinski, I. Reva, H. Rostkowska, and M. Nowak, Biophys. Chem. **122**, 123 (2006).

[193] A. Gerega, L. Lapinski, M. J. Nowak, A. Furmanchuk, and J. Leszczynski, J. Phys. Chem. A **111**, 4934 (2007).

[194] L. Lapinski, M. J. Nowak, and H. Rostkowska, J. Chem. Phys. **146**, 094306 (2017).

[195] L. Lapinski, M. J. Nowak, A. Les, and L. Adamowicz, J. Am. Chem. Soc. **116**, 1461 (1994).

[196] B. Chmura, M. F. Rode, A. L. Sobolewski, L. Lapinski, and M. J. Nowak, J. Phys. Chem. A **112**, 13655 (2008).

[197] S. J. Glaser et al., Eur. Phys. J. D **69**, 1 (2015).

[198] A. Accardi, A. Borowski, and O. Kühn, J. Phys. Chem. A **113**, 7491 (2009).

[199] H. -J. Werner, P. J. Knowles, R. D. Amos, A. Bernhardsson, and others, MOLPRO-2002, a package of ab inition programs; Universitat Stuttgart: Stuttgart, Germany; University of Birmingham, United Kingdom, (2002).

[200] M. D. Feit and J. A. Fleck, J. Chem. Phys. **78**, 301 (1982).

[201] N. Giri and S. Mahapatra, J. Chem. Phys. **156**, 094305 (2022).

[202] K. Nandipati, A. K. Kanakati, H. Singh, Z. Lan, and S. Mahapatra, Eur. Phys. J. D **71**, 1 (2017).

[203] K. Nandipati, Z. Lan, H. Singh, and S. Mahapatra, J. Chem. Phys. **146**, 214304 (2017).

[204] K. R. Nandipati, A. K. Kanakati, H. Singh, and S. Mahapatra, Phys. Chem. Chem. Phys. **21**, 20018 (2019).

[205] C. Gollub and R. de Vivie-Riedle, Phys. Rev. A **78**, 033424 (2008).

[206] M. Tsubouchi and T. Momose, Phys. Rev. A **77**, 052326 (2008).

[207] W. Domcke and A. L. Sobolewski, Science **302**, 1693 (2003).

[208] T. S. Zwier, Annu. Rev. Phys. Chem. **47**, 205 (1996).

[209] N. Mikami, Bull. Chem. Soc. Jpn. **68**, 683 (1995).

[210] R. J. Stanley and Castleman, J. Chem. Phys. **94**, 7744 (1991).

[211] K. Kleinermanns, C. Janzen, D. Spangenberg, and M. Gerhards, J. Phys. Chem. A **103**, 5232 (1999).

[212] C. Jacoby et al., J. Phys. Chem. A **102**, 4471 (1998).

[213] C. Janzen, D. Spangenberg, W. Roth, and K. Kleinermanns, J. Chem. Phys. **110**, 9898 (1999).

[214] A. Schiefke et al., J. Chem. Phys. **102**, 9197 (1995).

[215] M. Schütz, T. Bürgi, S. Leutwyler, and T. Fischer, J. Chem. Phys. **98**, 3763 (1993).

[216] M. Gerhards and K. Kleinermanns, J. Chem. Phys. **103**, 7392 (1995).

[217] H. Watanabe and S. Iwata, J. Chem. Phys. **105**, 420 (1996).

[218] G. Pino et al., Phys. Chem. Chem. Phys. **2**, 893 (2000).

[219] S. Kaneko, S. Yotoriyama, H. Koda, and S. Tobita, J. Phys. Chem. A **113**, 3021 (2009).

[220] S. I. Ishiuchi, M. Saeki, M. Sakai, and M. Fujii, Chem. Phys. Lett. **322**, 27 (2000).

[221] M. Yi and S. Scheiner, Chem. Phys. Lett. **262**, 567 (1996).

[222] W. Siebrand, M. Z. Zgierski, Z. K. Smedarchina, M. Vener, and J. Kaneti, Chem. Phys. Lett. **266**, 47 (1997).

[223] M. Miyazaki et al., J. Phys. Chem. A **117**, 1522 (2013).

[224] G. Grabner, N. Getoff, J. Zechner, and G. Köhler, Chem. Phys. Lett. **37**, 297 (1976).

[225] G. Grabner, G. Köhler, J. Zechner, and N. Getoff, J. Phys. Chem. **84**, 3000 (1980).

[226] C. M. Tseng, Y. T. Lee, and C. K. Ni, J. Chem. Phys. **121**, 2459 (2004).

[227] A. L. Sobolewski and W. Domcke, J. Phys. Chem. A **105**, 9275 (2001).

[228] A. L. Sobolewski, W. Domcke, C. Dedonder-Lardeux, and C. Jouvet, Phys. Chem. Chem. Phys. **4**, 1093 (2002).

[229] S. G. Ramesh and W. Domcke, Faraday Discuss. **163**, 73 (2013).

[230] M. Abe, Y. Ohtsuki, Y. Fujimura, Z. Lan, and W. Domcke, J. Chem. Phys. **124**, 224316 (2006).

[231] D. Zeidler, S. Frey, K. L. Kompa, and M. Motzkus, Phys. Rev. A **64**, 023420 (2001).

[232] A. Auger et al., Math. Models Meth. Appl. Sci. **12**, 1281 (2002).

[233] O. Atabek, C. M. Dion, and A. B. H. Yedder, J. Phys. B **36**, 4667 (2003).

[234] M. Tsubouchi, A. Khramov, and T. Momose, Phys. Rev. A **77**, 023405 (2008).

[235] S. Schumm, M. Gerhards, W. Roth, H. Gier, and K. Kleinermanns, Chem. Phys. Lett. **263**, 126 (1996).

[236] H. Bist, J. C. Brand, and D. Williams, J. Mol. Spectros. **24**, 402 (1967).

[237] S. Mahapatra and N. Sathyamurthy, J. Chem. Soc. Faraday Trans. **93**, 773 (1997).

[238] H. Köppel, W. Domcke, and L. S. Cederbaum, Adv. Chem. Phys. **57**, 59 (1984).

[239] R. Baer, D. M. Charutz, R. Kosloff, and M. Baer, J. Chem. Phys. **105**, 9141 (1996).

[240] J. Steadman and J. A. Syage, J. Chem. Phys. **92**, 4630 (1990).

[241] G. Berden, W. L. Meerts, M. Schmitt, and K. Kleinermanns, J. Chem. Phys. **104**, 972 (1996).

[242] S. Martrenchard-Barra et al., Chem. Phys. Lett. **310**, 173 (1999).

[243] G. Pino et al., J. Chem. Phys. **111**, 10747 (1999).

[244] O. David, C. Dedonder-Lardeux, and C. Jouvet, Int. Rev. Phys. Chem. **21**, 499 (2002).

[245] G. Grégoire et al., J. Phys. Chem. A **104**, 9087 (2000).

[246] T. Sawamura, A. Fujii, S. Sato, T. Ebata, and N. Mikami, J. Phys. Chem. **100**, 8131 (1996).

[247] J. Syage and J. Steadman, J. Chem. Phys. **95**, 2497 (1991).

[248] C. Jouvet, C. Lardeux-Dedonder, M. Richard-Viard, D. Solgadi, and A. Tramer, J. Phys. Chem. **94**, 5041 (1990).

[249] S. Mahapatra and N. Sathyamurthy, J. Chem. Phys. **102**, 6057 (1995).

[250] S. Mahapatra and H. Köppel, J. Chem. Phys. **109**, 1721 (1998).

List of publications

1. **N. Giri** and S. Mahapatra, *"Optimal control of photodissociation of phenol using genetic algorithm"*, J. Chem. Phys. **156**, 094305 (2022).

2. **N. Giri** and S. Mahapatra, *"Design of IR laser pulse for photodissociation of phenol using genetic algorithm"*, (manuscript is communicated).

3. **N. Giri** and S. Mahapatra, *"Control of the $\pi\pi^*$ state-mediated tautomerization in the 4(3H)-pyrimidinone/4-hydroxypyrimidine system"*, (manuscript under preparation).

4. **N. Giri** and S. Mahapatra, *"Control of vibrational transitions in 4(3H)-pyrimidinone/4-hydroxypyrimidine system"*, (manuscript under preparation).

Posters and oral presentations in conferences/symposia

1. Poster presentation in "CHEMFEST 2020, 18^{th} annual in-house symposium, 27-28 February, 2020 at School of Chemisty, University of Hyderabad, India".

2. Poster presentation in "CHEMFEST 2022, 20^{th} annual in-house symposium, 22-23 April, 2022 at School of Chemisty, University of Hyderabad, India".

3. Oral presentation in "CHEMFEST 2022, 20^{th} annual in-house symposium, 22-23 April, 2022 at School of Chemisty, University of Hyderabad, India".

Control of Chemical Dynamics of Polyatomic Molecules by IR and UV Laser Pulses

by Nitai Giri

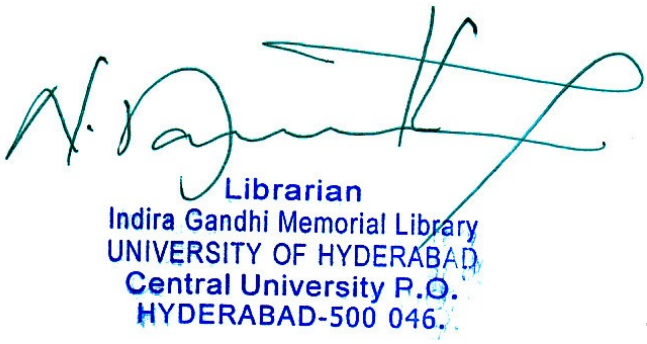

Submission date: 23-Aug-2023 11:52AM (UTC+0530)
Submission ID: 2149828398
File name: Nitai_Giri.pdf (5.23M)
Word count: 38103
Character count: 179009

Control of Chemical Dynamics of Polyatomic Molecules by IR and UV Laser Pulses

ORIGINALITY REPORT

18%	10%	16%	1%
SIMILARITY INDEX	INTERNET SOURCES	PUBLICATIONS	STUDENT PAPERS

PRIMARY SOURCES

1	Nitai Giri, Susanta Mahapatra. "Optimal control of photodissociation of phenol using genetic algorithm", The Journal of Chemical Physics, 2022 Publication	7%
2	chemistry.uohyd.ac.in Internet Source	3%
3	Nitai Giri, S. Mahapatra. "Optimal control of photodissociation of phenol using genetic algorithm", The Journal of Chemical Physics, 2022 Publication	2%
4	repository.ias.ac.in Internet Source	1%
5	mediatum.ub.tum.de Internet Source	<1%
6	opus.bibliothek.uni-wuerzburg.de Internet Source	<1%
7	www.researchgate.net	

Susanta Mahapatra
Professor
School of Chemistry
University of Hyderabad
Hyderabad-500 046, India.

	Internet Source	<1%
8	aip.scitation.org Internet Source	<1%
9	nozdr.ru Internet Source	<1%
10	Zhenggang Lan. "Time-dependent quantum wave-packet description of the [sup 1]πσ[sup", The Journal of Chemical Physics, 2005 Publication	<1%
11	Submitted to University of Hyderabad, Hyderabad Student Paper	<1%
12	publishup.uni-potsdam.de Internet Source	<1%
13	"Femtosecond Chemistry", Wiley, 1994 Publication	<1%
14	www2.pt.tu-clausthal.de Internet Source	<1%
15	hal.archives-ouvertes.fr Internet Source	<1%
16	PRAVEEN KUMAR, SITANSH SHARMA, HARJINDER SINGH. "OPTIMALLY CONTROLLED VIBRATIONAL POPULATION TRANSFER IN A	<1%

DIATOMIC QUANTUM SYSTEM", Journal of Theoretical and Computational Chemistry, 2011
Publication

17	Sitansh Sharma, Harjinder Singh, Gabriel G. Balint-Kurti. "Genetic algorithm optimization of laser pulses for molecular quantum state excitation", The Journal of Chemical Physics, 2010 Publication	<1 %
18	arxiv.org Internet Source	<1 %
19	refubium.fu-berlin.de Internet Source	<1 %
20	scholarworks.umass.edu Internet Source	<1 %
21	Johannes Ehrmaier, David Picconi, Tolga N. V. Karsili, Wolfgang Domcke. "Photodissociation dynamics of the pyridinyl radical: Time-dependent quantum wave-packet calculations", The Journal of Chemical Physics, 2017 Publication	<1 %
22	The Jerusalem Symposia Quantum Chemistry and Biochemistry, 1991. Publication	<1 %

vdoc.pub

23	Internet Source	<1%
24	"Ultrafast Dynamics Driven by Intense Light Pulses", Springer Science and Business Media LLC, 2016 Publication	<1%
25	Mitra Ataelahi, Reza Omidyan. "Microhydration Effects on the Electronic Properties of Protonated Phenol: A Theoretical Study", The Journal of Physical Chemistry A, 2013 Publication	<1%
26	Chergui, Majed. "FEMTOCHEMISTRY : Ultrafast Chemical and Physical Processes in Molecular Systems", Femtochemistry, 1996. Publication	<1%
27	Springer Series in Chemical Physics, 2007. Publication	<1%
28	Thomas Herrmann, Qinghua Ren, Gabriel G. Balint-Kurti, Frederick R. Manby. " design of picosecond infrared laser pulses for controlling vibrational-rotational excitation of CO molecules ", The Journal of Chemical Physics, 2007 Publication	<1%
29	Varnavski, Oleg, Theodore Goodson III, and Peter Bäuerle. "", Linear and Nonlinear Optics	<1%

of Organic Materials VII, 2007.
Publication

30	istina.ipmnet.ru Internet Source	<1%
31	Dohle, M., J. Manz, and G. K. Paramonov. "A Pump & Dump & Probe Strategy for the Spectroscopy of the Transition State During a Laser-Controlled Isomerization: Model Simulation for the Cope Rearrangement of 2,6-Dicyanoethylmethylsemibullvalene", Berichte der Bunsengesellschaft für physikalische Chemie, 1995. Publication	<1%
32	Submitted to University of Hong Kong Student Paper	<1%
33	L. S. Cederbaum. "The multistate vibronic coupling problem", The Journal of Chemical Physics, 1983 Publication	<1%
34	"Controlling Quantum Dynamics with Assisted Adiabatic Processes", Advances in Chemical Physics, 2016. Publication	<1%
35	Thomas Herrmann. "Ab initio design of picosecond infrared laser pulses for controlling vibrational-rotational excitation of	<1%

CO molecules", The Journal of Chemical Physics, 2007
Publication

36	Wolfgang Domcke. "Theory of Ultrafast Nonadiabatic Excited-State Processes and their Spectroscopic Detection in Real Time", Advances in Chemical Physics, 01/01/1997 Publication	<1 %
37	export.arxiv.org Internet Source	<1 %
38	"Surface and Interface Science", Wiley, 2016 Publication	<1 %
39	oatao.univ-toulouse.fr Internet Source	<1 %
40	Tseng, Chien-Ming, Yuan T. Lee, Chi-Kung Ni, and Jia-Lin Chang. "Photodissociation Dynamics of the Chromophores of the Amino Acid Tyrosine: *p*-Methylphenol, *p*-Ethylphenol, and *p*-(2-Aminoethyl)phenol†", The Journal of Physical Chemistry A, 2007. Publication	<1 %
41	jcp.aip.org.globalproxy.cvt.dk Internet Source	<1 %
42	link.springer.com Internet Source	<1 %
43	www.technion.ac.il	

	Internet Source	<1%
44	"Vibronic Interactions and the Jahn-Teller Effect", Springer Science and Business Media LLC, 2012 Publication	<1%
45	T. S. Venkatesan. "Exploring the Jahn-Teller and pseudo-Jahn-Teller conical intersections in the ethane radical cation", The Journal of Chemical Physics, 2005 Publication	<1%
46	Y. Miller, G. M. Chaban, B. J. Finlayson-Pitts, R. B. Gerber. " Photochemical Processes Induced by Vibrational Overtone Excitations: Dynamics Simulations for -HONO, -HONO, HNO , and HNO −H O ", The Journal of Physical Chemistry A, 2006 Publication	<1%
47	publikationen.bibliothek.kit.edu Internet Source	<1%
48	openresearch-repository.anu.edu.au Internet Source	<1%
49	K. R. Nandipati, Z. Lan, H. Singh, S. Mahapatra. "An alternative laser driven photodissociation mechanism of pyrrole via πσ*1／S0 conical intersection", The Journal of Chemical Physics, 2017	<1%

Publication

50	M. Perić, Sigrid D. Peyerimhoff, Robert J. Buenker. " investigation of the vibronic structure of the C H spectrum ", Molecular Physics, 1990 Publication	<1 %
51	Sitansh Sharma, Harjinder Singh. "Laser pulse shaping for optimal control of multiphoton dissociation in a diatomic molecule using genetic algorithm optimization", Chemical Physics, 2011 Publication	<1 %
52	archiv.ub.uni-heidelberg.de Internet Source	<1 %
53	www.ias.ac.in Internet Source	<1 %
54	Arasaki, Y.. "Quantum wavepacket dynamics for time-resolved photoelectron spectroscopy of the NO"2 conical intersection", Chemical Physics, 20070925 Publication	<1 %
55	Bjørn Felsager. "Geometry, Particles, and Fields", Springer Science and Business Media LLC, 1998 Publication	<1 %
56	Minho Kim, Sang-Su Kim, Hyuk Kang, Young Dong Park. "REMPI and IR-UV double	<1 %

resonance spectroscopy of 3-aminophenol·(NH3)1 cluster in the gas phase", Journal of Molecular Spectroscopy, 2010
Publication

57	Rangana Bhattacharya, Souvik Chatterjee, S. S. Bhattacharyya. " Preparation and probing of coherent vibrational wave packets in the ground electronic state of HD ", Physical Review A, 2012 Publication	<1 %
58	Keller, O.. "On the theory of spatial localization of photons", Physics Reports, 200505 Publication	<1 %
59	archive.org Internet Source	<1 %
60	pubs.rsc.org Internet Source	<1 %
61	scholar.sun.ac.za Internet Source	<1 %
62	Chieko Honma, Mohammad Saleem. "Approximate Inverse Preconditioners for the Conjugate Gradient Method", International Journal of Computer Mathematics, 2002 Publication	<1 %
63	K. R. Nandipati, Arun Kumar Kanakati, H. Singh, S. Mahapatra. " Controlled	<1 %

intramolecular H-transfer in malonaldehyde in the electronic ground state mediated through the conical intersection of nπ* and ππ* excited electronic states ", Physical Chemistry Chemical Physics, 2019
Publication

64	NATO ASI Series, 1992. Publication	<1 %
65	Submitted to Nanyang Technological University, Singapore Student Paper	<1 %
66	Springer Series in Chemical Physics, 1998. Publication	<1 %
67	digital.library.unt.edu Internet Source	<1 %
68	G. M. WEBB, M. BRIO, G. P. ZANK. "Lagrangian and Hamiltonian aspects of wave mixing in non-uniform media: waves on strings and waves in gas dynamics", Journal of Plasma Physics, 1998 Publication	<1 %

Exclude quotes	On	Exclude matches	< 14 words
Exclude bibliography	On		